

INVESTIGATION OF THE EFFECTS OF EQUAL CHANNEL ANGULAR
EXTRUSION ON LIGHT WEIGHT ALLOYS

A THESIS SUBMITTED TO
THE GRADUATE SCHOOL OF NATURAL AND APPLIED SCIENCES
OF
MIDDLE EAST TECHNICAL UNIVERSITY

BY

PINAR KARPUZ

IN PARTIAL FULFILLMENT OF THE REQUIREMENTS
FOR
THE DEGREE OF DOCTOR OF PHILOSOPHY
IN
METALLURGICAL AND MATERIALS ENGINEERING

JANUARY 2012

Approval of the thesis:

**INVESTIGATION OF THE EFFECTS OF EQUAL CHANNEL
ANGULAR EXTRUSION ON LIGHT WEIGHT ALLOYS**

submitted by **PINAR KARPUZ** in partial fulfillment of the requirements for the degree of **Doctor of Philosophy in Metallurgical and Materials Engineering Department, Middle East Technical University** by,

Prof. Dr. Canan Özgen _____
Dean, Graduate School of Natural and Applied Sciences

Prof. Dr. Tayfur Öztürk _____
Head of Department, **Metallurgical and Materials Engineering**

Prof. Dr. C. Hakan Gür _____
Supervisor, **Metallurgical and Materials Engineering Dept., METU**

Prof. Dr. İbrahim Karaman _____
Co-Supervisor, **Mechanical Engineering Dept., Texas A&M University**

Examining Committee Members:

Prof. Dr. Tayfur Öztürk _____
Metallurgical and Materials Engineering Dept., METU

Prof. Dr. C. Hakan Gür _____
Metallurgical and Materials Engineering Dept., METU

Prof. Dr. Uğurhan Akyüz _____
Civil Engineering Dept., METU

Assist. Prof. Dr. Besim Baranoğlu _____
Manufacturing Engineering Dept., Atılım University

Assist. Prof. Dr. Y. Eren Kalay _____
Metallurgical and Materials Engineering Dept., METU

Date: 27.01.2012

I hereby declare that all information in this document has been obtained and presented in accordance with academic rules and ethical conduct. I also declare that, as required by these rules and conduct, I have fully cited and referenced all material and results that are not original to this work.

Name, Last Name: Pınar Karpuz

Signature:

ABSTRACT

INVESTIGATION OF THE EFFECTS OF EQUAL CHANNEL ANGULAR EXTRUSION ON LIGHT WEIGHT ALLOYS

Karpuz, Pınar

PhD., METU - Department of Metallurgical and Materials Engineering

Supervisor: Prof.Dr. C. Hakan Gür

Co-supervisor: Prof.Dr. İbrahim Karaman

January 2012, 192 pages

Severe plastic deformation methods are of great interest in industrial forming applications, as they give rise to significant refinement in microstructures and improvements in mechanical and physical properties. In the “Equal Channel Angular Extrusion (ECAE)”, which is the most common method for production of ultrafine grained bulk samples, very high plastic strains are introduced into the bulk material without any change in cross section. This study is composed of two main parts. Part I focuses on the plastic deformation behavior of Al alloys by modeling ECAE with Msc. Marc finite element software. A series of

numerical experiments were carried out for the die angles of 90°, 120°, and 150°, different friction conditions, and different round corners. Besides, the effects of strain hardening characteristics of the material, strain hardening coefficient (K) and exponent (n) of Hollomon's law, on corner gap formation and strain homogeneity in equal channel angular pressing process were investigated quantitatively. The results were compared and verified with those of the upper bound analysis. The numerical results showed that the process performance can be improved by modifying the die corner curvature accordingly, without running time consuming simulations. On the other hand, the aim of Part 3 is to investigate the texture evolution, mechanical response and the corresponding mechanisms, in terms of the flow stress anisotropy and tension-compression asymmetry in the ZK60 Mg alloy. The alloy was processed using ECAE, with different processing routes and temperatures, in order to produce samples with a wider variety of microstructures and crystallographic textures. Several mechanical tests and microstructure examinations were carried out; and the flow stress anisotropy and tension-compression asymmetry of the as-received and processed samples were measured. It was found that the initial texture has a strong effect on the resulting textures; and the textures, combined with the microstructure effect, define the mechanical properties of processed samples. Thus, the tension-compression asymmetry and the flow stress anisotropy variations in the processed samples are attributed to the generated textures and it is possible to control these properties by controlling the processing route and temperature.

Keywords: Equal channel angular extrusion, Finite element modeling, Al-alloy, Mg-alloy, texture, flow strength anisotropy, Tension-compression asymmetry.

ÖZ

EŞ KANALLI AÇISAL EKSTRÜZYON YÖNTEMİNİN HAFİF ALAŞIMLAR UZERİNDEKİ ETKİLERİNİN İNCELENMESİ

Karpuz, Pınar

Doktora, ODTÜ - Metalurji ve Malzeme Mühendisliği Bölümü

Tez Yöneticisi: Prof.Dr. C. Hakan Gür

Yardımcı Tez Yöneticisi: Prof.Dr. İbrahim Karaman

Ocak 2012, 192 sayfa

Şiddetli plastik deformasyon yöntemleri, tane boyutunu aşırı küçültmeleri ve mekanik özellikleri iyileştirmeleri sebebiyle birçok endüstriyel şekillendirme uygulaması alanında ilgi uyandırmaktadır. Bu yöntemlerin arasında en çok bilinen ve kullanılanı, malzemenin kesit alanını değıştirmeden yüksek plastik gerinim oluşumuna olanak veren “Eş Kanallı Açısal Ekstrüzyon (EKAE)” dur. Bu çalışma iki ana bölümden oluşmaktadır. İlk bölüm, ticari sonlu elemanlar yazılımı Msc Marc ile Alüminyum alaşımlarının plastik deformasyonunun modellenmesi ve incelenmesini içermektedir. Bu bağlamda 90, 120 ve 150 derecelik kalıp açıları, farklı sürtünme katsayıları ve farklı köşe yuvarlaklıklarının etkilerinin incelendiğı birçok nümerik deney yapılmıştır.

Ayrıca, malzemenin gerinim sertleşmesi özelliklerinin ve Hollomon Denklemi'nde yer alan gerinim sertleşmesi katsayısı (K) ve üssü (n) değerlerinin, köşe boşluğu oluşumundaki etkileri kapsamlı olarak çalışılmıştır. Elde edilen bulgular yüksek sınır analizi ve doğrulanmıştır. Nümerik sonuçlar işlem performansının kalıp köşe yuvarlaklığının modifiye edilmesiyle artırılabilirliğini göstermiştir. Öte yandan, ikinci bölüm, bir diğer hafif alaşım olan Magnezyum ZK60'ın doku oluşumu, çekme-basma asimetrisi ve akma gerilmesi anizotropilerinin incelemektedir. Çalışmada alaşımın mikroyapısal ve dokusal gelişimlerinin belirlenmesi hedefiyle EKAE yöntemiyle değişik rota ve sıcaklıklarda deforme edilmiştir. Deforme edilmiş malzemelere çeşitli mekanik testler uygulanmış; akma dayancısı anizotropileri ve çekme-basma asimetrisi ölçülmüştür. Bu mekanik davranışlara sebep olan deformasyon mekanizmaları incelenmiştir. Elde edilen bulgularla değişik işlem şartları ve sıcaklıklarının, doku oluşumu ve mekanik davranışlara etkileri belirlenmeye çalışılmıştır. Çalışma sonucunda malzemenin başlangıçtaki dokusunun işlem sonrasındaki dokuyu büyük ölçüde etkilediği, ve bu durumun mikroyapısal gelişim ve mekanik özellikler üzerinde önemli etkileri olduğu gözlenmiştir. Bu bağlamda, farklı işlem görmüş malzemelerde çekme-basma asimetrisi ve akma dayancısı anizotropisindeki değişikliklerin doku gelişimiyle doğrudan ilgili olduğu anlaşılmış ve bu parametrelerin işlem rotası ve sıcaklığının kontrollü olarak değiştirilmesiyle kontrol edilebileceği belirtilmiştir.

Anahtar Kelimeler: Eş Kanallı Açısız Ekstrüzyon, Sonlu elemanlar analizi, Alüminyum alaşımları, Magnezyum alaşımları, doku, akma dayancısı anizotropisi, çekme-basma asimetrisi.

To My Family

ACKNOWLEDGEMENTS

I wish to express my gratitude to my supervisor Prof. Dr. C. Hakan Gür for his guidance, understanding and support throughout the study. His support; at all stages of this study was vital, and I truly appreciate it; if not admire. The invaluable contributions of the examining committee are also highly acknowledged.

I want to express my deepest gratitude to my co-supervisor, Prof. Dr. Ibrahim Karaman of Texas A&M University, TX, USA. I sincerely know that it was very generous of Dr. Karaman to give me the chance of working in his team. Without his support, this thesis simply would not be realized. Besides, I thankfully appreciate not only his support in this research, but also for being a mentor for me. I am also deeply thankful to Dr. Sena Karaman, kind and elegant wife of Dr. Karaman, for being always there for me, consoling and mentoring. She made me feel that an elder sister would not be different than her.

My special thanks go to Dr. Engin F. Kalkan and his elegant wife. Mrs. Fatma Kalkan. Dr. Kalkan made me feel real safe in College Station, ensuring that no one can disturb or trouble me there. I will always remember and appreciate this feeling of “safe” he brought to my life.

I remember using the following words to thank my parents in my M.S. thesis: “I’m deeply thankful to mom and dad, whose emotional strength, free-flowing love and caring concern have helped shape my maturation. Without their

patience and support, the research period would have been a complete disaster”. Now I know much better what “patience and support” is. My father, Prof. Dr. Celal Karpuz literally made this thesis real, not letting me give up under any circumstances. “Not giving up” is the most important thing I learned from my father and my wonderful mother, V. Ayten Karpuz, with many other characteristics and values that a daughter should have and a family can give. I am afraid there are no words in any language to explain how extraordinary people my parents are, and how I feel about them.

Of course, my parents are not the only ones in my family to thank. A very special person, my aunt Dr. G. Seckin Naipoglu was always there for me, and actually with me in Texas. My bond with her is very strong and deep; deeper than a lot of people cannot even imagine. My cousins, Osman Oytun Naipoglu, Mustafa Naipoglu were also of great support even from thousands of miles away. Also Defne Alya Naipoglu, my sweetest niece brought joy to me and my family’s lives; and I thank her mother, my sister-in law Neslihan Naipoglu and her father, Mustafa Naipoglu, for bringing her to our lives.

When it comes to friends, my best friend, Dr. A. Semih Sunkar has a special place. It is a fact that there were so far away, I am happy and proud to call him my “best friend”. I appreciate all kinds of help and support I got from him, but cannot thank him enough for everything he has done for me. As my friends in METU, I wish to express my gratitude to Dr. Caner Simsir, Metehan Erdogan, Gulden Simsek and Ebru Ozdemir Arslan. Dr. Simsir was the one that “built” the base of this thesis and supported not only it; but also me with his friendship and mentoring in almost every area of my life. Mr. Erdogan, is also more than a friend to me ever since I met him. His mastership in thermodynamics and patience in lecturing me were not only amazing; but also inspiring. He is a true

blessing for everyone around him, and I am extremely lucky to be one of them. Mrs. Simsek and Mrs. Ozdemir Arslan, made the darkest days in the department bearable. I sincerely thank them for everything they have done.

The kind help of Mr. Robert Barber is also highly acknowledged. Besides being an extremely kind gentleman and a real master in what he is doing, he was very understanding and friendly to me. I really enjoyed our chats during the experiments and appreciate his effort for teaching me and helping me.

I want to thank my labmates at Texas A&M University, MESAM Lab. Dr. K. Can Atli holds a special place; teaching me, helping me, and being there for me at many moments of this period. I am also thankful to Mr. Nick Barta, Mr. Nick Bruno, Dr. A. Alper Cerit, Mr. Ebubekir Dogan and her sweet wife Mrs. F. Ceyda Dogan, Mr. Alper Evirgen, Mr. Brian Franco, Mr. Ceylan Hayrettin, Mr. Liangfa Hu, Mr. Murat Kaynak, Mr. Ankush Kothalkar, Mr. Ji Ma, Mr. James A. Monroe, Dr. Nevin Ozdemir, Mr. Li-Wei Tseng, Mr. Cengiz Yegin and Mr. Ruixian Zhu (please note the alphabetical order) for the comfortable and peaceful environment they supported. The close friendship of Mr. Onur Saray (soon-to-be Dr. Saray) is also highly acknowledged.

I want to express my special thanks to Mrs. Sonia Modarres Razavi, the pretty lady who taught me “what was going on in those circles”. She was my best friend, the first person I would call to pass any news, the one I hugged and cried for good or bad. I thank god for knowing her and having her with me.

TABLE OF CONTENTS

ABSTRACT.....	iv
ÖZ.....	vi
ACKNOWLEDGEMENTS.....	ix
TABLE OF CONTENTS.....	xiii
LIST OF FIGURES.....	xiv
LIST OF TABLES.....	xix
CHAPTER	
1. INTRODUCTION.....	1
2. FINITE ELEMENT MODELING OF ECAE OF ALUMINUM ALLOYS ...	8
2.1. Theoretical Background and Literature Review.....	8
2.1.1 Al and Its Alloys.....	8
2.1.2 Equal Channel Angular Extrusion (ECAE) and Its Applications on Al Alloys	9
2.1.3 Finite Element Modeling of ECAE.....	14
2.2. Results	17
2.2.1. Effect of Die Geometry	17
2.2.2. Effect of Friction	23
2.2.3. Corner Gap Analysis in ECAE.....	26
2.3. Conclusion.....	41

3. INVESTIGATION OF TEXTURE EVOLUTION AND MECHANICAL FLOW RESPONSE AND ANISOTROPY IN ZK60 MAGNESIUM ALLOY PROCESSED BY EQUAL CHANNEL ANGULAR PRESSING.....	43
3.1 Theoretical Background and Literature Review.....	43
3.1.1 Mg and its alloys	43
3.1.2 Deformation of Mg and its alloys.....	48
3.1.3 Development and measurement of crystallographic texture	57
3.1.4 Applications of ECAE on Mg alloys.....	68
3.2. Experimental Methods and Materials.....	76
3.2.1 Thermomechanical Processing of ZK60 Mg Alloy by ECAE	76
3.2.2 Analytical methods.....	82
3.3. Experimental Results and Discussions.....	87
3.3.1 The as-received Material: S4.....	87
3.3.2. ECAE Processed Samples: Conventional Routes	94
3.3.3. ECAE Processed Samples: Hybrid Routes	118
3.3.4 ECAE Failures.....	151
3.3.5 Effect of Evolved Texture on Mechanical Response and Deformation Mechanisms.....	158
3.4. Conclusions	166
4. CLOSING COMMENTS AND FUTURE WORK.....	171
REFERENCES.....	173
VITA	192

LIST OF FIGURES

Figure 1.1.1. Schematic illustration of ECAE process.....	10
Figure 2.1.2. The four conventional processing routes in ECAE [76].....	12
Figure 2.2.1. Effect of die geometry parameters on total equivalent plastic strain distributions for frictionless condition: (a) $\Phi=90^\circ$, (b) $\Phi=120^\circ$, and (c) $\Phi=150^\circ$. [68].....	19
Figure 2.2.2. Corner gap for $\Phi=90^\circ$ and $\psi = 0^\circ$ die (frictionless condition). [68]	22
Figure 2.2.3. Effect of different friction conditions on total equivalent plastic strain distributions of a billet deformed in a right angle die with central angle of 0.[68]	24
Figure 2.2.4. Strain distributions and deformation behavior of deformed billets: For the friction coefficients between the billet and the die walls of (a) 0, (b) 0.025, (c) 0.05, (d) 0.075, (e) 0.1, (f) 0.125 and (g) 0.15. [68]	25
Figure 2.2.5. Stress–strain curves for extreme cases of Hollomon’s equation. [71]	27
Figure 2.2.6. The variation of corner gap angle with strain hardening exponent (n) for different strain hardening coefficients (K). [73]	28
Figure 2.2.7. The variation of corner gap angle with strain hardening coefficient (K) for different strain hardening exponents (n). [73].....	29
Figure 2.2.8. The combined effect of the strain hardening coefficient (K) and strain hardening exponent (n) on the corner gap angle (α). [71].....	30
Figure 2.2. 9. Velocity profiles in the billet (a) before the formation of the corner gap, (b) during the formation of the corner gap and (c) after the formation of the corner gap. [71]	31

Figure 2.2.10. The effect of ψ on force–displacement curve of the ram. [71] ...	34
Figure 2.2.11. The distribution of equivalent plastic strain for dies with $\psi = 0^\circ$, 30° , 57° and 90° . [71].....	35
Figure 2.2.12. Comparison of the punch pressure values obtained by FEM and upper bound analysis. [71]	38
Figure 2.2.13. Comparison of the strain values obtained by FEM and upper bound analysis. [71]	40
Figure 3.1.1. Effect of alloying elements for Mg on several mechanical properties [77]	45
Figure 3.1.2.HCP crystal structure.	49
Figure 3.1.3. Active slip systems in Mg and its alloys [78].	50
Figure 3.1.4. The possible model for source mechanism for non-basal $\langle c+a \rangle$ slip dislocation [26].	53
Figure 3.1.5. The most common twin systems in Mg and its alloys [83].	55
Figure 3.1.6. Crystallographic elements of twin [84].	55
Figure 3.1.7. Shape change produced by $(101\bar{2})$ twinning [60].	57
Figure 3.1.8. Schematic rolling textures in HCP metals with different c/a ratios [84].	60
Figure 3.1.9. Two methods for representing the orientation g . (a) Miller indices (b) Euler angle [84].	63
Figure 3.1.10. Schematics that illustrates the basic concepts of a pole figure [60].	64
Figure 3.1.11. (a) Stereographic projection, (b) equal area projection [60].	65
Figure 3.1.12. Back-reflection technique [64].	66
Figure 3.1.13. Effect of (a) tilting angle on effective irradiated specimen area and (b) broadening of the reflection beam [64].	67
Figure 3.2.1. The ECAE system at TAMU (Backpressure die).	78
Figure 3.2.2. Hybrid route formation strategy.	80
Figure 3.2.3 Bruker AXS D8 Discover Diffractometer.	83

Figure 3.2.4 popLA opening screen.	83
Figure 3.2.5 Position of the tension and compression test specimens.....	84
Figure 3.2.6. Wire EDM system.....	85
Figure 3.2.7.(a) MTS Teststar 3 system (b) MTS Insight electromechanical desktop test frame.....	86
Figure 3.3.1. Optical microscopy images from flow plane of the as-received sample S4 with magnifications (a) X300 (b) X1000 (c) X1000 and SEM images from flow plane of the as-received sample S4with magnifications (d) X1000 (e) X1000 (f) X5000.....	88
Figure 3.3.2. Optical microscopy images from extrusion plane of the as-received sample S4 of magnifications (a) X100 (b) X400 (c) X800 (d) X1000.....	89
Figure 3.3.3. Cross-sectional view of the ZK60 alloys extruded at 300 °C and at ratio 44 [33].	90
Figure 3.3.4. Prismatic and basal pole figures of S4 from (a) extrusion plane (b) flow plane.	91
Figure 3.3.5. (a) Compressive (b) tensile response of the as-received material.	93
Figure 3.3.6. S10 under optical microscope with magnifications of (a) X400 (b) X700 (c) X1000 (d) X1000.	96
Figure 3.3.7. S22 under optical microscope microscope with magnifications of (a) X2000 (b) X3000 (c) X4000 (d) X5000.	97
Figure 3.3.8. Pole figures of the ZK60 deformed in ECAE using different routes, 4 passes [109].	99
Figure 3.3.9. Prismatic and basal poles figures of (a) S4, (b) S11 and (c) S22.	100
Figure 3.3.10. Expected textures in the study.	103
Figure 3.3.11. Compressive response of (a) S10 and (b) S22.	103
Figure 3.3.12. Tensile response of (a) S10 and (b) S22.	106
Figure 3.3.13. S11 under optical microscope with magnifications of (a) X100 (b) X500 (c) X1000 (d) X1000 (e) X3000 (f) X5000.	111
Figure 3.3.14. Microstructural analysis on S11 (SEM images).	112

Figure 3.3.15. (a) Prismatic and basal pole figures of 4A processed ZK60 at 260 °C [28, 29]	114
Figure 3.3.16. Compressive response of (a) S10 and (b) S11.	115
Figure 3.3.17. Tensile response of (a) S10 and (b) S11.	116
Figure 3.3.18. Comparison of the basal fibers of (a) S10 and (b) S11.	118
Figure 3.3.19. Compressive response of S11 along three orthogonal directions.	123
Figure 3.3.20. Tensile response of S11 along three orthogonal directions.	124
Figure 3.3.21. Prismatic and basal pole figures of S11.	125
Figure 3.3.22. Microstructure of S27.	126
Figure 3.3.23. Prismatic and basal pole figures of S27.	127
Figure 3.3.24. Compressive response of S27 along three orthogonal directions.	128
Figure 3.3.25. Tensile response of S27 along three orthogonal directions.	128
Figure 3.3.26. Processed billet S21.	130
Figure 3.3.27. Microstructure of S21.	131
Figure 3.3.28. Prismatic and basal pole figures of S21.	131
Figure 3.3.29. Compressive response of S21 along three orthogonal directions.	132
Figure 3.3.30. Tensile response of S21 along three orthogonal directions.	133
Figure 3.3.31. Yield stress through the processing steps of S21.	134
Figure 3.3.32. Prismatic and basal pole figures for (a) S27 and (b) S21.	135
Figure 3.3.33. Optical microscopy images of S20 with magnifications of (a) X800, (b) X800, (c) X1000, (d) X1000.	137
Figure 3.3.34. Prismatic and basal pole figures for S20.	138
Figure 3.3.35. Compression test results of S20 in three orthogonal directions.	139
Figure 3.3.36. Peak splitting in S20.	140
Figure 3.3.37. Tensile test results of S20 in three orthogonal directions.	140

Figure 3.3.38. Characteristic prismatic and basal pole figures of a hot rolled plate.	141
Figure 3.3.39. Optical image of S28.	143
Figure 3.3.40. Prismatic and basal pole figures of S28.	144
Figure 3.3.41. Compressive response of S28 along three orthogonal directions.	145
Figure 3.3.42. Tensile response of S28 along three orthogonal directions.	146
Figure 3.3.43. Optical image of S23.	148
Figure 3.3.44. Prismatic and basal pole figures of S23.	149
Figure 3.3.45. Compressive response of S23 along three orthogonal directions.	149
Figure 3.3.46. Tensile response of S23 along three orthogonal directions.	150
Figure 3.3.47. S12 after ECAE (2A@200 °C).	154
Figure 3.3.48. Load vs. displacement curve for S12.	155
Figure 3.3.49. Failure of S13 due to extreme mushrooming (1A@ 200 °C). ...	158
Figure 3.3.50. Tensile behavior of S11 compared to its compressive behavior.	160
Figure 3.3.51. Stress differential values.	163

LIST OF TABLES

Table 3.1.1. Comparison of some physical properties of Mg, Fe and Al [34]...	44
Table 3.1.2. Standard four-part ASTM system of alloy and temper designations for magnesium alloys [38].....	47
Table 3.1.3. Independent slip systems for Mg [43].....	51
Table 3.1.4. The commonly observed twin systems in Mg [43].	56
Table 3.2.1. ECAE experiments.	81
Table 3.3.1. Mechanical properties of S4.....	92
Table 3.3.2. Mechanical properties of S10.....	104
Table 3.3.3. Mechanical properties of S22.....	104
Table 3.3.4. Mechanical properties of S11.....	117
Table 3.3.5. Mechanical properties of S11.....	124
Table 3.3.6. Mechanical properties of S27.....	129
Table 3.3.7. Mechanical properties of S21.....	133
Table 3.3.8. Mechanical properties of S20.....	141
Table 3.3.9. Mechanical properties of S28.....	147
Table 3.3.10. Mechanical properties of S23.....	150
Table 3.3.11. Stress differential values.	162

CHAPTER 1

INTRODUCTION

Ultra-fine grained (UFG) materials, having grain sizes in the submicrometer range, have always been the focus of interest and extensive research in materials science. The most important reasons for this interest and corresponding research activities are the unusual mechanical and physical properties that UFG materials possess, when compared to those of traditionally produced coarse-grained materials. This interest has grown significantly in the recent years with the development of several severe plastic deformation (SPD) methods which provide the opportunity to produce bulk UFG materials without many difficulties encountered during the prior fabrication methods. Of these SPD methods, equal channel angular extrusion (ECAE) is the most promising since the workpiece cross section does not change during the process.

ECAE is developed by Segal et al. [1] in 1981; and is exploited ever since. Now the process is extensively used to achieve ultra-fine grained structures in bulk form, which gives rise to attain the outstanding properties such as high strength, toughness and hardness at ambient temperatures, exhibition of superplastic behavior at high strain rates at elevated temperatures and so [2]. In ECAE process, two channels of the same cross section intersect at a certain angle to form the die. The billet, either of round or square cross section, is pushed from the top into this die by means of a flat faced ram and is subjected to simple shear without any change in cross sectional dimensions. By repeated pressings, the

workpiece can attain very large strains which are almost impossible to obtain via conventional manufacturing methods. However, one should pay much attention before exploring the application of ECAE in industrial practice. For a processed part to be employed in industrial applications, homogeneity throughout the workpiece should be attained since it has a direct impact on the product quality.

Regarding this, several analysis are employed; experimental, analytical or numerical, which aim to attain the best process performance in terms of process parameters like external die geometry, friction conditions, back pressure application, workpiece material properties, microstructural and textural evolution during the process, etc. Analytical studies can hardly include the effect of all of these parameters, but finite element method (FEM) is a very reliable tool to consider these effects to yield better analysis results and accordingly there are several studies employing FEM for ECAE process performance analysis. These findings, combined with the experimental experience yield improved process and material performance for a wide range of metals and alloys.

When it comes to material processing for industrial and research applications, the light metals call a great amount of interest. The property of lightness translates directly to the material property enhancement for many products since by far the greatest weight reduction is achieved by a decrease in density. The term “light metals” has traditionally been given to both aluminum and magnesium because they are frequently used to reduce the weight of components and structures. On this basis, titanium and beryllium also qualify and find their places in this group. This is quite expected since specific strength becomes one of the most important desired properties and is easier to be achieved due to the low densities of such materials

Of these alloys, Aluminum (Al) is the 3rd most abundant element in the earth's crust, ranking only behind oxygen and silicon. It makes up about 9% of the earth's crust, making it the most abundant of all metals. Accordingly, it is employed in a wide range of applications, mainly involving transportation, packaging, roofing, siding, door frames, screens, electrical appliances, automobile engines, heating and cooling systems, water purification, sewage treatment, etc.

Magnesium (Mg), being the 8th most abundant element on earth by mass, holds a very important place among non-ferrous metals as being the lightest structural metal [3]. Pure Mg is strong and light, with a density of only two-thirds that of aluminum and just over one-fifth that of iron; and its mechanical and physical properties can be easily improved upon the addition of alloying elements and different processing techniques.

Mg alloys, attracting a considerable amount of interest during and after World War 3, have been widely used in military and aerospace [4]. Due to the ever-increasing fuel costs since WW3 and environmental concerns, the demand for Mg alloys in civil applications has increased significantly. Striking specific mechanical properties are not their only advantage, but they also exhibit good physical properties. The metal is light, but conducts and radiates heat better than plastics. They maintain a metallic texture and they are non-magnetic. They can block electromagnetic waves and minimize the influence of noise. In addition, they are employed in several industrial parts, including automobile and truck components. They are also widely used for manufacturing of electronic devices and components such as laptop computers cases: portable electronic devices and mobile phone cases, housings of large-sized plasma panels. The one only disadvantage of the metal is the low workability.

Since the low workability makes the homogeneous deformation almost impossible, wrought components stood a step back in replacing other metals, which results in Mg alloys being more common in as-cast form. To increase the availability of wrought Mg components for applications, several techniques are readily available which would improve the formability of the alloys. The most important of these techniques involves processing at elevated temperatures.

High temperature ECAE processing of Mg alloys results in the activation of additional slip systems by decreasing their CRSS's, while twinning remains more active at lower temperatures. However, it should be remembered that Mg undergoes dynamic recrystallization (DRX) during not only in hot processing, but also during deformation at lower temperatures. Since DRX has a strong influence on the resulting microstructure, it should be carefully monitored to achieve the desired physical and mechanical properties.

The mechanical properties of HCP materials including Mg and its alloys depend highly on the texture evolution during deformation. Grain refinement associated with ECAE is not the sole matter of interest, but the way these alloys deform under different types of loading is also an interesting topic to investigate. As mentioned, such materials with strong textures are expected to exhibit anisotropy leading to tension/compression (T/C) asymmetry and distinct mechanical flow responses when mechanically tested. If the scientific literature is investigated, it can easily be observed that there are several studies on the flow stress anisotropy of Mg alloys under tensile and compressive loadings [5-13], and texture evolution [7, 14-21]; but there is limited data on T/C asymmetry of mechanical properties [7, 22-24]. Therefore, a comprehensive investigation of the deformation modes, texture evolution and resulting mechanical properties during and after ECAE is seen to be necessary.

This study is divided into two parts. The first part deals with the most abundant light metal on earth, Al and its alloys. FEM is used to study the ECAE of Al and its alloys, and the results are evaluated to optimize the processing conditions for better product homogeneity. The objectives of this part are stated as follows:

- Conduction of systematic studies to examine the effects of die geometry on the deformation homogeneity.
- Investigation of the effect of friction on the ECAE process and the final product.
- Analysis of corner gap formation during ECAE, the associated mechanisms and consequent product design.
- Determination of a corner gap prediction model as a function of material properties and the assurance of the model's validity.

The second part, on the other hand, investigates with the lightest of the light metals, Mg and its alloys. It is carried on an Mg alloy, ZK60 that is widely used in industrial applications. The alloy contains 5.5 wt% Zn and 0.5% wt% Zr. Zn is an extensively used alloying element for Mg alloys and it is used mainly for improvement of strength. Zr, on the other hand, is a very successful grain refining agent for Mg. The studies carried on ZK60 Mg in literature generally focus on contributions of the ECAE process on strength, microstructure and texture [25-32], but none of them considers all of these parameters in a single study to the best of our knowledge. Consequently, a detailed and systematic study which studies all of these parameters; the deformation modes, evolution of texture and mechanical properties during and after ECAE, and especially their combined effects, is required for this alloy system. Consequently, the obtained

results and conclusions can be employed in designing new processing routes for better mechanical property enhancements for ZK60; and increase the usage areas of the alloy in industrial and civilian applications.

To achieve this goal, several ECAE experiments are carried out in varying processing conditions. Hybrid routes are also developed besides the conventional routes. The microstructural and textural evolutions as well as the mechanical responses of ECAE processed materials are investigated. With the support of the data in literature, the governing deformation mechanisms are studied, and the process is worked to be optimized in order to achieve the desired mechanical properties for the specific applications; mainly a combination of good strength and ductility.

Consequently, the objectives of this part can be summarized as follows:

- ECAE processing of ZK60 Mg alloys with different processing routes and temperatures, utilizing temperature step-down method to develop hybrid ECAE routes with distinct crystallographic textures. The literature considers 200 °C a “low temperature” for the ECAE processing of Mg and its alloys. This worked aimed to go to lower temperatures and use the advantages of such processing conditions.
- Determination of the best processing conditions for to obtain a high strength and high ductility ZK60 Mg alloy by ECAE processing by studying the routes, passes, processing temperature, and resulting texture.

- Explore the effect of texture formation on the workability of ECAE processed ZK60 Mg alloy samples (by mechanical testing of the processed samples).
- Investigation of the relationship between the grain sizes and the activation of different deformation mechanisms.
- Exploration of the anisotropy in the mechanical response of ZK60 Mg alloy that is ECAE processed under different conditions and resulting textures.
- Conduction of systematic T/C asymmetry studies on the processed samples.

CHAPTER 2

FINITE ELEMENT MODELING OF ECAE OF ALUMINUM ALLOYS

2.1. Theoretical Background and Literature Review

2.1.1 Al and Its Alloys

Being the second most used metal on earth, the first commercial preparation of Aluminum occurred in France in 1855, when H. Sainte-Claire Deville reduced Aluminum chloride with sodium. The potential military applications of this metal led to a strategic importance and consecutively developed a wide range of industrial usage areas.

The largest single use of aluminum alloys is in the transportation industry. Car and truck manufacturers use aluminum alloys because they are strong, but lightweight. Another important use of aluminum alloys is in the packaging industry. Aluminum foil, drink cans, paint tubes, and containers for home products are all made of aluminum alloys. Other uses of aluminum alloys include window and door frames, screens, roofing, siding, electrical wires and appliances, automobile engines, heating and cooling systems, kitchen utensils, garden furniture, and heavy machinery.

Aluminum is also made into a large variety of compounds with many industrial and practical uses. Aluminum ammonium sulfate is used as a mordant, in water purification and sewage treatment systems, in paper production and the tanning of leather, and as a food additive.

Accordingly, new Al alloys and production or processing techniques are still developing in many research areas. Accordingly, the works on the metal are numerous; however, it is a perfect candidate for analytical and numerical studies when ECAE processing is considered.

2.1.2 Equal Channel Angular Extrusion (ECAE) and Its Applications on Al Alloys

ECAE is first introduced in literature by Segal in 1981. The publication is originally in Russian language, but it is cross referenced in almost all of the following publications on this subject. Segal, afterwards, carried out his research on ECAE process and published several papers both in Russian and English [2, 33-37].

In his first study, Segal defined the ECAE process as a pressing method in which two channels of the same cross section intersect at a certain angle to form the die. The billet, either of round or square cross section, is pushed from the top by means of a flat faced ram. Fig. 2.13 shows a schematic diagram of the process, where Φ is the die-channel angle commonly ranging from 90° to 150° . The angle of the corner curvature (central) angle is defined ψ which ranges from 0° to $(180^\circ - \Phi)$ [38]. The deformation is produced by simple shear as the specimen passes by the shear plane formed at the corner of the two channels. After that study, he continued working extensively on materials processing by simple shear and the effect of this deformation on material properties [2, 33],

and more importantly, he discussed the possible opportunities about engineering and commercialization of ECAE [36]. He concludes that ECAE should be optimized carefully in terms of process parameters in order to have an effective processing from practical point of view. This remark formed a base for all of the studies performed in this area after him. He also mentioned that ECAE can be used as a control tool for microstructure, texture, mechanical and physical properties [34].

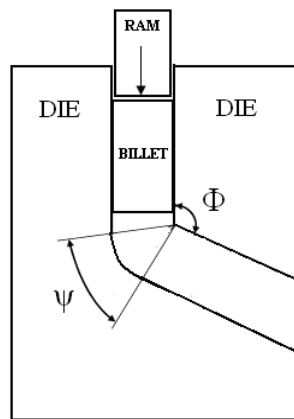


Figure 1.1.1. Schematic illustration of ECAE process.

During ECAE process, multiple passes can be applied by changing the billet orientation at each step in different strain paths; called the “routes”. The ECAE routes usually lead to different microstructure [39] and texture evolution [40] after ECAE. In route A, the billet’s orientation in the die does not change in the following passes, i.e. the face that is in contact with the front wall at the first pass is again in contact with the same wall during the consequent passes. This continuity increases the distortion of an imaginary element of the billet after each pass. As the number of passes increases, the imaginary element undergoes more and more distortion at the same direction, and a significant texture formation is expected. In route B, the billet is rotated by $\pm 90^\circ$ between each

consecutive passes, i.e. the face of the billet which is in contact with the front wall at the first pass contacts the first counterclockwise (CCW) wall after each odd numbered pass and the first clockwise (CW) wall after each even numbered pass. Route B_c involves rotation of the billet around its axis 90° in CCW direction after each pass. In route C, the billet is rotated by 180° around its axis after each pass. The face that is in contact with the front wall of the die comes in contact with the same wall before every even numbered pass. These conventional routes are shown in Figure 2.14. However, one should remember that it is not a must to follow these basic routes during ECAE processing. Combination or alterations of these routes can also be used. For example, the hybrid route E is developed as a combination of route C and B_C, where the billet is rotated by 180° and 90° before the even and odd-numbered passes, respectively.

Employing different routes, thus changing the orientation of the billet shall change the slip systems that are activated by the shear stresses as the billet is pushed around an internal angle. Activation of the different slip systems results in different textures and properties in the material. Thus, the internal angle of the die would be the most important factor in controlling the level of imposed strain to the billet. The central angle of the die, ψ , is also discussed to be an effective parameter in the produced strain. Valiev et al. report that the best die configuration would be $\psi=20$, and no arc curvature at the inner point of the intersection of the two channels [2], whereas there are different works in literature that mention the dies with central angle curvatures would lead to an increase in the inhomogeneities in the microstructure and resulting properties[41, 42].

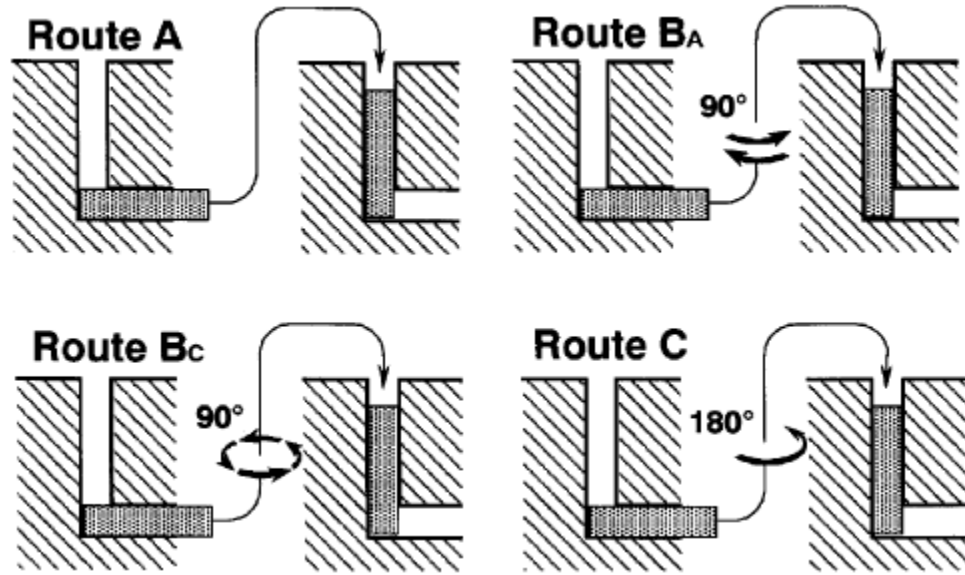


Figure 2.1.2. The four conventional processing routes in ECAE [76].

During ECAE, assuming that the surfaces of the die are frictionless, the billet moves inside the channel as a rigid body and fills the channel perfectly, and the billet deformation takes place homogeneously by simple shear at the plane of junction of two channels. Segal [33] developed the equation for total equivalent plastic strain formed during the process by using the slip line field theory as

$$\varepsilon = \frac{2}{3} \cot(\Phi) \quad (2.1.1)$$

Iwahashi et.al.[43] suggested a more extensive equation that includes the effects of central angle on total equivalent plastic strain as

$$\varepsilon = \frac{1}{3} 2 \cot \frac{\Phi}{2} + \frac{\psi}{2} + \psi \operatorname{cosec} \frac{\Phi}{2} + \frac{\psi}{2} \quad (2.1.2)$$

These equations ignore the effect of friction, which has the potential effect of ruining the homogeneity of the deformation. The strain here is assumed to be

dependent only on the die channel angle Φ and central angle ψ for a single pass, however; friction between contacting surfaces, deformation temperature, strain rate, dynamic and thermal properties influence the material flow and the deformation mechanisms during ECAE.

Segal's and Iwahashi's works were not the only ones that employ theoretical studies. Segal has two additional studies in which slip line field solutions are given for the ECAE problem [34, 35]. Horita et.al. described the principals of ECAE with emphasis on the shearing systems and the resulting deformation within the material [44]. Lee suggested an upper bound solution for the channel angular deformation (CAD) (in which two channels are not equal in cross section) [45]. ECAE is only a special case of CAD, and Lee made a stress analysis of the process general case. Another upper bound analysis was performed by Altan et al. [43]. Their model includes the effect of friction between the sample and the die walls, radius of the inner corner die and the dead metal zone. The authors also gave further directions for progresses in deformation analysis in SPD processes.

Ever since Segal's work, numerous studies were performed in the name of optimizing the process. These works use several tools with the real practice for optimization as discussed before. Slip line field and upper bound theories provided many theoretical information whose reliabilities were approved by experimental data and microstructural analysis. Besides these theoretical methods, finite element analysis provides a very effective and reliable tool for the evaluation of ECAE process.

2.1.3 Finite Element Modeling of ECAE

Being this much reliable, there are numerous publications on FE analysis of ECAE. The first publication on FE analysis of ECAE process came 16 years later, from Pragnell et al. [46].

Upon several publications in this area, Kim's works on the FE modeling of ECAE were very enlightening for the understanding of the process [47-50]. He extensively studied the material behavior of metals during ECAE. He proposed utilization of slanted workpieces for better strain homogeneity during the process. He also mentioned the usage of acute angle dies and their effects on deformation homogeneity. Moreover, he discussed the effects of die geometry, process parameters and the materials properties, yielding very valuable information for the ECAE researchers.

FE studies are easier to perform once the idea is grasped from the theory. Experimental work requires so much experience and can be degraded by several factors like die wear and fracture. Furthermore, it is not an easy job to modify the process parameters like die geometry or friction conditions in real practice, since each of these parameters require new die design and manufacturing. These drawbacks are readily overcome by numerous FEM studies in literature. The best way to present these studies is probably grouping them according to their area of concern.

The largest group of FEM studies on ECAE is formed by those which investigated the effect of die geometry on the process performance, namely the strain distribution and homogeneity [36, 49-60]. There are some inconsistencies in this group though [36], which led us to perform the simulations on the effect of die geometries once more by ourselves. These studies considered the

effect of φ and ψ , and it was concluded that increasing die channel angle φ decreases the total equivalent plastic strain accumulated in the material. Increasing central angle ψ has a pronounced effect only for 90° , whereas it almost does not contribute to deformation behavior for other die channel angles. Also, it was observed that the total equivalent plastic strain value cannot reach to those obtained by the equation considering only the effect of die channel angle, but not central angle or material properties. Moreover, for all die channel angles regardless of the central angle, the lower parts of the billet exhibit lower strain values compared to the upper regions. This strain inhomogeneity is due to the gap formed at the outer corner of the die.

The formation of the corner gap is investigated by another group of authors since it is a very important factor that deteriorates the strain homogeneity throughout the billet [48, 55, 61, 62]. The gap formation is due to the strain hardening characteristics of materials and occurs all the time unless the material is perfectly plastic. These studies observed the corner gap formation in the simulations and searched the factors causing this and the ways to minimize the effect of ruining of strain homogeneity due to this occurrence. Back slants and back pressures are suggested for the closure of the corner gap, and the effect of corner curvature is also discussed in terms of strain profiles. It should be kept in mind that none of the theoretical examinations take the corner gap formation into account, which makes these works crucial for the better understanding of workpiece behavior.

Another important simulation parameter is friction, which is inevitable in real practice. During the studies on friction [36, 41, 52, 56, 62-65], it was observed that when the friction coefficient is relatively low, the strain distribution is similar to the frictionless condition. Furthermore, the degree of inhomogeneity in deformation increases with increasing friction coefficients. Increasing the

friction more, the workpiece may exhibit a completely different behavior where the corner gap disappears but extensive strains are accumulated at the lower surface, leading to more inhomogeneous strain distributions. In practice, failures initiate at these points. This reminds us once again that friction analysis is also crucial for more reliable simulations and practice.

For square cross sectional billets, the problem reduces to a plain strain problem. A plane passing through the center of the die and billet can easily be simulated and the desired results are acceptable. However, for circular cross sections, this assumption obviously does not hold. Accordingly, there are also some studies which employ 3D simulations of circular cross sections [60, 64].

Another important assumption in most of the FE analysis is that the process is isothermal. In literature, there is a study which considers the temperature rise during the ECAE process [45]. The study concludes that the temperature rise at different locations can be very different. Also, it was strongly mentioned that both the workpiece and the pressing speed have a great influence on the temperature rise during ECAE.

Besides these numerous works on microstructural evolution and finite element modeling in ECAE, the combination of these two, namely a finite element model which evaluates and considers the microstructural changes during the running of the model are only a few [44, 66, 67]. This area is open for improvement.

2.2. Results

2.2.1. Effect of Die Geometry

The first model was constructed ECAE was simulated by using the commercial finite element modeling code Msc. Marc. For simplification of the problem, plane strain condition was assumed and a plane passing through the center of the die and billet was simulated accordingly. The process was accepted to be isothermal, although there are studies reporting temperature rise during ECAE [45]. A low ram speed of 1 mm/sec was employed. The die and the ram are assumed to be rigid (i.e., not undergo deformation during the process). A small fillet radius was given to the inner corner to avoid convergence problems. No damage criterion was considered. Simulations were carried out for a hypothetical material of which the flow stress changes with strain according to

$$\sigma = 150 + 250 * \varepsilon^{0.35} \quad (2.2.1)$$

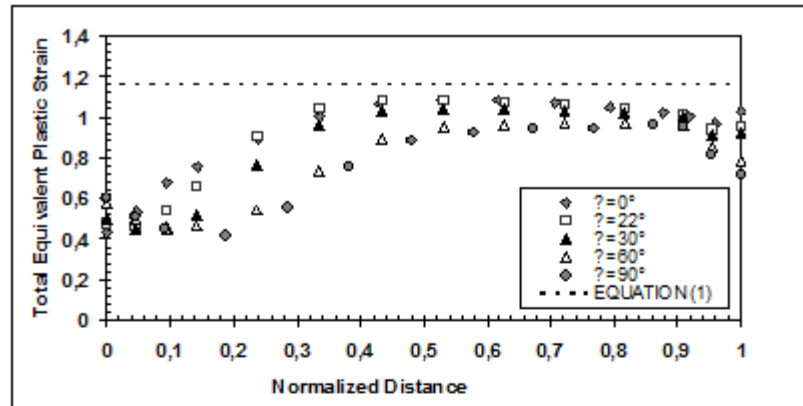
where σ is the flow stress in MPa, and ε is the equivalent plastic strain. Young's modulus of 69 GPa and Poisson's ratio of 0.33 was assigned to the material. The values are chosen to be in accordance with the Al alloys.

For the die channel angle, the commonly used values 90°, 120° and 150° [38] were chosen. Three different central angles of $\psi = 0^\circ$, 22° and 30° were considered for each and every die channel angle. Central angles of 60° for die channel angle of 120°; 60° and 90° for die channel angle of 90° were also studied to observe the effect of increasing corner curvature on deformation behavior and homogeneity. These values were chosen because they are the maximum values that a central angle can take considering the die geometry.

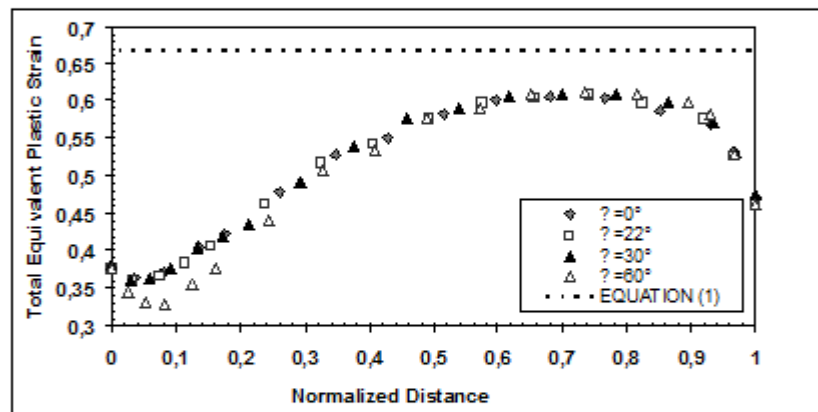
Deformation uniformity has the greatest effect on the grain refinement and resultant grain size and shape. Accordingly, homogeneity in strain distribution is essential to achieve a uniform grain size and shape and thus to attain the desired physical and mechanical properties. Any factor that destructs homogeneity of the deformation also spoils the expected properties.

The total equivalent plastic strain distribution along the cross section of the billet under frictionless conditions for die channel angles of 90° , 120° and 150° are given in Fig. 2.2.1 in terms of central angle. The exit channel data was collected from the regions where the deformation profile is almost uniform along the length. It was observed that the effective strain distribution is relatively uniform at the horizontal direction of the exit channel, whereas it is fairly non-uniform at the vertical cross section.

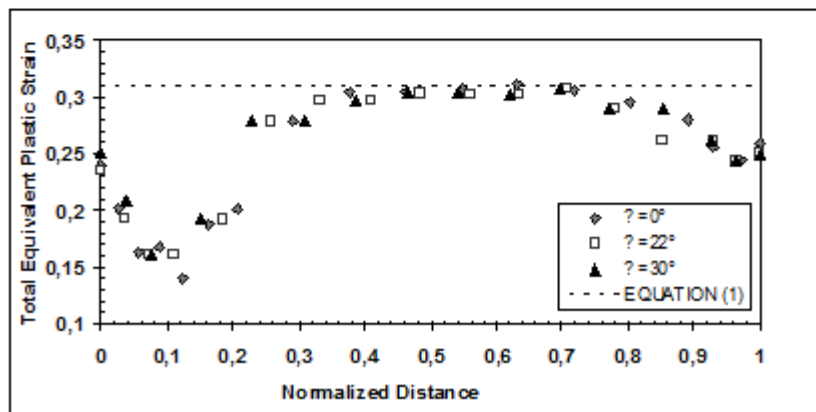
The effective strains have a general trend to exhibit a slight decrease around the outer surface, and a gradual increase from outer to inner parts. At the inner surface, a slight decrease is detected again. In the middle part of the cross section, constant strain values are achieved.



(a)



(b)



(c)

Figure 2.2.1. Effect of die geometry parameters on total equivalent plastic strain distributions for frictionless condition: (a) $\Phi=90^\circ$, (b) $\Phi=120^\circ$, and (c) $\Phi=150^\circ$. [68]

For the die channel angle (Φ) of 90° (Figure 2.2.1(a)), the effective strains decrease with increasing central angles however, this behavior is not pronounced for 120° and 150° . The effective strains exhibit a slight decrease around the outer surface, and a gradual increase from outer to inner parts. The largest difference between the maximum and minimum effective strain values is achieved in the billet. At the inner surface, a slight decrease is detected again. In the middle part of the cross section, a constant strain value is achieved. The first decrease in strain is not observed for central angle of 0° , however, the extent of the decrease in outer region increases with increasing central angle. Considering the behavior of die channel angle of 90° , it can be observed that the maximum strain is accumulated for central angle of 0° , where the strain distribution is also much more uniform. The extent of inhomogeneous deformation increases with increasing central angle.

For $\Phi=120^\circ$ (Figure 2.2.1 (b)), the effective strain behavior is nearly independent of the central angle. Neither the decrease in strain with increasing central angle is observed as in Figure 2.2.1 (a), nor has the central angle any significant effect on the vertical position where the strain behavior changes. The effective strain shows a slight decrease with increasing vertical distance, then increases, reaches a constant value and finally decreases, and exhibits this behavior for all central angles. The only noteworthy difference in deformation behaviors of different central angles is that slightly more reduction is observed in strain around the outer surface of the normalized distance of 0 to 0.2 for central angle of 60° .

For $\Phi=150^\circ$ (Figure 2.2.1 (c)), the effect of central angle is not much pronounced as well. The deformation behavior is similar to that of $\Phi=120^\circ$, but the primary decrease in strain is more pronounced. The strain distribution curve is smoother than those of other die channel angles. The accumulated strains are

much less, and the strain distribution curves are smoother than those of die channel angles of 90° and 120° .

As seen in Figure 2.2.1, the extent of severe plastic deformation and accumulated strain decrease with increasing die channel angle, reaching the maximum for $\Phi=90^\circ$. The central angles do not have a significant role which can alter this tendency. Inhomogeneities across the height of exit channel are due to corner gap formed during deformation. The strain values cannot reach to theoretical values of Equation (2.1.1) since it considers only the effect of die channel angle, but does not take into account any other parameters that can influence the deformation behavior and the resultant accumulated strains like material properties or other die geometry characteristics.

For all die channel angles regardless of the central angle, it was observed that the lower parts of the billet exhibit lower strain values compared to the upper regions. The reason seems to be the gap formed at the corner of the die (Figure 2.2.2). The strain hardening effect is more effective in the inner region which experiences more deformation, and therefore, this region becomes harder and shows higher resistance to further deformation. On the contrary, the outer part, subjected to less severe plastic deformation, flows more easily into the exit channel. This behavior forms the corner gap, which destructs the homogeneity of deformation throughout the billet. Accordingly, the sharpest die corners are not crucial for the process, as they are not filled completely. As strain hardening is the basis for gap formation, the gap does not form during deformation of a perfectly plastic material under frictionless conditions.

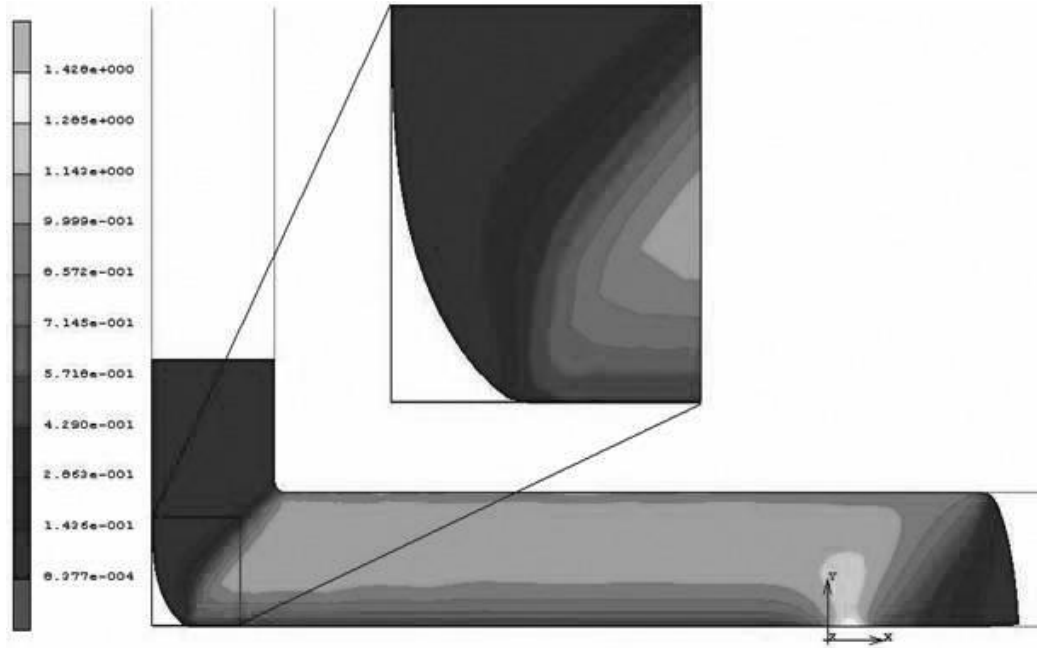


Figure 2.2.2. Corner gap for $\Phi=90^\circ$ and $\psi = 0^\circ$ die (frictionless condition). [68]

The corner gap reduces the strain formed at the outer region and increases it at the inner region of the billet. In the deformation zone, the material at the outside region moves faster and travels larger distances compared to that in the inner part. Thus, despite traveling faster, the outer part is literally left behind at the exit of deformation zone. Remembering that the velocity at the exit channel is the same at any point along the cross section, the differences in the strain behavior at the inner and outer regions are due to this velocity difference.

In literature, there are several studies which discuss the effects of process parameters and deformation behavior for die channel angle of 90° [36, 45-48, 52, 56, 59, 62, 65, 69, 70], but only a few are present to study deformations of $\Phi=120^\circ$ and $\Phi=150^\circ$ [38, 46]. The results obtained for $\Phi=90^\circ$ are in accordance with the studies reported in [36, 52, 59, 69], which points out that the magnitude of total equivalent plastic strain decreases with increasing central angle, but the

strain profiles are similar for different central angles across the billet. Total equivalent plastic strain decreases also with increasing die channel angles and larger die channel angles are capable of accumulating lower strains [38, 46, 52]. Strain distribution was also observed to be consistent with studies in literature [53].

2.2.2. Effect of Friction

Effect of friction was considered in the simulation with the die channel angle of 90° , and central angle of 0° . For this configuration, friction between the die walls and the billet is first neglected, and then considered with coefficients of 0.025, 0.05, 0.075, 0.1, 0.125 and 0.150, to have a clear understanding.

The effect of friction coefficient on strain distributions and deformation behavior are given in Figure 2.2.3 and Figure 2.2.4, respectively for deformations taking place at a right angle die with central angle of 0° .

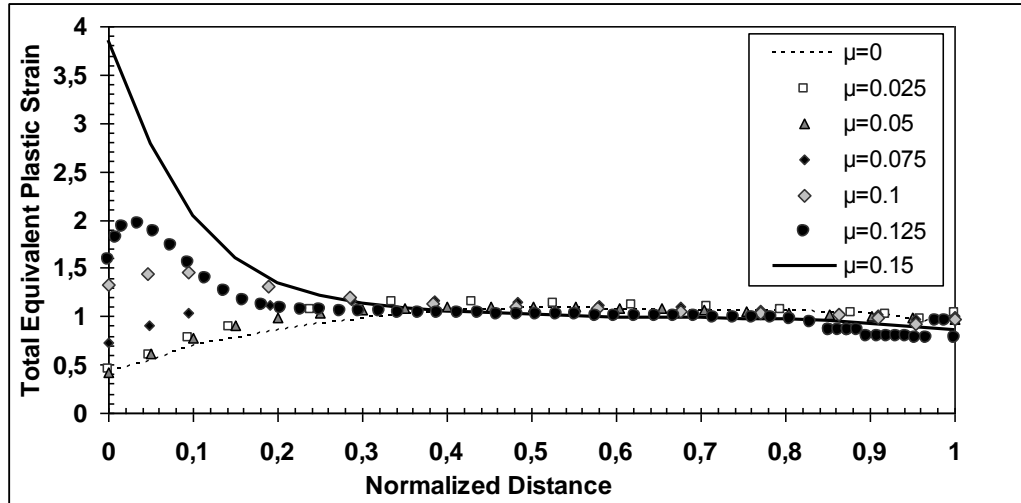


Figure 2.2.3. Effect of different friction conditions on total equivalent plastic strain distributions of a billet deformed in a right angle die with central angle of 0.[68]

Overall inhomogeneity of the deformation increases with increasing friction coefficient. Increasing friction coefficient results in a significant increase in the accumulated strains at the outer surface, whereas it does not have a major effect on those accumulated at the inner part. Friction intensifies the shear deformation at the surface, since it operates in the opposite direction to the motion of the moving surfaces and the friction induced by the outer region of the die limits the flow of the material through the outer corner. Thus, increasing the friction will increase the area of the less sheared zone at the outer surface.

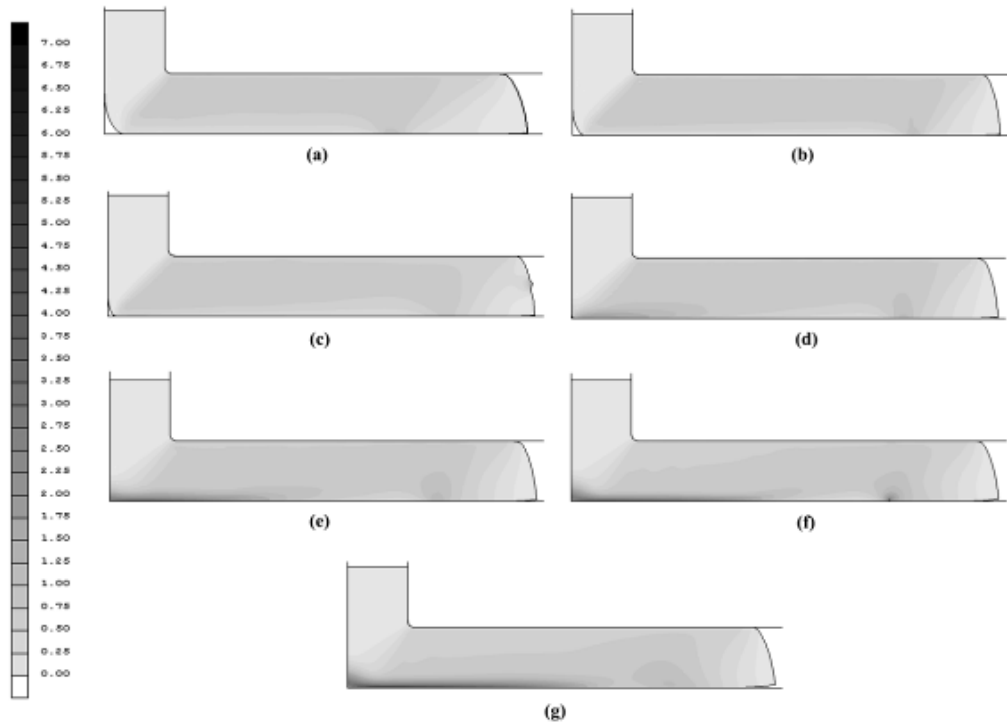


Figure 2.2.4. Strain distributions and deformation behavior of deformed billets: For the friction coefficients between the billet and the die walls of (a) 0, (b) 0.025, (c) 0.05, (d) 0.075, (e) 0.1, (f) 0.125 and (g) 0.15. [68]

With increasing friction coefficients, the corner gap becomes smaller and eventually disappears. The reduced gap which is present in the deformed billet of friction coefficient of 0.75 (Figure 2.2.4(c)) cannot be observed in the deformed sample with friction coefficient of 0.1. Instead, the gap is completely filled and the strains accumulated at the outer surfaces increased tremendously. For relatively small friction coefficient values, the deformation behavior resembles the frictionless conditions where a die corner gap is present and affects the strain homogeneity. Under these conditions, the strains observed at the outer regions of the billet are not very high or more truly, they are nearly the same with those observed under frictionless conditions.

However, when the friction coefficient increases more, corner gaps become filled and the outer surfaces where the larger strains are accumulated are more pronounced. For frictionless conditions, the lower strain values were attributed to the die corner gap. In the presence of friction, the gap is not present especially for high friction coefficients; and also opposing friction forces on the surfaces become more pronounced. As a result, increasing the friction coefficient makes the friction forces which oppose the flow become much more distinct and the inequality of the reaction forces between outer and inner regions arise. This forms the origin of the non-uniform deformation when friction is present. This behavior is consistent with data in literature [36, 52, 56, 62, 69]

2.2.3. Corner Gap Analysis in ECAE

The model is reconstructed to resemble ECAE of a rectangular billet having dimension of 10 mm × 50 mm in a die with $\Phi = 90^\circ$ and $\psi = 0^\circ$ in order to study the mechanism of corner gap formation. The billet was meshed into 2000 elements; with an average edge length of 0.5 mm. Global remeshing was employed when element distortion, strains and rotations reached to a critical value.

Simulations were carried out considering a “rigid plastic” material, whose constitutive behavior is described by Hollomon’s Law:

$$\bar{\sigma} = K\bar{\epsilon}_p^n \quad (2.2.2)$$

where $\bar{\sigma}$ is the flow stress, $\bar{\epsilon}_p$ is the equivalent plastic strain, K and n are the strain hardening coefficient and strain hardening exponent, respectively.

n is known to range from 0.05 to 0.5, for most of the metals, whereas K has a wider range of values for metals and alloys depending on the alloy system. However, for most of the light alloys, K is known to vary between 50-500 MPa. Several cases of stress-strain behavior are illustrated on Figure 2.2.5.

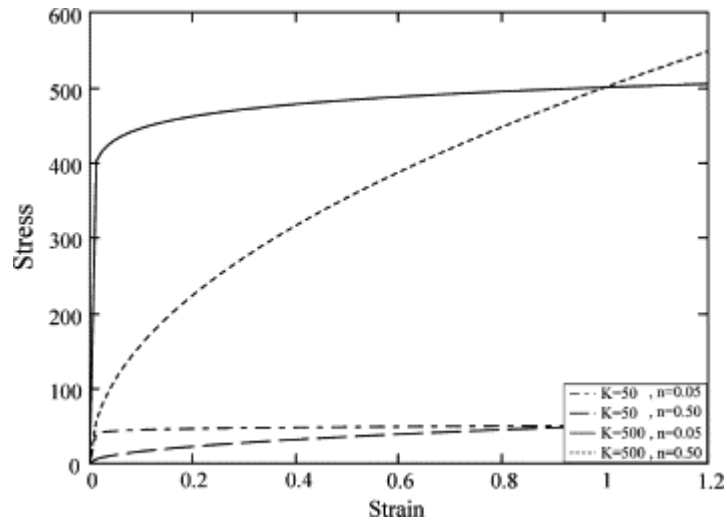


Figure 2.2.5. Stress–strain curves for extreme cases of Hollomon’s equation. [71]

In the simulations, K and n values were selected in 50-500 MPa range with 50 MPa increments and 0-0.5 range with 0.05 increments, respectively. All combinations of K and n values were used to investigate the effect of material properties, which gave rise to a total number of 100 simulations.

In the previous studies carried out by Bowen et al.[41], Dumoulin et al.[52], Nagasekhar et al.[55], and Wu and Baker[72], the die angle which provides the optimal combination of high strain per pass with reasonable homogeneity was found to be 90°. Thus, this die setup was also used in this study.

The results of the simulations are given in Figures 2.2.6 and 2.2.7. The corner gaps are represented in terms of angle “ α ” as defined in the Figure 2.1.1. Figure 2.2.6 shows the variation of the corner gap angle with strain hardening exponent “ n ”, for different strain hardening coefficient “ K ” values. It can be seen from the figure that in all of the simulations, regardless of the K value, an increase in the corner gap angle is associated with any increase in n . Figure 2.2.7 presents the dependence of the corner gap angle on K for different n values and it is observed that the corner gap angle exhibits a slight increase with increasing K values.

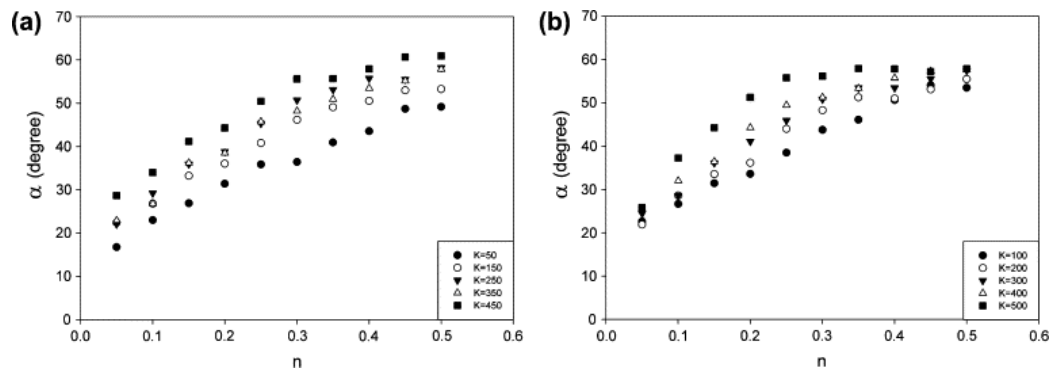


Figure 2.2.6. The variation of corner gap angle with strain hardening exponent (n) for different strain hardening coefficients (K). [73]

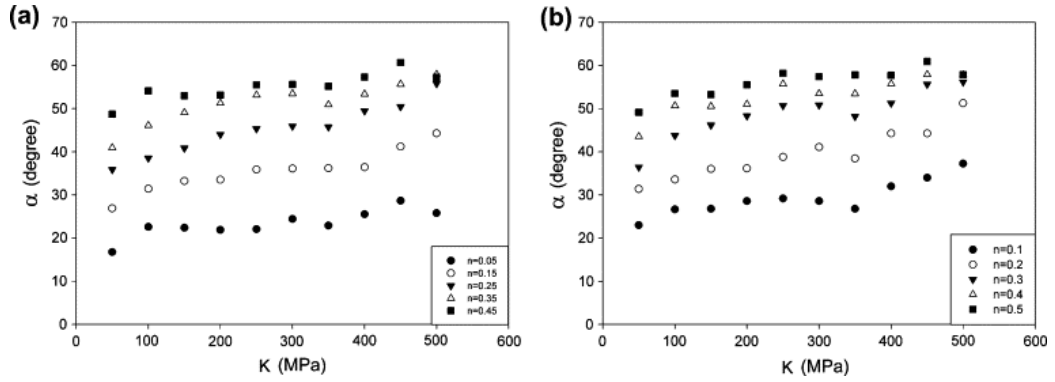


Figure 2.2.7. The variation of corner gap angle with strain hardening coefficient (K) for different strain hardening exponents (n). [73]

The combined effect of K and n on the corner gap angle is given as a three dimensional plot in Figure 2.3.8. The surface is represented by Equation (2.2.3) derived from multivariate regression analysis. This expression can be used to calculate the corner gap angle (α) for different materials.

$$\alpha_{K,n} = 0.02K + 75.43n + 0.09Kn - n + 15.43 \quad (2.2.3)$$

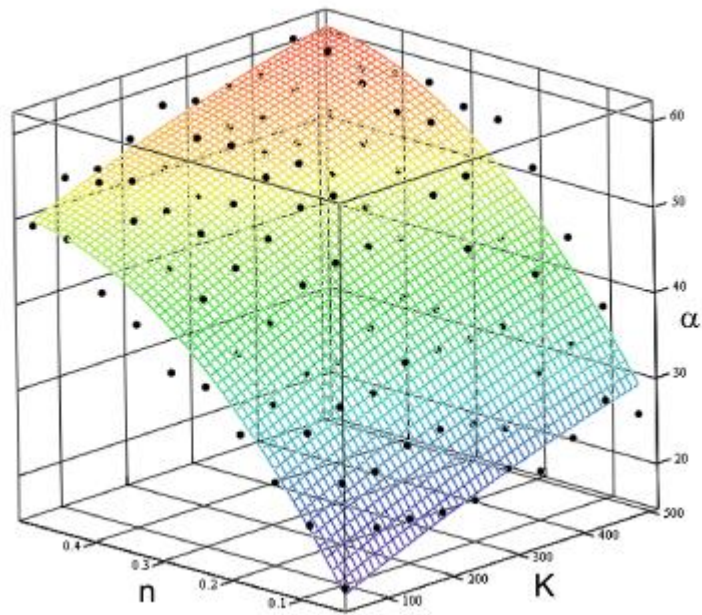


Figure 2.2.8. The combined effect of the strain hardening coefficient (K) and strain hardening exponent (n) on the corner gap angle (α). [71]

In literature, studies published by Bowen et al.[41], Kim et al.[47], Nagasekhar and Tick-Hon [53], and Wei et al [36] reported that the homogeneity of the deformation and the strain values in the billet was different from the ones expected in ideal shear. This difference was attributed to many different reasons, of which the gap formed at the corner of the die is the most significant. This finding may be exploited in process design. For this purpose, this study aimed to investigate the effect of material properties on the deformation behavior in terms of the dependence of the corner angle on strain hardening multiplier and strain hardening exponent of the Hollomon's law. The results of the simulations quantitatively relate the strain hardening behavior to the corner gap formation.

2.2.3.1. Mechanism of corner gap formation

The formation of the corner gap can be explained considering the flow velocity difference between the top and the bottom of the exit channel. The velocity in distributions during different stages of the process can be observed in Figure 2.2.9. Before the formation of the corner gap, there exists a large difference in velocities at the top and the bottom of the exit channel (Figure 2.2.9). This behavior persists during the formation of the corner gap. Once the corner gap is formed, the velocity profile becomes homogeneous at the exit channel.

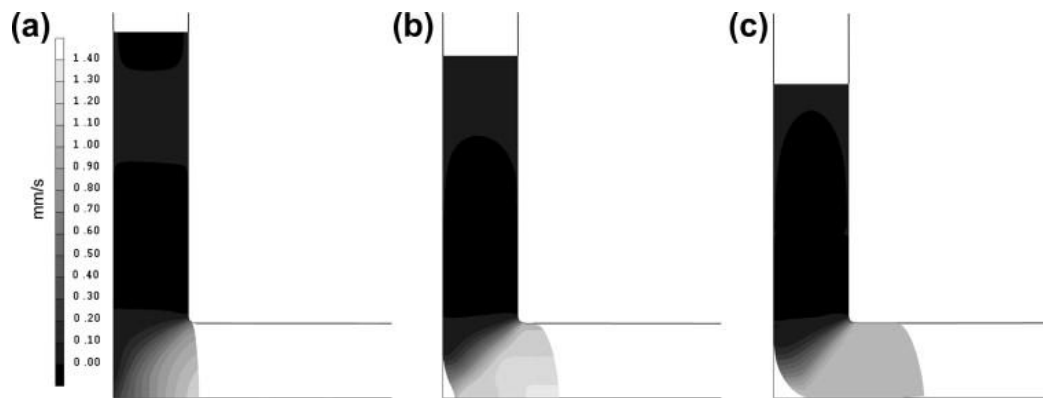


Figure 2.2. 9. Velocity profiles in the billet (a) before the formation of the corner gap, (b) during the formation of the corner gap and (c) after the formation of the corner gap.

[71]

The origin of velocity differences is the deformation history difference between the top and the bottom of the deformation zone. Path difference, friction and the flow stress variation in the deformation zone are the major causes of differences in deformation history. Path difference is negligible for small channel widths, which is a common case in ECAE studies. The friction amplifies the effect of the path difference but the effect of friction can also be neglected for small

friction coefficients if the friction conditions for the upper and lower die are the same. The flow stress variation is mainly due to the strain hardening of the material. According to Kim et al.[42], for a quasi-non strain hardening material, this difference is negligible, and hence no corner gap formation is observed for such kind of materials.

According to the flow rule, plastic strain increment is proportional to the variation of the yield functional with respect to the stress state. Thus, any factor that intensifies the variation of the local flow stress in the deformation zone will cause an increase in the flow velocity gradient. Practically, this variation may be due to the strain hardening or strain rate sensitivity of the material. In the case of strain hardening, this variation is in such a way that leads to larger corner gap formation. The effect of strain rate sensitivity is beyond the scope of this work and will be considered in another study. However, there are several studies that report formation of a gap between the upper part of the exit channel and the deformed workpiece during ECAE process, for strain rate sensitive materials.

During ECAE process, material near the upper die corner experiences larger strains at the initial stage, leading to higher local hardening. On the other hand, the material near the bottom of the exit channel can flow easier since its motion is less restricted, resulting in a smaller amount of local hardening. At the subsequent stages, hardened regions flow slower than less hardened material as a consequence of the flow rule. This variation of the flow velocity in the cross-section of the exit channel leads to formation of a corner gap. It should be noted that this explanation also clarifies the observed lower shear strains at the bottom part of the pressed billet.

In this sense, it is reasonable to observe an increase in α in more strain hardening materials, having high K and n values. This behavior is clearly observed

in Figures 2.2.6 and 2.2.7. Although most of the studies on corner gap formation report the increase of the corner gap due to increasing n [51],[52], [42], the effect of K is usually neglected. It is obvious that for an ideally plastic material ($n = 0$), no corner gap would form independent of the K value. However, for a strain hardening material, K intensifies the flow stress gradient, and hence, the velocity gradient in the deformation zone. Although its effect may be neglected for small values of n , neglecting the effect of K for large values cause a considerable error in predictions.

2.2.3.2. Process design considering material characteristics

Homogeneity of strain distribution can be improved by minimizing the velocity gradient in the deformation zone. A simple way for this is to optimize the corner curvature (ψ). Figure 2.2.10 illustrates the analysis results for dies with $\psi = 0^\circ$, 30° , 57° and 90° , for a hypothetical material with $K = 300$ and $n = 0.5$. It can be seen that the strain distribution in the billet pressed through the die with $\psi = 30^\circ$ is more homogeneous than the one pressed through a die with $\psi = 0^\circ$, as also stated by the authors in a previous study [68]. But the most homogeneous strain distribution is obtained when $\psi = 57^\circ$, which is almost equal to the calculated corner gap angle (α) for this material. The simulations of Yoon et al. [74], also supports this finding. The corner curvature during ECAE process can be generated because of inherent strain hardening behavior or it can be forced by die design as long as “forced” corner angle is greater than corner gap angle of the material. Thus, one can conclude that the strain homogeneity is mainly influenced by corner curvature regardless of its generation mechanism. However, use of a die with a corner angle close to corner gap angle provides some other advantages which will be clarified in this section. Accordingly, die corner curvature which can be calculated by Equation 2.2.3 are advised for a better process performance.

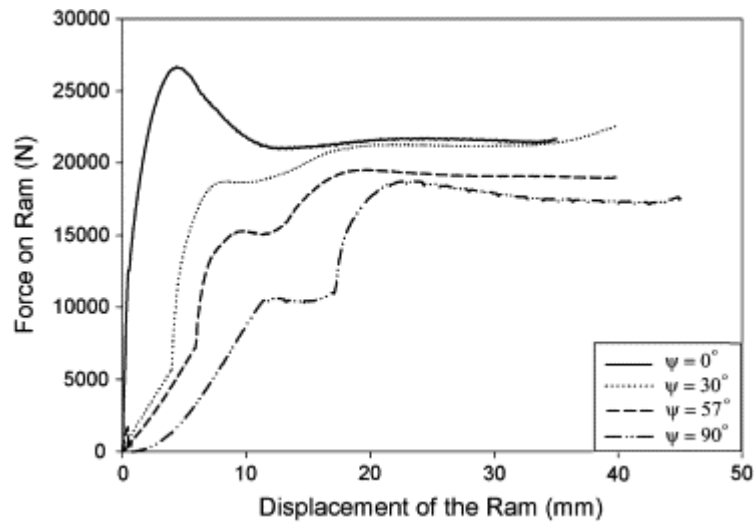


Figure 2.2.10. The effect of ψ on force–displacement curve of the ram. [71]

One of advantages of designing a die with $\psi = \alpha$ is the decrease in the probability of failure and the increase in the length along which the strain distribution is homogeneous. When $\psi = 0^\circ$, the motion of the metal near the bottom corner of the die is highly restricted. This restriction results in accumulation of plastic deformation in this region, which can even trigger failure. On the contrary, when $\psi = \alpha$, the motion of those particles become easier, and the strain does not localize at these points. Consequently, the length along which the strain distribution is homogeneous increases. This behavior can be observed in Figure 2.2.11. For $\psi = 0^\circ$, there is an accumulation of strain up to a value of 1.5 at the lower part of the billet, which may cause damage or failure. When $\psi = 30^\circ$, the accumulated strain decreases, but still has the potential to generate failure. For the condition in which $\psi = \alpha$, the region where the strain is accumulated can hardly be observed. The decreasing trend of localized deformation calls attention to the cases where $\psi > \alpha$, but this time exit channel gap formation, which deteriorates the strain homogeneity, is observed at the upper part of the billet.

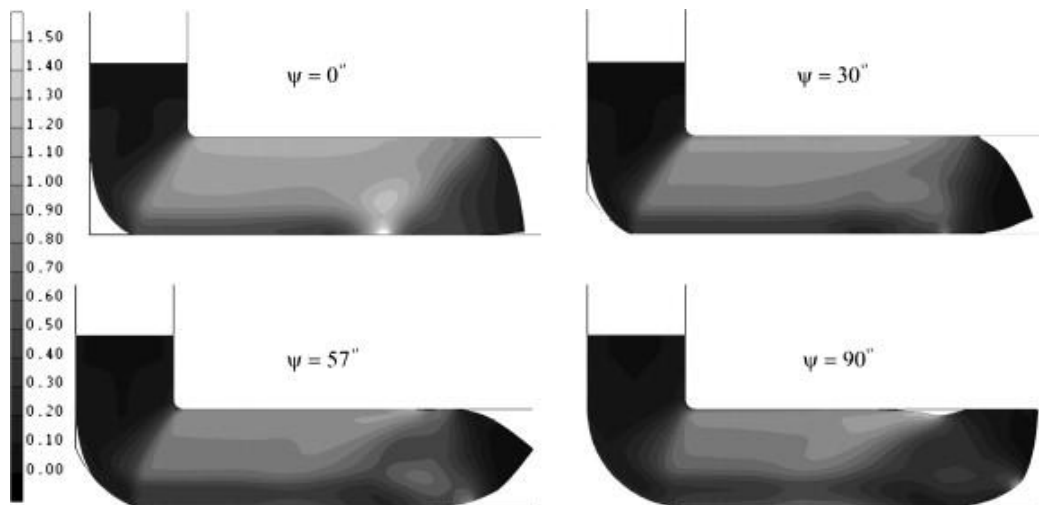


Figure 2.2.11. The distribution of equivalent plastic strain for dies with $\psi = 0^\circ$, 30° , 57° and 90° . [71]

Another advantage of designing a die with $\psi = \alpha$ is the reduction of the ram pressure. The decrease in ram pressure provides not only a reduction in energy requirement for the process, but also facilitates the die design due to smaller reaction forces. Moreover, such a design improves the force–displacement characteristics of the process. Figure 2.2.10 illustrates the force exerted on the ram vs. displacement curves for different corner curvatures. The curves exhibit different behaviors at different stages of deformation. For the case of simulations, that is $\psi = 0$, the punch pressure exhibits a unique behavior; initial increasing, decreasing, and steady state. The initial increasing trend in the punch pressure develops while the severely constrained front part of the workpiece passes through the deformation zone. The following decrease on the force–displacement curve for $\psi = 0^\circ$ is simply due to corner gap formation. Corner gap formation provides a relaxation by a reduction of constraints and the deformation proceeds almost at steady state thereafter. The initial increasing trend is observed in all ψ values. However, the punch pressure is observed to

reach to higher levels for $\psi = 0$ and the increasing trend is interrupted (even accompanied with a short plateau or a minor decrease for a while) for increasing ψ values. This interruption is due to the front part of the workpiece leaving the deformation zone and bending upwards into the exit channel. Since there are much fewer constraints in the exit channel and the billet can move more freely, a decrease in the punch pressure is observed. The reason for the bending upwards in the exit channel is the prevention of the straight downward motion of the billet which is observed in the case $\psi = 0$, and early contact of the workpiece with the die where there exists a curvature in the outer wall. The drastic decrease in punch pressure after the corner gap formation for the case $\psi = 0$ cannot be observed that much seriously in increasing ψ values and almost disappears for $\psi = 90$. This is due to ease or difficulty of the formation of the corner gap in the situations with different ψ values. For $\psi = 0$, the workpiece is obliged to form a corner gap to obey the flow rules, and once the gap formation is completed, it relaxes and flows easier. However, for the case where ψ is 90° , the material flows through the deformation zone as if a corner gap was already formed in the beginning; even the very first flow profile resembles the conditions after the completion of a corner gap in a sharp corner die. This can also explain the lower values of the maximum punch pressures achieved in these circumstances. Although the required force and energy when $\psi = 90^\circ$ is the lowest, the homogeneity of strain distribution is ruined due to formation of an exit channel gap. Those results are also supported by the former findings of Kim [42].

2.2.3.3. Validity of the equation for corner gap estimation

The validity of Equation 2.2.3 can be investigated by comparing the data obtained by it with the data in the literature. Accordingly, study performed by Alkorta and Sevillano [51] is considered, in which, the authors conducted an

upper bound analysis for determination of the punch pressure and came up with the following expression:

$$P_{ECAE} = \frac{K}{1+n} \frac{2 \cot \frac{\phi+\psi}{2} + \psi}{3}^{1+n} \quad (2.2.4)$$

where K and n are the strain hardening coefficient and strain hardening exponent, respectively, and ϕ and ψ are the die channel angle and the corner curvature angle respectively.

Equation 2.2.4 is evaluated for randomly chosen K and n values to determine the punch pressure. ϕ and ψ values are taken to be 90° and 0° respectively, as employed in the finite element model. The results obtained by this upper bound evaluation are given in Figure 2.2.12. For comparison reasons, the loads obtained from finite element analysis are also presented in the corresponding figures. The punch pressures given in the figure are evaluated as the average value they attain at the plateau region appearing in the punch pressure vs. displacement profiles. Considering the figure, it should be noted that the analytical results give only an upper bound limit for the punch pressure values.

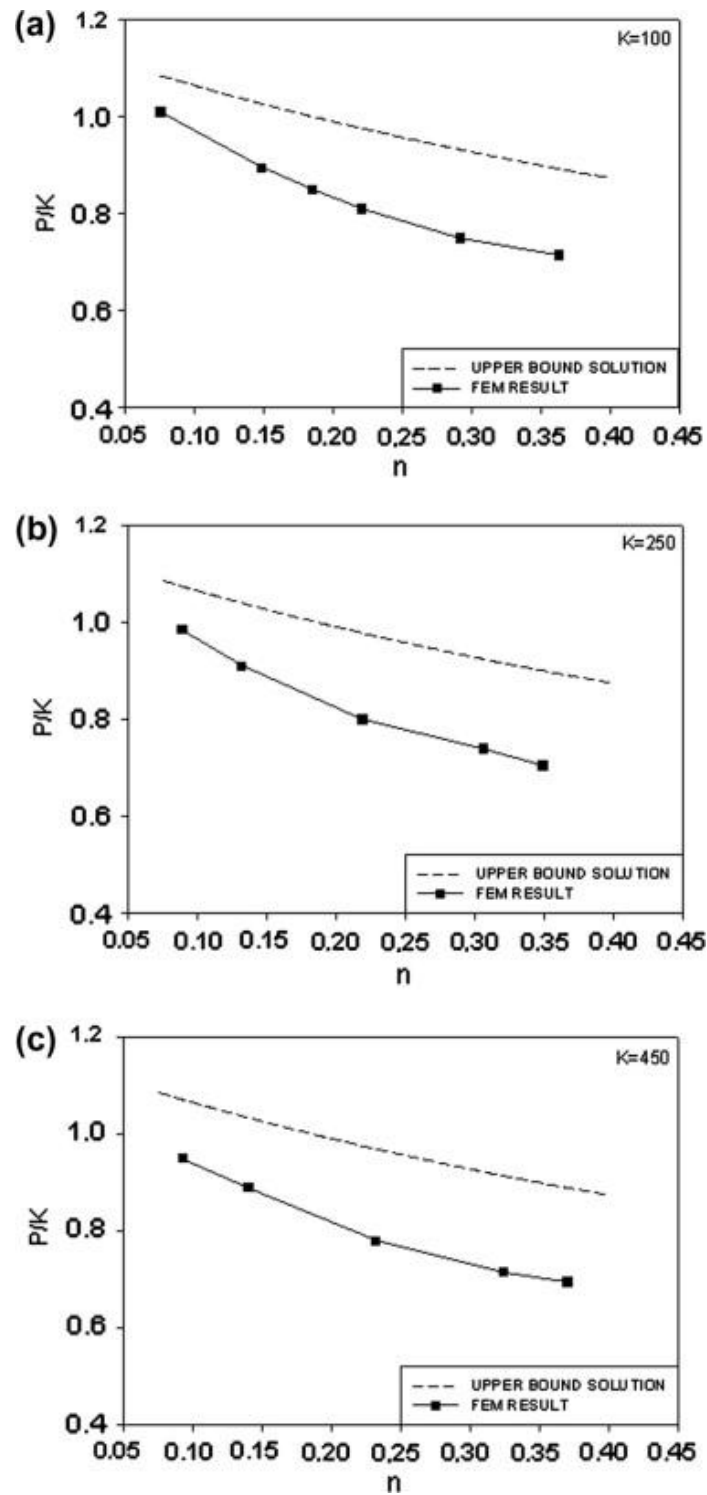


Figure 2.2.12. Comparison of the punch pressure values obtained by FEM and upper bound analysis. [71]

In the same study, the plastic strain is given by:

$$\varepsilon_p = \frac{2 \cot\left(\frac{\phi + \varphi}{2}\right) + \varphi}{\sqrt{3}} \quad (2.2.5)$$

Figure 2.2.13 gives a comparison of the strain values obtained by the finite element and upper bound analysis. The most significant reason for the difference in the strain values of upper bound and finite element analysis; and the inhomogeneities in strain profiles at finite element results is the formation of the corner gap, as discussed before.

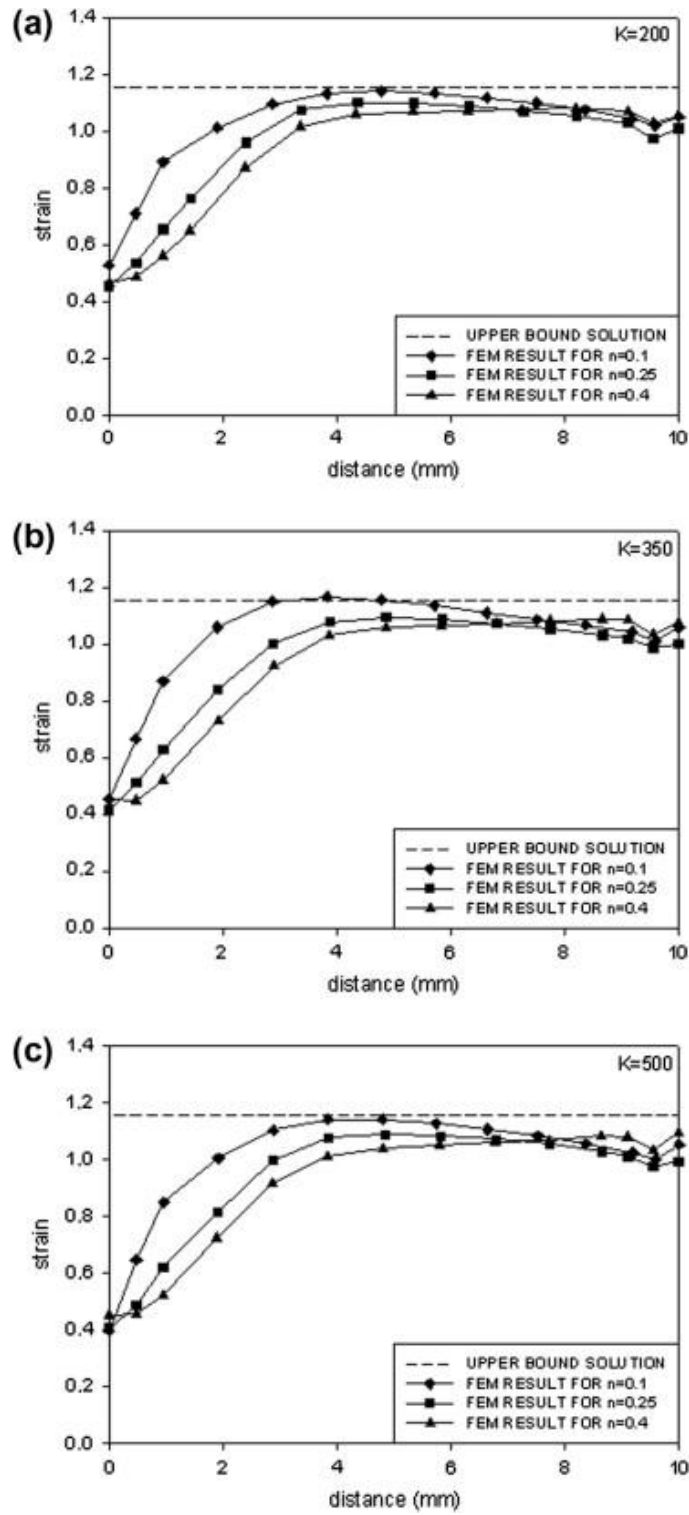


Figure 2.2.13. Comparison of the strain values obtained by FEM and upper bound analysis. [71]

2.3. Conclusion

Material properties are important parameters that influence the ECAE performance and should be considered beside the external parameters during the process design. This study aimed to investigate, quantitatively, the dependence of the corner gap angle on strain hardening behavior of the billet. The effects of die geometry and friction on the total plastic equivalent strain distribution and deformation behavior for determining the optimum process parameters to attain strain homogeneity were also discussed. According to the results of finite element simulations, following conclusions can briefly be drawn:

- Increasing die channel angle decreases the total equivalent plastic strain accumulated in the material. Increasing central angle has a pronounced effect only for 90° , whereas it almost does not contribute to deformation behavior for other die channel angles.
- Total equivalent plastic strain value cannot reach to those obtained by the equation considering only the effect of die channel angle, but not central angle or material properties.
- For all die channel angles regardless of the central angle, the lower parts of the billet exhibit lower strain values compared to the upper regions. This strain inhomogeneity is due to the gap formed at the outer corner of the die.
- For the conditions where friction is present, the origin of nonuniform deformation is based on two main reasons: corner gap formation and the inequality of the reaction forces between outer and inner regions.

- When the friction coefficient is relatively low, the strain distribution is similar to the frictionless condition.
- The degree of inhomogeneity in deformation increases with increasing friction coefficients. Increasing the friction more, the billet exhibits a completely different behavior where the corner gap disappears but extensive strains are accumulated at the lower surface, leading to more inhomogeneous strain distributions.
- Both the strain hardening exponent (n) and the strain hardening coefficient (K) affect the corner gap formation and strain homogeneity.
- Design of an ECAE die, where the corner curvature is equal to the corner gap angle, improves strain homogeneity, decreases the ram pressure, probability of failure and improves the load–displacement characteristics of the process.
- An analytical expression, covering a wide range of light structural alloys, to predict the corner gap angle considering the combined effect of strain hardening exponent and strain hardening coefficient was derived by multivariate regression analysis of the simulation results. ECAE process designers may use this expression as a simple tool that eliminates the need of performing time consuming simulations.

CHAPTER 3

INVESTIGATION OF TEXTURE EVOLUTION AND MECHANICAL FLOW RESPONSE AND ANISOTROPY IN ZK60 MAGNESIUM ALLOY PROCESSED BY EQUAL CHANNEL ANGULAR PRESSING

3.1 Theoretical Background and Literature Review

3.1.1 Mg and its alloys

Magnesium is the 8th most abundant element on earth by mass and constitutes about 2 percent of the Earth's crust. Magnesium in pure metal form metal was first produced by Sir Humphry Davy in 1808 as a product of reduction of magnesium oxide with potassium vapor. However, the metal and its alloys have been considered as industrial structural materials in the late 1920's and early 1930's. Mg-Al-Zn and Mg-Mn alloys were the most commonly used systems until around 1950s. Table 3.1.1 shows some of the mechanical and physical properties of Mg and its competent, iron and even Aluminum. Today, Mg and its alloys are employed in very wide range of applications as alternatives of iron and even of Aluminum, in the name of reducing the weight of the structural components.

Table 3.1.1. Comparison of some physical properties of Mg, Fe and Al [34].

Metal	Specific gravity (gr/cm ³)	Melting point (°C)	Tensile strength (MPa)	Elongation (%)	Hardness (HB)
Mg	1.74	650	98	5	30
Al	2.74	660	88	45	23
Fe	7.86	1535	265	45	67

Pure Magnesium is the lightest of all structural metals. Besides this particular advantage, it also has the important physical properties like as electromagnetic wave shielding, dent resistance and vibration damping [75]. However, the metal suffers from low strength levels, heat and corrosion resistance. For employment in structural applications, these shortcomings should be overcome. Alloying with the proper amount of elements made the ideal solution for this situation. Luo and Pekguleryuz proposed that the alloying elements for Magnesium can be grouped into three [76]:

- The elements that increase the ductility, but offers a little strengthening effect: Cd, Tl and Li; in that order of effectiveness;
- The elements that intensely contribute to strengthening, but at the cost of ductility; Sn, Pb, Bi and Sb in the order of effectiveness;
- The elements that increase both strength and ductility: which can be subdivided into two, as Al, Zn, Ca, Ag, Ce, Ga, Ni, Cu, Th; being the most effective ones to increase the strength, in that order; and Th, Ga, Zn, Ag, Ce, Ca, Al, Ni, Cu as the efficient alloying elements to impose high ductility.

Considering alloying, Aluminum (Al) and Zinc (Zn) are the main additions to Mg. They are used for both cast and wrought alloys to increase the strength. It is reported that the yield strength of the Mg alloy increases with increasing Zn content [41]. Another alloying element, Lithium (Li) increases the ductility and impact strength while reducing the density. It also reduces the difference between tensile and compressive yield strengths; i.e. reduces T/C asymmetry. Zirconium (Zr) additions result in significant reduction in the grain size of the alloy. When it is used with rare earth (RE) elements, the result is a significant increase in tensile strength and ductility, not only at room temperature, but also at high temperatures like 200 °C. Other than these, several alloying additions are possible as mentioned above. A general overview of these alloys with accompanying properties is given in Figure 3.1.1.

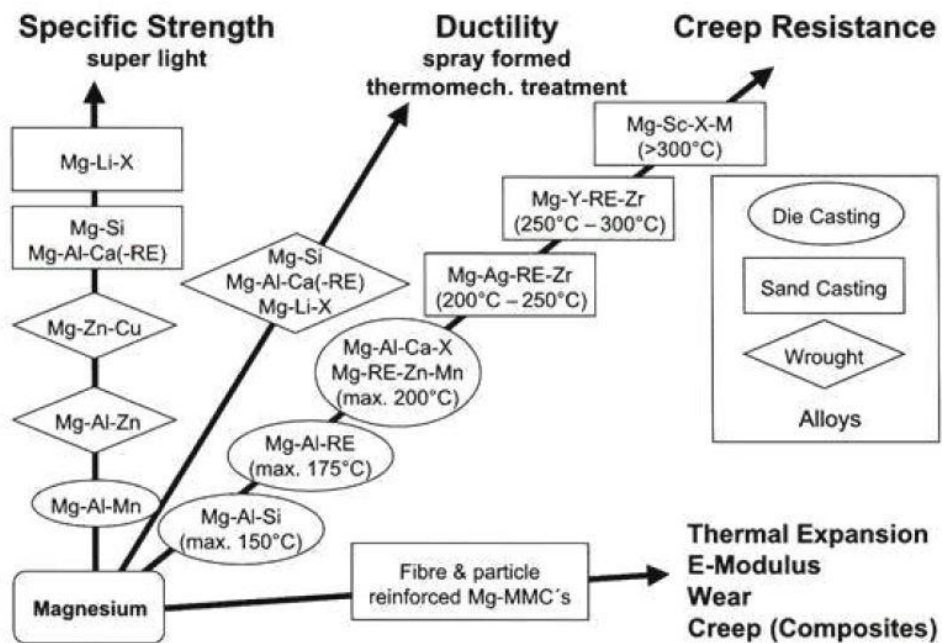


Figure 3.1.1. Effect of alloying elements for Mg on several mechanical properties [77]

Since it can be alloyed with several elements, a common nomenclature was developed for Mg. This alloy designation is given in Table 3.1.2.

Table 3.1.2. Standard four-part ASTM system of alloy and temper designations for magnesium alloys [38].

First Part	Second Part	Third Part	Fourth Part
Indicates the two principal alloying elements	Indicates the amounts of the two principal alloying elements	Distinguishes between different alloys with the same percentages of the two principal alloying elements	Indicates condition (temper)
Consists of two code letters representing the two main alloying elements arranged in order of decreasing percentage (or alphabetically if percentages are equal)	Consists of two numbers corresponding to rounded-off percentages of the two main alloying elements and arranged in same order as in first part	Consists of a letter of the alphabet assigned in order as compositions become standard	Consists of a letter followed by a number (separated from the third part of the designation by a hyphen)
A-aluminum B-bismuth C-copper D-cadmium E-rare earth F-iron G-magnesium H-thorium K-zirconium L-lithium M-manganese N-nickel P-lead Q-silver R-chromium S-silicon T-tin W-yttrium G-magnesium H-thorium K-zirconium L-lithium M-manganese N-nickel P-lead Q-silver R-chromium S-silicon T-tin W-yttrium Y-antimony Z-zinc	Whole numbers	Letters of alphabet except I and O	F-as fabricated O-as annealed H10 and H11-slightly strain hardened H23,H24 and H26-F-as fabricated O-as annealed H10 and H11-slightly strain hardened H23,H24 and H26-strain hardened and partially annealed T4-solution heat treated T5-artificially aged only T6-solution heat treated and artificially aged T8-solution heat treated, cold worked and artificially aged

Considering ZK60A-T5, as an example, the first part, ZK, shows that Zinc and Zirconium are the two principal alloying elements. The numerical part, 60, gives the weight percentages of Zinc and Zirconium roughly; the alloy contains 5.5% Zn and 0.5% Zr. The third part, A, indicates that this is the first alloy standardized with 5.5% Zn and 0.5%Zr as the principal alloying additions. The fourth part, T5, denotes that the alloy is artificially aged only.

AZ series are the most widely employed alloys in structural and daily life applications. ZK series are comparatively newer, and are second in line despite exhibiting better mechanical properties than AZ series. The main reason for this is the high price of the alloying element Zr. Nevertheless, they are coveting for the demand to the AZ series. ZK60 belongs to this group, and is the most promising and common alloy in the series.

ZK60, the alloy to be investigated in this study, is only supplied in the form of extruded bars and rods. As any other HCP material, its workability is low due to the limited slip activity at room temperature.

3.1.2 Deformation of Mg and its alloys

Magnesium has HCP crystal structure and is usually demonstrated by a hexagonal prism. The atomic positions are shown in Figure 3.1.2.

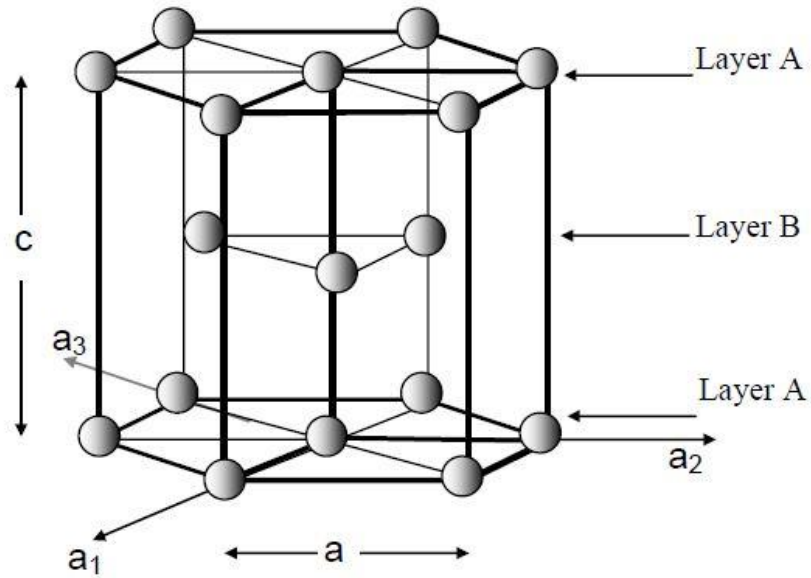


Figure 3.1.2.HCP crystal structure.

Unlike metals with cubic structures, HCP crystals exhibit relatively lower active deformation modes, which results in the necessity of combination of activation of different deformation modes to fulfill Taylor's homogeneous deformation criterion. Deformation slip, the most common deformation mode for metals, is observed in HCP materials in different systems. Basal $\langle a \rangle$ slip takes most of the deformation since it has the lowest CRSS among the others; however, it only provides two independent slip systems. Besides, it does not accommodate the c-axis deformation by itself; thus other deformation modes are necessary for homogeneous deformation. Deformation slip is not the only deformation mode observed; twinning has an important role for the deformation of HCP crystal structures. The contribution of twinning to total strain is not as high as crystallographic slip, but the significant lattice changes associated with twinning may orient the lattice in such a way that further slip can take place.

3.1.2.1 Crystallographic slip

It is basic materials science knowledge that crystallographic slip occurs when the stress acting on the slip plane exceeds the CRSS of that plane. The active slip systems in Magnesium and its alloys are shown in Figure 3.1.3. The plastic deformation of Mg and its alloys in terms of slip is accommodated mainly by the glide of $\langle a \rangle$ type dislocations on (0001) basal plane and 1010 prismatic planes, the glide of $\langle c+a \rangle$ type dislocations on 1122 pyramidal planes. Basal and prismatic slip systems belong to $\langle a \rangle$ group, whereas the pyramidal slip system may be of either $\langle a \rangle$ or $\langle c+a \rangle$ groups.

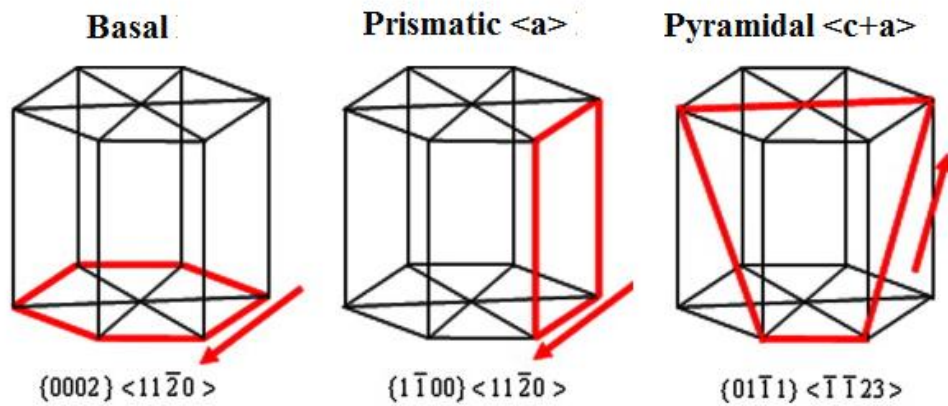


Figure 3.1. 3. Active slip systems in Mg and its alloys [78].

For a polycrystalline material to be able to be deformed successfully, each and every single grain that composes the structure should undergo the same shape change with the structure. This requires each individual grain to be deformed with the same strain as the body. For a grain, this shape change is defined by independent strains, ϵ_1 , ϵ_2 , γ_{12} , γ_{23} , γ_{31} , in the rectangular coordinate system. Consequently, as discussed before, five independent slip systems are required to achieve sizeable amount of ductility, considering that there are no other

deformation mechanisms involved. The absence of these five independent slip systems would result in inhomogeneous deformation, even failure. The independent slip systems for Mg are given in Table 3.1.3.

Table 3.1.3. Independent slip systems for Mg [43].

Slip plane	Slip direction	Number of slip systems	
		Total	Independent
Basal {0001}	$\langle a \rangle$ type, $\langle 1120 \rangle$	3	2
Prismatic {1010}	$\langle a \rangle$ type, $\langle 1120 \rangle$	3	2
Pyramidal {1011}	$\langle a \rangle$ type, $\langle 1120 \rangle$	6	4
Pyramidal {1122}	$\langle c+a \rangle$ type, $\langle 1123 \rangle$	6	4

As observed from the table, it is almost impossible to achieve five independent slip systems for Mg. This is due to the low symmetric nature of the HCP structure.

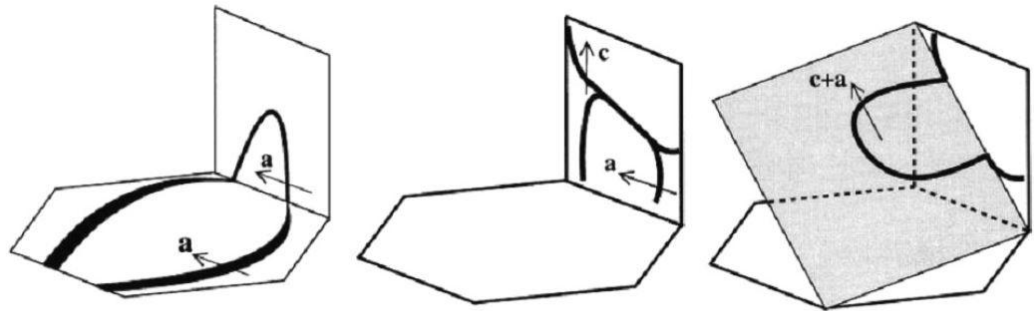
The predominant active slip system for Mg is the basal slip. The main reason for this is that the CRSS for basal slip at room temperature is almost 1/100 of the non-basal slip systems on prismatic and pyramidal planes [18]. As a result, plastic deformation is considered to take place by basal slip. In such a case, the basal slip system provides only two independent slip system, which is not enough to fulfill the necessary five independent systems for homogeneous deformation. Accordingly, other slip systems are operated, in the order of decreasing ease of operation. The next easiest slip system for deformation of Mg is the prismatic $\langle a \rangle$ slip; with the components (0001) $\langle 1120 \rangle$, pyramidal $\langle a \rangle$ slip of (1010) $\langle 1120 \rangle$, and pyramidal $\langle c+a \rangle$ slip with (1122) $\langle 1123 \rangle$.

For Mg and its alloys, there is a decrease by two orders of magnitude in the CRSS for prismatic slip when the temperature is increased. Furthermore, the activation of the non-basal slip systems can also be improved by additions of the element Y and form Mg-Y binary alloys [78]. In their study, they also showed that the forest dislocation hardening due to activation of the non-basal slip system played an important in the strengthening of Mg-Y alloys.

The $\langle c+a \rangle$ slip in Mg is an important system since it provides four independent slip systems for deformation. Besides, it is the only slip mode that contributes the c-axis deformation. Yoo et al. [79] extensively investigated the stability of $\langle c+a \rangle$ dislocations and their mobility in HCP. Their simulation analysis and texture measurements demonstrated that the $\langle c+a \rangle$ dislocations play an important role in the texture evolution of Mg alloys. Another study on texture evolution of AZ31 alloy [80] studied the tensile test of the extruded form from room temperature up to 250 °C. The authors reported the direct evidence for the high activity of the $\langle c+a \rangle$ slip system for temperatures $\geq 200^\circ\text{C}$.

The possible model for source mechanism for non-basal $\langle c+a \rangle$ slip dislocation, proposed by Yoo et.al. [79] suggests that the source generation takes place in three steps. First, cross-slipping of $\langle a \rangle$ dislocation occurs, and the segment of this dislocation forms a $\langle c+a \rangle$ junction at the prismatic plane. The third step is the cross-slipping of these junctions. Remembering that in a polycrystalline material, grain boundaries are possible sites for generation of pyramidal slip, particularly at triple grain junctions [26]. The incoherent twin boundaries inside the grains also generate $\langle c+a \rangle$ dislocations. In deformed Ti, Mg, and Be samples, $\langle c+a \rangle$ dislocations were not observed at TEM investigations, even though they are responsible for the compressive deformation along the c-axis. When found, they were usually observed in conjunction with $\langle a \rangle$ and $\langle c \rangle$ dislocations, as shown in Figure 3.1.4 [26]. The activity of non-basal slip

systems also plays an important role in dynamic recovery of Mg alloys, which has been experimentally proved to be contributed to the improvement of the ductility [18].



(a) Cross-slip of $\langle a \rangle$ dislocation (b) $\langle c+a \rangle$ junction formation (c) cross-slip of $\langle c+a \rangle$ dislocation

Figure 3.1. 4. The possible model for source mechanism for non-basal $\langle c+a \rangle$ slip dislocation [26].

3.1.2.2 Deformation twinning

Twins in FCC and BCC materials is rare except at low temperature or high strain rates. Twinning in HCP materials is much more important than in BCC and FCC materials in which slip systems can accommodate deformation in any direction. This is because the number of slip systems in HCP materials is limited and all easy slip direction $\langle 1120 \rangle$ or $\langle a \rangle$ are perpendicular to c -axis. Therefore, slip does not produce any elongation or shortening parallel to c -axis.

There are two types of twinning in Mg alloys: $(1012) \langle 1011 \rangle$ extension (tensile) or $(1011) \langle 1012 \rangle$ contraction (compressive), depending on whether twinning results in elongation or reduction in the c -axis length. The activation of each of these mechanisms depends on the material, the temperature, and the strain rate [81]. At room temperature, the two dominant deformation modes of Mg alloys are basal slip and $(1012) \langle 1011 \rangle$ twinning [27, 28]. As temperature

increases, the activation of non-basal slips becomes more favorable owing to the lowered CRSS; twinning becomes less critical; thus a better formability can be observed. According to Yoo [14, 82], the mode of twinning that would take place depends on the c/a ratio of the HCP metal. The critical value of this ratio is 1.633, since this situation results in a square shear plane and the twinning shear becomes zero. If the c/a ratio is less than 1.633, (1012) twin helps to extend along the c -axis, and it is called “tensile twin”, as in the case of Mg and its alloys.

In contrast with slip, twinning produces a homogeneous shear distributed over a three dimensional region. The effect of twinning in terms of strain is quite small; however, it has significant effects on overall deformation. During the initial stages of deformation, twinned regions act as barriers to dislocation motion, causing strain hardening. On the other hand, twinning that takes place at the later stages are capable of reorienting the basal planes and make the basal slip favorable. Another important property of twins is that it provides grain nucleation sites during recrystallization and increase the amount of fine grains and the rate of nucleation.

The tensile and compressive twin systems are visualized in Figure 3.1.5 for Mg and its alloys.

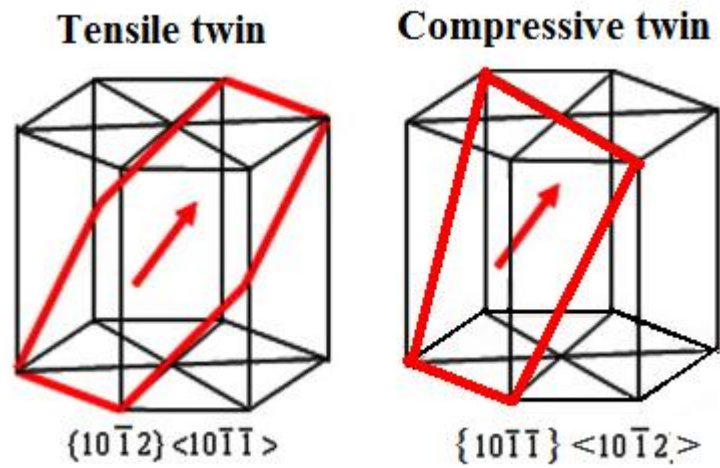


Figure 3.1.5. The most common twin systems in Mg and its alloys [83].

Going into a little more detail on tensile twinning that generally occurs in Mg and its alloys, the crystallographic elements for twin and produced by (1120) plane are shown in Figure 3.1.6.

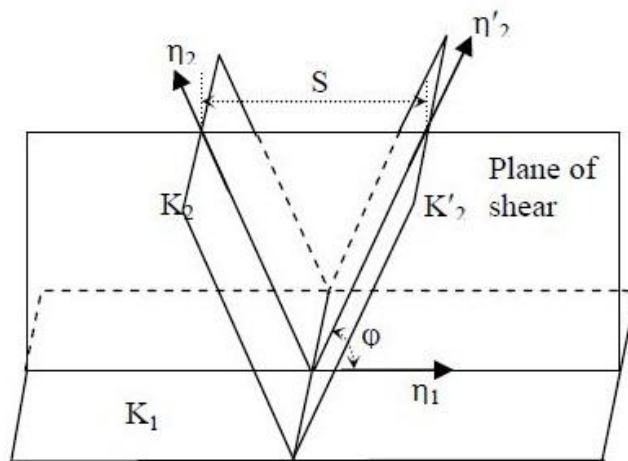


Figure 3.1.6. Crystallographic elements of twin [84].

There are two planes that remain undistorted by the twinning shear (K_1 and K_2). While the twinning plane K_1 , containing the twinning shear direction η_1 , does

not change its position, K_2 displaces to K_2' by the twinning shear. The cross-sections between the plane of shear and K_2 (K_2') are denoted by η_2 (η_2').

The twinning shear S varies with c/a ratio, the acute angle ϕ between K_1 and K_2 is related to the amount of twinning shear S , associated with this twin depends on c/a ratio and is defined as;

$$s = \left(\frac{c}{a}\right)^2 - 3 \frac{\sqrt{3}a}{3c} \quad 3.1.1$$

Therefore, if $c/a > \sqrt{3}$, the sign of the shear strain is negative and hence twinning occur under tension (Zn and Cd). For all other, $c/a < \sqrt{3}$, twin $(1012) \langle 1011 \rangle$ occurs under compression, as in Mg.

Defining these parameters, twinning systems in HCP materials can be restated. Table 3.1.4 presents the twinning planes commonly observed in magnesium and its alloys [83].

Table 3.1. 4. The commonly observed twin systems in Mg [43].

K_1	K_2	η_1	η_2	S
{1012}	{1012}	$\langle 1011 \rangle$	$\langle 1011 \rangle$	0.130
{1011}	{1013}	$\langle 1012 \rangle$	$\langle 3032 \rangle$	0.137
{1121}	{0001}	$\langle 1126 \rangle$	$\langle 1020 \rangle$	0.616
{1122}	{1123}	$\langle 1124 \rangle$	$\langle 2243 \rangle$	0.260

The crystal shape changes followed by $\{10\bar{1}2\}$ twin produce the 4° tilting of $\{10\bar{1}2\}K_2$ plane and simultaneously 86.18° rotation of basal plane, shown in Figure 3.1.7. Because the c/a ratio in Mg is slightly smaller than the ideal case, the symmetry conditions require the second undistorted plane, K_2 , to be tilted clockwise; in reverse case the K_2 plane rotates counter-clockwise. This has an effect of lengthening the crystal inside the twinned volume in a direction perpendicular to basal plane. That is, the tensile stress perpendicular to basal plane, or compression parallel to basal plane, favors $\{10\bar{1}2\}$ twinning in Mg.

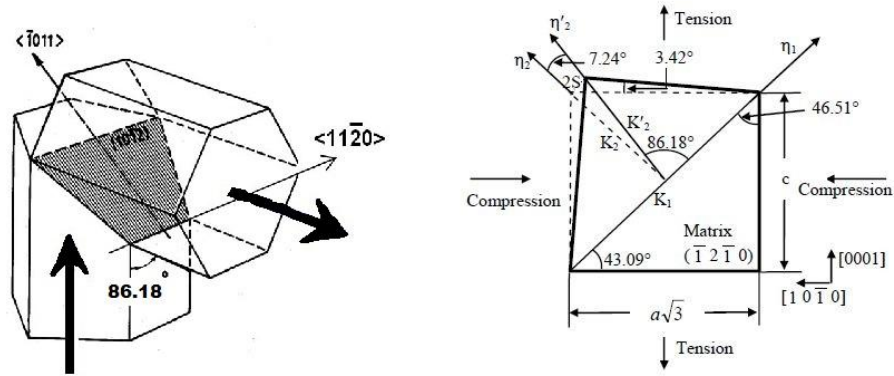


Figure 3.1.7. Shape change produced by $(10\bar{1}2)$ twinning [60].

As grain sizes decrease, more energy (higher average stress) is required to produce the same volume fraction of twin.

3.1.3 Development and measurement of crystallographic texture

The orientation of hundreds of thousands of crystals cannot be presented in a single numeric value like other physical and mechanical properties, rather it is presented graphically. Most of these materials contain grains with lattice orientations that are not random, but instead are clustered to some degree about

a particular orientation or about a set of orientations. Structures in which the grains are oriented non-randomly are said to have a preferred orientation or texture. An extensive knowledge on the texture of a polycrystalline sample is of fundamental importance in science and industry.

Texture deserves much of attention due to the important effects it has on the properties the materials. A fine grained material in which the grains have random lattice orientations will possess identical properties in all directions, but a specimen with a preferred orientation will have anisotropic properties that may be desirable or undesirable depending on the purpose of the application.

Deformation, casting, processing, welding and heat treatments can cause a reorientation of the lattice of individual grains of a polycrystalline material and tend to develop a texture of the lattice in the grains, as well as a preferred change of shape of grains. However, one should remember that the presence of elongated or flattened grains does not always imply a certain texture or even the presence of any texture at all; as the presence of the equiaxed grains does not necessarily have random texture.

Because of the low symmetry in HCP lattice, the crystallographic texture is more important in these materials than in other materials having lattices of high symmetry, like FCC and BCC crystals. The texture development in HCP metals strongly depends on the axial ratio (c/a ratio) of the lattice, because it determines the closed packed plane and direction along which the crystallographic slip takes place. When the c/a ratios are above the ideal value of 1.633 such as in Cd and Zn, it tends to exhibit textures with basal poles tilted 15° to 25° away from the normal direction toward the rolling direction and the $\langle 1010 \rangle$ prismatic poles show the maximum in the transverse direction, so called r-type (rolling type) texture, as shown in Figure 3.1.8 (a) [39].

When the c/a ratio is approximately equal to the ideal value of 1.633, such as in Mg and Co, the textures are developed with tendency of basal fiber texture, the so called c-type (center type) texture, as shown in Figure 3.1.8 (b). Metals and alloys with below ideal c/a ratios, such as Zr and Ti, tend to form textures with basal poles tilted 20° to 40° away from the normal direction towards the transverse direction, and $\langle 1010 \rangle$ prismatic poles are aligned with the rolling direction as shown in Figure Figure 3.1.8 (c). The categorization by c/a ratio is, however, a rather crude approach because many other factors influence the texture development; like strain rate, temperature and chemical composition. All those factors have direct or indirect relation to the activity of a deformation mode, and the large variety of deformation textures in hexagonal metals are actually due to the fact that the different combinations of slip and/or twinning modes cause different textures.

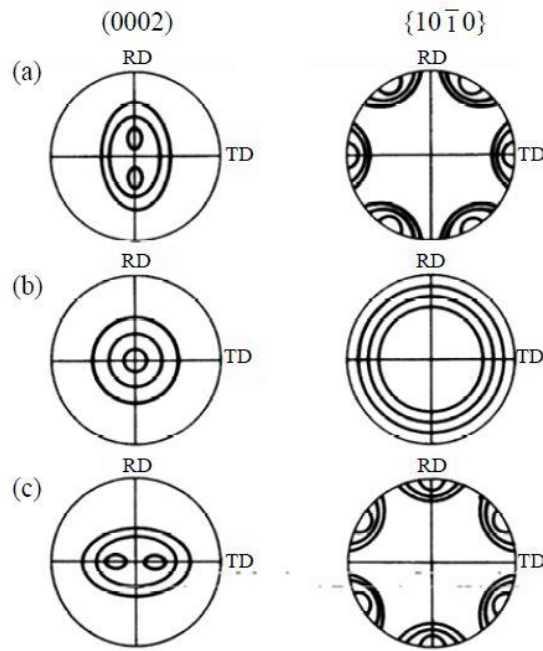


Figure 3.1. 8. Schematic rolling textures in HCP metals with different c/a ratios [84]. When the deformation modes are considered, this grouping of texture formation can be expressed on different basis. For example, a splitting of the basal poles towards the rolling direction in Mg alloys, as in Figure 3.1.8 (a), due to the activation of $\langle 10\bar{1}2 \rangle$ twinning is reported in literature [84]. During a uni-axial deformation such as round extrusion, however, a $\langle 10\bar{1}0 \rangle$ fiber texture, in which the normals of the basal planes are perpendicular to the main deformation axis is most likely to be formed. This texture has been observed in extruded round rods of HCP metals like Mg, Ti [85], Zr [86] and Be [87].

The type of fiber texture also varies according to the deformation temperature and the alloying elements, as mentioned. For example, pure Mg shows the ring type fiber-texture, in which all crystallographic directions in basal plane can be laid parallel to extrusion direction. On the other hand, $\langle 10\bar{1}0 \rangle$ fiber-texture was observed in Mg alloy having Al, Mn and Zn after extrusion, while Mg alloy with 2 wt.% of Mn showed a double fiber-texture consisting of $\langle 10\bar{1}0 \rangle$ and $\langle 11\bar{2}0 \rangle$

fibers. In Mg alloys all of three texture types have been observed depending on alloying elements, temperature and deformation methods. The development of c-type texture has been frequently observed in various Mg alloys, e.g. in Mg after hot rolling [88], in AZ31 alloy after hot and cold rolling [89, 90], and in AZ61 after hot rolling and annealing [91]. Similar with Ti and Zr, the c-texture formation is caused mainly by basal $\langle a \rangle$ slip. The splitting of the basal pole towards the rolling direction in (0002) pole figure, r- type texture, has been reported by many authors after hot working of AZ31 [92] and AM60 [93]. Agnew et al. [94] simulated the evolution of r-type texture during plain strain compression of Mg-Li and Mg-Y alloys. They found that a good correlation with the experimentally observed r-type textures was obtained when an increasing activity of $\langle c + a \rangle$ slip is taken into account on top of basal $\langle a \rangle$ slip and twinning. Dillamore [87] explained the splitting of the basal pole in the extruded bar by employing the double twinning mechanism. In their study, Barnett et al.[90] reported on an EBSD observation of $\langle 1010 \rangle$ - $\langle 1012 \rangle$ double twinned structure in cold rolled Mg alloys, however, it occurs in a very small volume. In addition, they verified the existence of 20° tilted basal pole toward the rolling direction in shear band that was nucleated in the double twinned area.

Knowing the texture of a material, one can predict the mechanical response along any direction. Consequently, texture evolution can be employed for controlling the mechanical properties of the material. There are several factors that influence texture development; like the initial texture, active deformation mechanisms and deformation conditions defined by die angle, processing route, and number of passes [95]. Slight differences of any of these factors can result in significant differences in the final texture.

In texture evolution area, the most important studies are published by Los Alamos National Laboratory team, Tome, Beyerlein, et al. [96-104]. The team is also very well-known with the viscoplastic self-consistent (VPSC) model they developed for texture prediction. The model is extensively employed in the studies on modeling of texture evolution [98-100, 102, 103, 105-111].

3.1.3.1 Crystallographic texture measurement

There are two techniques for presenting the crystallographic texture, namely the pole figures and the orientation distribution function (ODF). The pole figure describes the 3-dimensional distribution in 2-dimension based on the stereographic projection. On the other hand, the Orientation Distribution Function (ODF) is based on the three Euler angles of rotation required to coordinate a unit cell with a reference coordinate system.

For describing the orientation distribution, two coordinate systems are introduced. As a coordinate system fixed in the sample, $K_A = (X, Y, Z)$, the exterior shape is generally used. The second coordinate system is defined as $K_B = (X', Y', Z')$, which is fixed in the crystal-axes following the crystal symmetry, e.g. (1010), (1120) and (0001) in case of hexagonal structure. These two coordinate systems are related each other with an orientation g , as followed.

$$K_B = g \cdot K_A \quad (3.1.2)$$

As the equation states, the K_A is transformed by g into the K_B .

The orientation g can be presented in some different ways, for example, by Miller-indices (hkil) [u v t w] or by Euler angles ($\varphi_1, \Phi, \varphi_2$), Figure 3.1.9. The

Euler angles are defined by rotation angles around 3 fixed axes, by which the crystal coordinate system becomes matched with the sample coordinate system. The crystal coordinate system is firstly rotated about the Z' -axis through the angle φ_1 , secondly about the X' -axis (in its new orientation) through Φ and, thirdly, once again about the Z' -axis (in its new orientation) through the angle φ_2 [112].

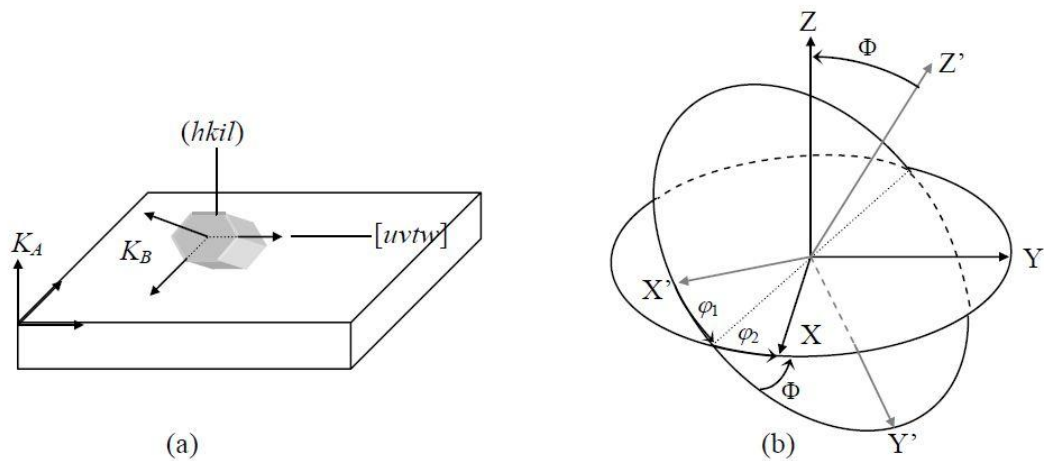


Figure 3.1.9. Two methods for representing the orientation g . (a) Miller indices (b) Euler angle [84].

The Euler angles are represented in three-dimensional Cartesian coordinate in the so called Euler space. Each point in the Euler space indicates an orientation g , that is to say, the entirety of all crystals in the Euler space is called as texture. Again, the texture is defined in general as the volume-distribution of certain crystals in the Euler space.

ODF can be represented in a reduced Euler space, when the crystal and sample symmetries are taken into account, as in orthorhombic sample symmetry of

sheets. The whole Euler space is ranged in $0^\circ \leq \varphi_1 \leq 360^\circ$, $0^\circ \leq \Phi \leq 180^\circ$ and $0^\circ \leq \varphi_2 \leq 360^\circ$, when the symmetry is not considered.

Figure 3.1.10. shows the general concept for pole figure that represents the probability of the distribution of crystals laid in an arbitrary sample direction. In case that the crystallites are randomly oriented, the poles are distributed uniformly in the projection, Figure 3.1.10 (a). Otherwise, assuming that the (0001) planes are oriented parallel to sample normal plane then the (0001) poles appear in center of the pole figure, Figure 3.1.10 (b). The pole density (or intensity) is presented in general as contour lines, as illustrated in Figure 3.1.10 (c).

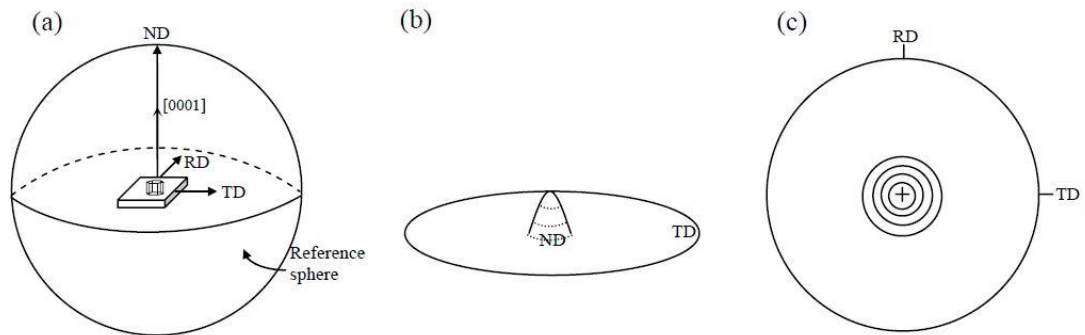


Figure 3.1.10. Schematics that illustrates the basic concepts of a pole figure [60].

For projecting the reference hemisphere (Figure 3.1.11 (a) and (b)) onto a projection plane, two common methods are employed: the stereographic projection and the equal area projection. In the stereographic projection a point on the surface of the reference sphere is connected to the South Pole, and the intersection of the connecting line to the plane tangent to the North Pole (that is

the projection plane) defines the point on the projection, Figure 3.1.11 (a). In this projection method, the distances and areas between the points are not preserved, however the angles are preserved. For this reason, this is also called the equal angular projection method. In the equal area projection, on the other hand, the point of the reference sphere is connected to the North Pole, and then the connecting line is rotated on the projection plane, as shown in Figure Figure 3.1.11 (b). The angles between the great circles are preserved in the stereographic projection, for this reason this is called also as the equal angular projection. On the other hand, in the equal area projection the circles of same diameter on the reference hemisphere convert into ovals of the same area.

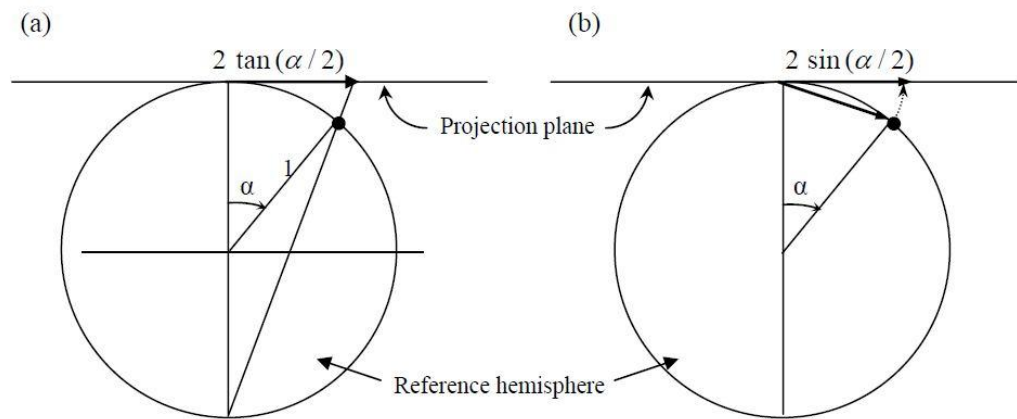


Figure 3.1.11. (a) Stereographic projection, (b) equal area projection [60].

For representing the texture of hexagonal materials the ODF has not been frequently used, but the texture is represented by measured (1010) and/or (0002) pole figures. It is attributed not only the fact that more measured pole figures are needed for the calculation, but also the fact that the qualitative texture analysis has brought sufficient results. It is fact that both pole figures support important information and fast insight for the simple extrusion or rolling texture. Due to

this fact, pole figures are employed extensively for texture evolutions in this study.

3.1.3.2 Pole figure measurement

Pole figures can be directly measured by some diffraction techniques, e.g. laboratory X-ray, neutron diffraction, synchrotron diffraction, SEM/TEM.

The most common technique for these measurements is the X-ray diffraction (back reflection technique), as employed in the current study.

The back scattered technique is proposed by Schulz [113]. The method involves hitting the specimen surface with an incident beam and measuring the intensity of the reflected beam to have a point on the pole figure. The sample is rotated about the normal direction and through the angle about the intersection of the reflecting plane and the sample plane to get reflections from more grains. A schematic of the method is given in Figure 3.1.12 [84].

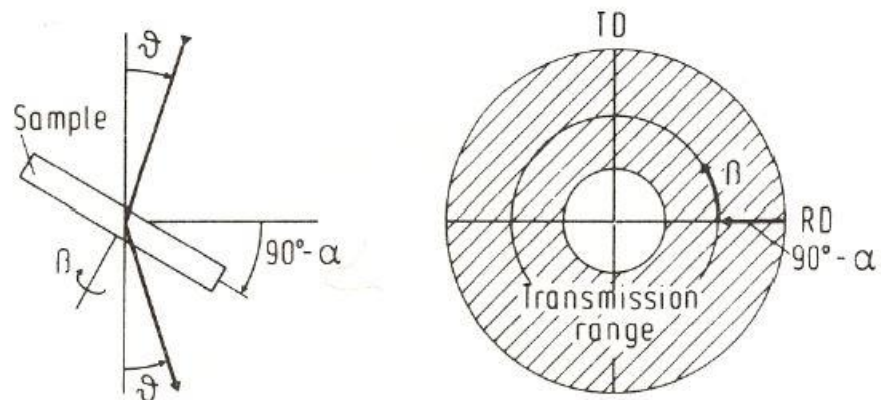


Figure 3.1.12. Back-reflection technique [64].

Since the incident beam hits the specimen surface in form of a cone of finite divergence, the tilting angle α becomes important due to its implications on effective cross-sectional area and broadening of the reflected beam. If the tilting angle α increases, the ideal round irradiated area becomes more and more elliptical. Thus, at too high tilting angles, the effective irradiated area may become larger than the sample size (Figure 3.1.13 (a)). Therefore, the reflection method loses its reliability as the tilting angle approaches 90° . The focusing conditions set up for the measurements are only true for the central line of the incidental cone and not for the border lines of the cone. The upper and lower parts of incident cone fall inside and outside the focusing sphere, which broadens the reflected beam. This gives rise to a loss of intensity Figure 3.1.13 (b)).

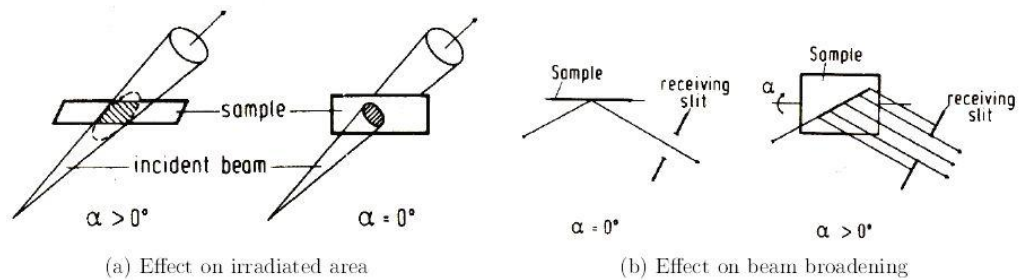


Figure 3.1.13. Effect of (a) tilting angle on effective irradiated specimen area and (b) broadening of the reflection beam [64].

Regarding these, one should remember that when the laboratory X-ray is used, the coverage of such measurements is often incomplete and the measured pole figures have non-normalized intensities. More importantly, the pole figures provide the orientation distribution in 2-dimension so that some of different

orientations appear on a same domain. The measured pole figures are generally called incomplete pole figures, because they do not cover the whole range of the pole figure or, more precisely, they do not cover the whole asymmetric unit of the pole figure. The incomplete pole figures are completed using various calculation methods by the software, popLA[114] in this study.

3.1.4 Applications of ECAE on Mg alloys

While these theoretical and computational works were being carried on, so many experimental studies were also performed. Wu and Baker [72] conducted experiments on ECAE using plexiglass tools and plasticine billets to examine how well the mentioned theoretical methods describe the local shear strain increase. They mentioned that the experimental findings are in good agreement with theoretical values. Furukawa et al. [115] examined the shearing characteristics associated with ECAE for different processing routes. They clarified the most appropriate processing route for the most rapid microstructural evolution. Their results lead also to the predictions concerning the dominant texture characteristics after pressing through different processing routes.

Shan et al. [38] employed gridding of the workpiece in order to observe the shear deformation during ECAE of Aluminum directly. They concluded that the shear deformation is relatively uniform except the top and end parts of the billet and they also verified the formation of a dead metal zone in the outer corner of the die. Semiatin and DeLo [72] also employed gridding and after an extensive work full of several data, they established the effect of the material properties on the tendency for shear localization in ECAE under cold working and hot working temperatures.

The effect of deformation speed is discussed in many studies especially on Aluminum, in addition to these aforementioned works. It has been shown that the equilibrium grain size does not change significantly with the pressing speed [2, 116]. However, higher speeds can induce temperature rises during deformation and thus processing at lower speeds would produce more equilibrated microstructures [2, 116].

These and most of the other works performed in this area also discuss the resultant microstructures and the evolution of them. They employ a wide range of imaging methods in order to characterize the microstructures and texture formations, as well as material characterization techniques. The studies considering the microstructural and textural changes are the majority in the ECAE research area.

Segal showed by the help of microstructural analysis that pure shear provides a long stage of continuous evolution and planar high angle boundaries [2]. Its characteristics are a short stage of continuous evolution, early localization, intensive straining along the shear bands and cross loading resulting in spatial networks of high angle boundaries and optimized processing.

Zisman et al. studied the method of equal channel angular drawing of sheet metals (ECADS) and presented the mechanical properties with the textural and microstructural findings [117]. They mentioned that they simply didn't observe the high angle boundaries in the deformation microstructures after 2 and 4 ECADS passes, and attributed this to the relatively high homologous temperature of Aluminum at room temperature. They advised further microstructural investigations for the estimation of the ECADS potential in producing high angle microstructures with sub-micron crystallites.

The usage of SPD as a tool for microstructural control is also discussed by Furukawa et al.[118]. They emphasized the factors influencing the development of homogeneous microstructures of equiaxed grains separated by high angle grain boundaries. It was concluded that the ultrafine grain sizes introduced by ECAE are stable at elevated temperatures in alloys where particles are present to inhibit grain growth. These materials exhibited high ductilities in tensile testing at rapid strain rates.

Jin et al. analyzed the microstructure evolution of AZ31 Mg alloy during ECAE [69]. 8 passes of ECAE were applied and it was observed that the grains of the alloy were significantly refined. The authors mentioned that the dislocations were induced at the initial stage of extrusion and they rearranged themselves to form dislocation boundaries and sub-grain boundaries during deformation. It was observed that as the strain increases, the newly created dislocations in the sub-grains were also absorbed by the sub-boundaries and the misorientation between sub-boundaries increased and evolved to low angle and high angle grain boundaries. They suggested that the grain refinement can be described as continuous dynamic recovery and recrystallization. Grain refinement mechanism is also analyzed by Zhao et al. in a study investigating ECAE of pure Aluminum [119]. They also described the process as a continuous dynamic recovery and recrystallization like Jin et al. The authors suggested that from the viewpoint of microstructure analysis, the grain refinement process is to control the dynamic balance of the dislocation generation and annihilation. From the viewpoint of the macro deformation analysis, the grain refinement process is to seek proper number of passes and the optimal processing routes.

The study carried out by Jin et al. [69] is one of the many studies on ECAE of Magnesium and its alloys. Yamashita et al.[52] applied ECAE to pure Mg and Mg-0.9% alloy at high temperatures like 200 °C and 400 °C, and they have

observed that the grain size is reduced under all conditions due to DRX and the process gave a significant improvement both in strength and ductility.

Biswas et.al.[120] presented the first study at which, pure Mg is ECAE processed at room temperature. They succeeded to products with grain sizes around 250 μm using route A, without any cracks. To do this, they aimed to minimize twinning and maximize the activity of non-basal slips, benefiting the stacking fault energy (SFE) differences between the modes. They concluded that a favorable initial orientation that corresponds to high Schmidt factor for basal slip and comparatively low Schmidt factor for the non-basal slips increases the workability of the metal. For the temperature effect, they showed that lowering the processing temperature slowly and decreasing the grain size increases the fraction of grain boundaries and triple junctions. Since these areas are favorable for activation of non-basal slip, the low temperature workability of the metal increases as well.

Considering the ECAE processing of several alloys with different crystal structures, Langdon, Figueiredo et.al is one very active group that is focused mainly on this subject. They discussed the effect of initial microstructure on microstructural evolution during ECAE at high temperatures, using both modeling and experimental results [121]. They also carried out innovative studies on the grain refinement mechanisms and texture evolution in ECAE processed metals [44, 118, 121-129] in addition to the studies mentioned above.

Beausir et.al.[21] studied the texture development of Mg during ECAE with a 90° die. They simulated processing with the routes A, B_C, and C upto four passes using polycrystal plasticity methods while presenting experimental results as well. The study concludes that there are very large lattice rotations during routes A and C, and this, when combined with the rotation field

characteristics of the process, explains the texture evolution. One interesting conclusion is that although the modeling process they used does not consider DRX which takes place during the processing, it gave very successful results. The authors explained this with a mechanism of DRX during which the newly formed grains are rotated around the c-axis, so they remain in the c-fibers in the study.

Recrystallization of high purity Aluminum during ECAE is studied by Skrotzki et al.[74]. Aluminum billet is subjected to three passes and the microstructure and texture are investigated by orientation imaging microscopy and electron backscatter diffraction. The resulting microstructure showed complete recrystallization after the first pass onwards. The study mentioned that the grain size decreased slightly with the increasing number of passes, and the corresponding texture consisted of an oblique cube component.

The DRX mechanisms of ZK60 alloy is also a popular subject of interest that requires more studies to be clearly understood. The concept is important since it results in uniform microstructures with an average grain size in the micrometer range [130-132]. The studies showed that the development of DRX in ZK60 strongly depends on the deformation temperature. Galiyev et al characterized the activation of DRX mechanisms in different temperature regimes [130]. According to their studies, at low temperatures ($T = 423 \text{ }^\circ\text{K}$), twinning plays an important role in the development of DRX grain structure, and twin-twin interactions result in high misorientation angles at grain boundaries. Besides, subsequent slip-twin interactions can result in the formation of high angle boundaries with intrinsic grain boundary dislocations. The new grains with highly non-equilibrium grain boundaries are characteristics of the low temperature DRX. At temperatures around $523 \text{ }^\circ\text{K}$, basal slip is the predominant deformation mechanism but cross-slipping takes place near original grain

boundaries. This results in extensive rearranging of dislocations and the formation of the subgrain structure, which, low angle boundaries are converted into high angle boundaries by small strain increases due to incorporation of cross-slipped dislocations. This evolution of subgrain misorientation increase is very typical for continuous DRX. At the third regime, $T = 623 \text{ }^\circ\text{K}$, the high temperature defines the deformation controlling step to be dislocation climb since the activation energy for plastic flow approaches the activation energy for volume self-diffusion. The microscopic strain localization at the slip lines causes the formation of grain boundary bulges, which provokes the nucleation of DRX grains.

In another study, Al-Samman and Gottstein discussed the DRX during high temperature deformation of AZ31 alloy to [133]. They applied compression to the samples at different temperatures and strain rates and observed the DRX behavior by texture predictions, SEM and EBSD analysis. They concluded that the steady state DRX grain size depended much more on deformation temperature and strain rate and suggested that there is a processing window where complete recrystallization and nearly random texture can be established; i.e. $T = 400 \text{ }^\circ\text{K}$, $\dot{\epsilon} = 10^{-4} \text{ s}^{-1}$, $\epsilon = -1.6$. The texture of the recrystallized twins was much weaker than the texture of parent grains and the mechanism of DRX in twins was found to be of continuous nature, involving the formation of low angle boundaries and their conversion to high angle boundaries; forming new, fine grains.

One important concept related to ECAE research, texture evolution during ECAE has led to many studies in the area. As mentioned earlier, Los Alamos National Laboratory, NM, USA is a pioneer institution with their valuable works. The team has a very important review paper on the subject [85], in which, ECAE texture measurements and calculations for the common crystal

structured materials is discussed in detail; not only analytically, but also experimentally. [96-104] Los Alamos National Laboratory team is also very well-known with the viscoplastic self-consistent (VPSC) model they developed for texture prediction. The model is extensively employed in the studies on modeling of texture evolution [98-100, 102, 103, 105-111].

Orlov et.al. [31] studied the texture evolution and the improvement of mechanical properties of ZK60 by integrated extrusion and ECAE. The work mostly compared the integrated ECAE technique with the conventional one, in terms of resulting microstructure, texture, and mechanical properties. They stated that the two-step integrated ECAE processed billets give much better mechanical results compared to single-step ECAE processed ones. This is attributed to the more extensive grain refinement in the proposed two-step procedure. Discussing the texture evolution in both cases, the conclusion reached is that the specimens processed by both methods exhibit a very similar strong (0002) basal texture.

Another important team working on the subject is Agnew et.al. Their works are not only on ZK60 processed in different conditions; but involve a lot of comparison with the other Mg alloys like AZ31, processed in same conditions. One of their publications is on the crystallographic texture in three different Mg alloys during ECAE [28]. That paper and the companion article [27] detailing the route A texture evolution offer a range of possible textures to explore, which may enhance different properties and applications, such as the enormous improvement in room temperature ductility documented for AZ alloys. They stated a very important conclusion, which will be supported with this current work. Considered broadly, ECAE processing of magnesium alloys tends to produce a certain class of textures regardless of the alloy or processing route. This class of textures is defined generally as <0001> fiber textures. However,

the orientation and strength of the $\langle 0001 \rangle$ fiber texture is strongly affected by alloying additions and processing histories. For example, the AZ alloys tend to develop textures with $\langle 0001 \rangle$ highly inclined (around 55°) to the extrusion axis, while the ZK alloy develops a primary fiber closer to 90° and along with secondary $\langle 0001 \rangle$ fiber(s), either normal to the flow plane or within the flow plane.

The companion article stated in this work [27], supports the findings with modeling studies and simulations, and affirms important conclusions. The authors mention that equal channel angular extrusion offers the potential to induce previously unobserved crystallographic textures, which may be of significant interest for modifying the properties. That study documents some of the variety of textures which are generated by Route A ECAE processing, for a number of magnesium alloys, with a range of initial textures and grain-sizes. For a given alloy, Route A processing appears to result in similar textures from one pass to the next. However, it is emphasized that the material undergoes large rigid-body rotations during the course of loading into the die and during the process itself, so it is not really the same orientations persisting, rather each pass through the die involves a texture evolution that results in a final texture very similar in appearance to the previous pass. Initial texture is shown to have a pronounced effect, particularly in dictating the presence or absence of certain texture components which arise due to their rotational stability.

The lower symmetry of the ECAE process as compared with conventional deformation processes reveals distinctions in the texture evolutions of the major classes of wrought magnesium alloys, despite the similarity of their conventional extrusion textures. In turn, these texture evolutions are used to extract information about the relative activities of the deformation mechanisms, which accommodate the plastic deformation, using an inverse approach. Alloys

AZ31 and AZ80 demonstrate basal slip dominated deformation with a small balanced contribution of the non-basal $\langle a \rangle$ and $\langle c+a \rangle$ slip modes. Alloys ZK60 and WE43 also show similarities with each other, and a significant contribution from the non-basal $\langle c+a \rangle$ slip mechanism (in addition to basal slip) appears to explain most of the observed texture components. Finally, the unique texture evolution of the Mg–Li solid solution exhibits a number of characteristics of simulated textures resulting from extensive activity of the prismatic $\langle a \rangle$ slip mode.

Considering the materials and methods they employed, Agnew's works will be referred frequently in this study while discussing the results.

3.2. Experimental Methods and Materials

3.2.1 Thermomechanical Processing of ZK60 Mg Alloy by ECAE

ECAE experiments are carried out at the Press Lab of Texas A&M University, College Station, TX, USA.

As mentioned, ECAE was invented in the former Soviet Union by Vladimir Segal in 1977, for which he obtained an Invention Certificate of the USSR, similar to a patent. Dr. V. Segal was a research associate in the ECAE Lab of Texas A&M University from 1992 to 1995 and built the present ECAE system, which is shown in Figure 3.2.1.

Previously provided die assemblies were often unsatisfactory for deformation processing of high strength, brittle materials due to excessive friction forces associated with movement of the material from one channel into a second channel. Temperature differences also often occurred between different portions

of the die assemblies and the material being extruded. Attempts have been made to overcome these limitations by using expensive, complex machinery to apply hydrostatic back pressure to brittle and low ductility materials during the extrusion process. The costs associated with such deformation processing equipment and methods have been very high and the results have been less than satisfactory [134].

Accordingly, an extrusion apparatus is provided including a die assembly with a first extrusion channel and a second extrusion channel formed at angles relative to each other for deformation processing of selected materials. The first extrusion channel includes two walls disposed opposite from each other and movable along the longitudinal axis of the first extrusion channel in the direction of extrusion. The moveable walls substantially reduce the negative effects of friction upon a billet or work piece as it moves through the first extrusion channel. A bottom plate assembly is provided within the die assembly to define a portion of the second extrusion channel which communicates with the first extrusion channel. The bottom plate assembly is used to both minimize friction during movement of the billet through the second extrusion channel and to apply a desired back pressure on the billet. The bottom plate assembly includes a first portion which is fixed relative to the die assembly and a second portion which may slide relative to the first portion during movement of the billet through the second extrusion channel [134].

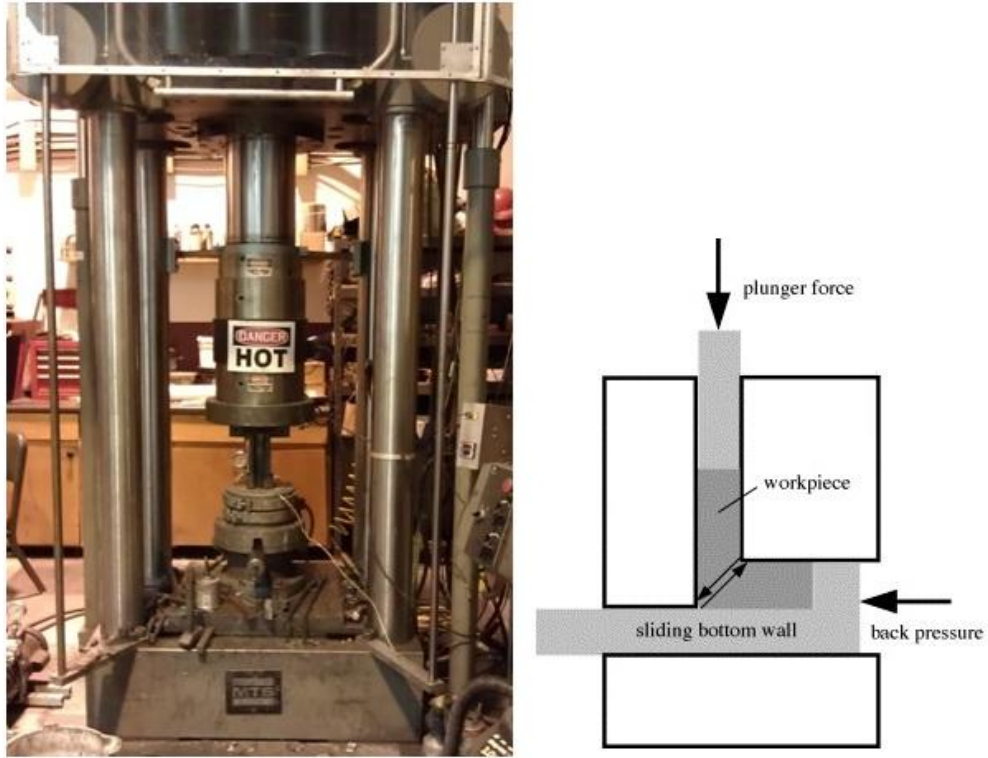


Figure 3. 2.1. The ECAE system at TAMU (Backpressure die).

The extrusions were carried out using a tool with a sharp 90° angle. The as-received ZK60 bars were coated with TEFLON films before extrusion. This was necessary to minimize tool wear, to conduct a smoother extrusion yielding uniformly deformed billets. Billets were of 25.4×25.4 mm cross section, with a length of 18 cm.

As mentioned before, Mg alloys need to be processed at elevated temperatures to avoid fracture [99]. However, the phenomenon of strain hardening of basal plane during plastic deformation, while prismatic and pyramidal planes would be recovering to get strain-softening, enables us to run ECAE on this alloy at lower temperatures in the later passes [120]. Accordingly, the first four passes were carried out at 200°C except one specimen. Extrusion rate was kept at

0.075 mm/s for all the passes except for the passes at 125 °C and below, which was reduced to 0.038 mm/s to suppress shear localization [12, 135]. These pressing speeds are kept this low studying the reports of Kang et al. [136], who observed uniform flow when AZ31 Mg alloy is pressed by 0.417 mm/sec at 200 °C; while segmented flow was observed at the same alloys when pressed at 0.17 mm/sec at 150 °C. The die was heated to the desired temperatures and the TEFLON coated bars are inserted to the die lubricated die. The billets were kept in the die at the extrusion temperature for 20 minutes before the first pass and 15 minutes before the subsequent passes. They were water quenched directly after each pass. The back pressure was increased from 7 MPa to approximately 100 MPa by increasing the number of passes on a single billet. Back pressure generates a compressive hydrostatic pressure to the sample and reduces the possibility of crack initiation and growth [137]. Since a lot of number of passes was applied and after each pass the billet needs to be machined, care was taken to preserve as much material as possible. Applying back pressure is necessary to increase the hydrostatic pressure and prevent cracking during processing. On the other hand, if back pressures higher than actually needed are applied, the billet will expand (fatten) and sometimes get stuck in the die. These ECAE parameters were found, after many trials, to be necessary to process the alloy without major shear localization or cracks due to the instability of deformation structure.

Regarding the billets processed at lower temperatures to benefit from the step-down effect, hybrid routes are also developed and employed during this study. Several trials are made to achieve the best final responses while exploring the literature data. The hybrid route formation strategy is simply shown in Figure 3.2.2.

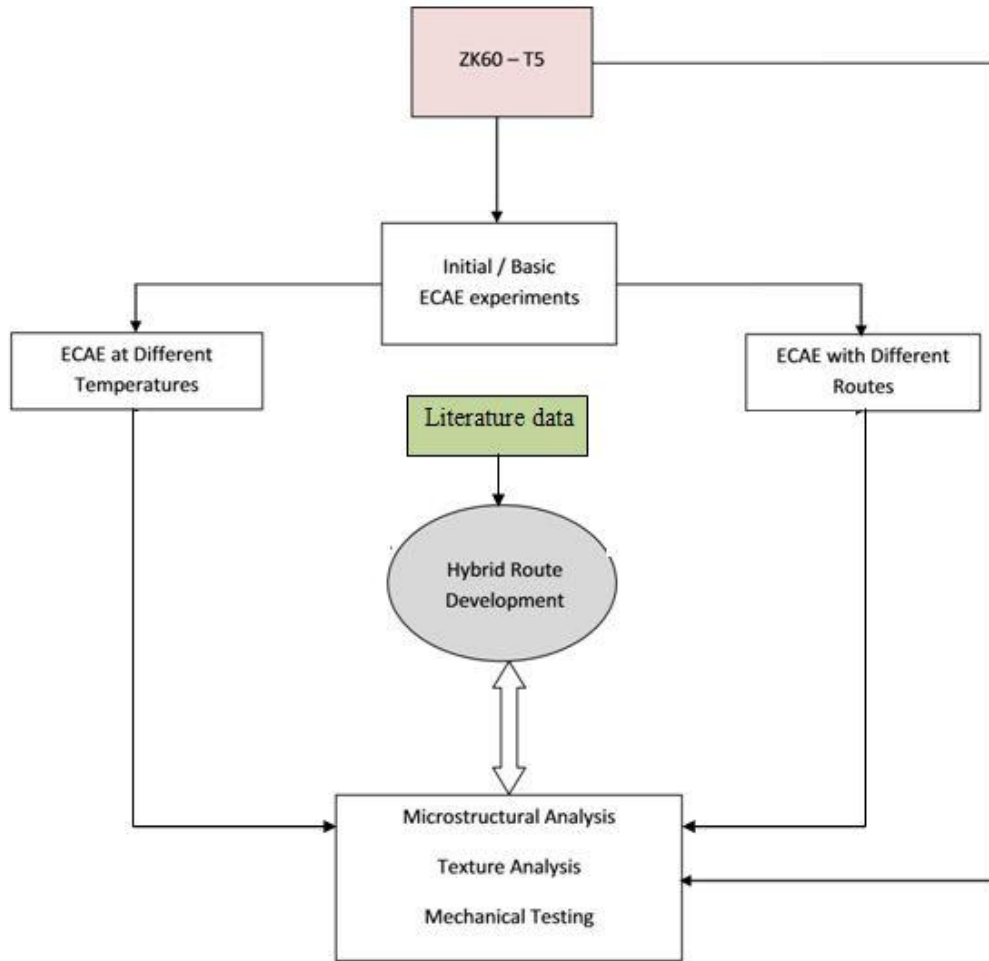


Figure 3.2.2. Hybrid route formation strategy.

Accordingly, the ECAE experiments carried out in this study are given in Table 3.2.1 with the accompanying processing conditions.

Table 3.2.1. ECAE experiments.

ZK60 ALL TESTS		
SAMPLE	PROCESS	Comments
S4	AR in T5 condition. Cast and hot rolled at 300C.	OK
S6	1A@RT	Failed SHEAR LOCALIZATION
S7	1A@100	Failed SHEAR LOCALIZATION
S10	4A@150	OK
S11	4A@200	OK
S12	2A@200	Failed SHEAR LOCALIZATION
S13	1A@200	Failed EXTREME MUSHROOMING
S20	4A@200 + 1C@150 + 1C@125	OK
S21	4A@200 + (1C@150+1A@150) + (1C@150+1A@150)	OK
S22	4B _c @150	OK
S23	2A@200 + (1C@150+1A@150) + 1C@125	OK
S27	4A@200 + (1C@150+1A@150)	OK
S28	4A@150 + (1C@150+1A@150)	OK

3.2.2 Analytical methods

3.2.2.1 Microstructural analysis

Optical microscopy and crystallographic texture measurements were performed on the samples cut from the fully deformed region of the billets from their flow planes. For optical microscopy, the samples were mechanically polished down to 0.1 μm and etched using a solution that is composed of 10 mL acetic acid, 4 gr picric acid, 20 ml H_2O and 50 ml ethanol. The optical micrographs were taken using a Keyence VHX-600K digital microscope.

The microstructural evolution of the alloy is also monitored by scanning electron microscopy (SEM). The samples were obtained by sectioning the processed billets parallel to their flow plane, and then prepared using standard metallographic techniques down to 0.25 μm diamond solution. The specimens were then etched with a solution that is a mixture of the same etchant used for optical microscopy. The SEM micrographs were taken using Cameca SX50 electron microscope.

3.2.2.2 Crystallographic texture analysis

Texture measurements were carried out using X-ray diffraction with a Bruker AXS D8 Discover Diffractometer (Figure 3.2.3) with $\text{Cu-K}\alpha$ radiation at 40 kV and 40 mA.

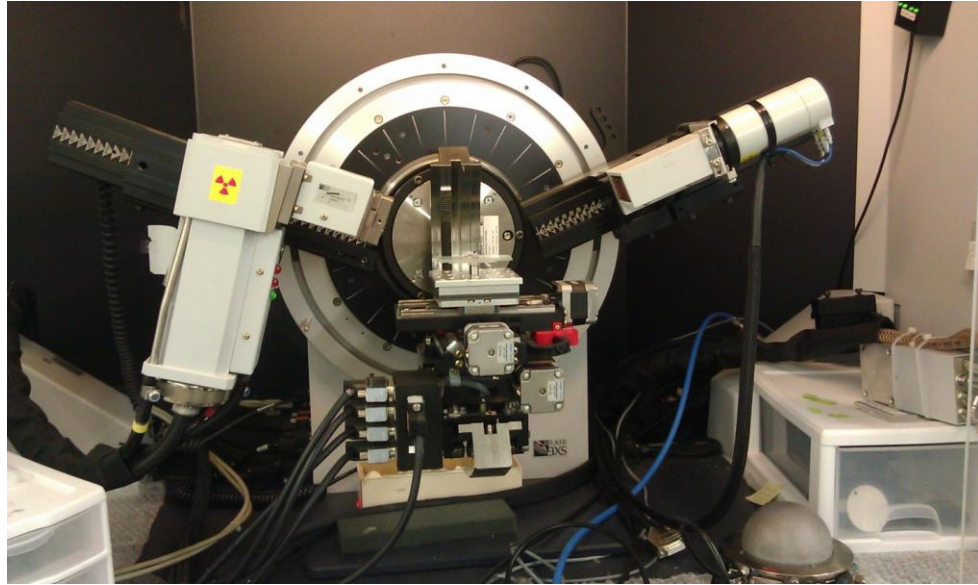


Figure 3. 2.3 Bruker AXS D8 Discover Diffractometer.

The data obtained from the diffraction is converted into actual pole figures by the software popLA (Preferred Orientation Package – Los Alamos) [114] (Figure 3.2.4).

```
popLA: preferred orientation package - Los Alamos          (Page 1)
U.F. Kocks, J.S. Kallend, H.R. Wenk (May 1999)

0. QUIT
1. Get specimen DIRECTORY and VIEW a file
2. MESSAGE data files: correct,rotate,tilt,symmetrize,smooth,compare
3. WIMV: make spec.SOD: calculate PFs and inverse PFs; make matrices
4. HARMONIC analysis: COMPLETE rim (.FUL), get Roe Coeff.file (.HCF)
5. CONVERSIONS, permutations, transformations, paring
6. DISPLAYS and plots
7. Derive PROPERTIES from .SOD or .HCF files, make WEIGHTS file for simul.
8. DOS (temporary: type EXIT to return)
Please type a number from 0 to 8 --> _
```

Figure 3.2.4 popLA opening screen.

3.2.2.3 Mechanical testing

Tensile and compressive test specimens were cut along three different directions; longitudinal, extrusion and the flow directions (Figure 3.2.5).

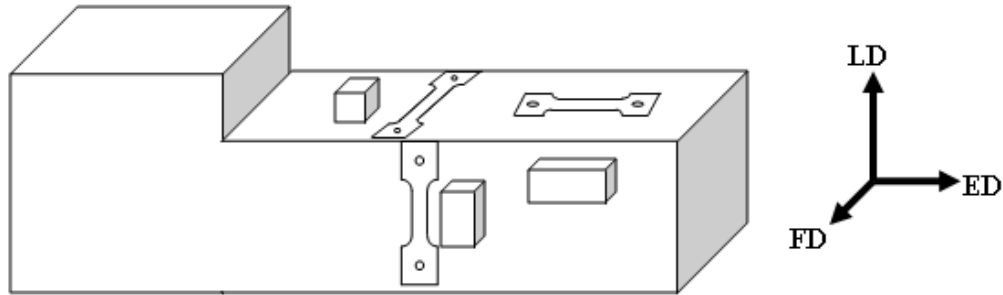


Figure 3.2.5 Position of the tension and compression test specimens.

The mechanical tests are done by displacement control during loading and force control during unloading. The tension test samples which had a dog-bone shape with a gage section of 1.5 mm x 3 mm x 8 mm were cut by wire electrical discharge machining (EDM) from the extruded billets (Figure 3.2.6). The tests are carried out by a MTS servo-hydraulic test frame controlled with a Teststar 3 system at a strain rate of $5 \times 10^{-4} \text{ s}^{-1}$. (Figure 3.2.7 (a)) The strains were measured using Epsilon 8 mm miniature extensometer. (Figure 3.2.8)



Figure 3.2.6. Wire EDM system.

For the compressive behavior exploration, the test samples are also obtained by wire EDM with dimensions of 4 mm x 4 mm x 8 mm, and tested with MTS Insight electromechanical desktop test frame (Figure 3.2.7 (b)). All the specimens were carefully cut from the areas which were uniformly strained, regarding the fact that the location of such volumes is a function of ECAE route [79].



(a)



(b)

Figure 3.2.7. (a) MTS Teststar 3 system (b) MTS Insight electromechanical desktop test frame.

The tensile and compressive behavior is presented as the average of at least three tests.

Microhardness test are also performed on as received and some of the deformed samples. The measurements were carried out at a load of 300 mN and presented in Vicker's hardness scale.

3.3. Experimental Results and Discussions

3.3.1 The as-received Material: S4

Initial microstructural analysis revealed that there is a bimodal grain size distribution, where grains elongated in the extrusion direction are accompanied with equiaxed ones. SEM studies are also performed on the specimen. The microstructural images on flow plane are given in Figure 3.3.1. The average equiaxed grain size is measured to be 3.45 μm with a standard deviation of 0.14 μm .

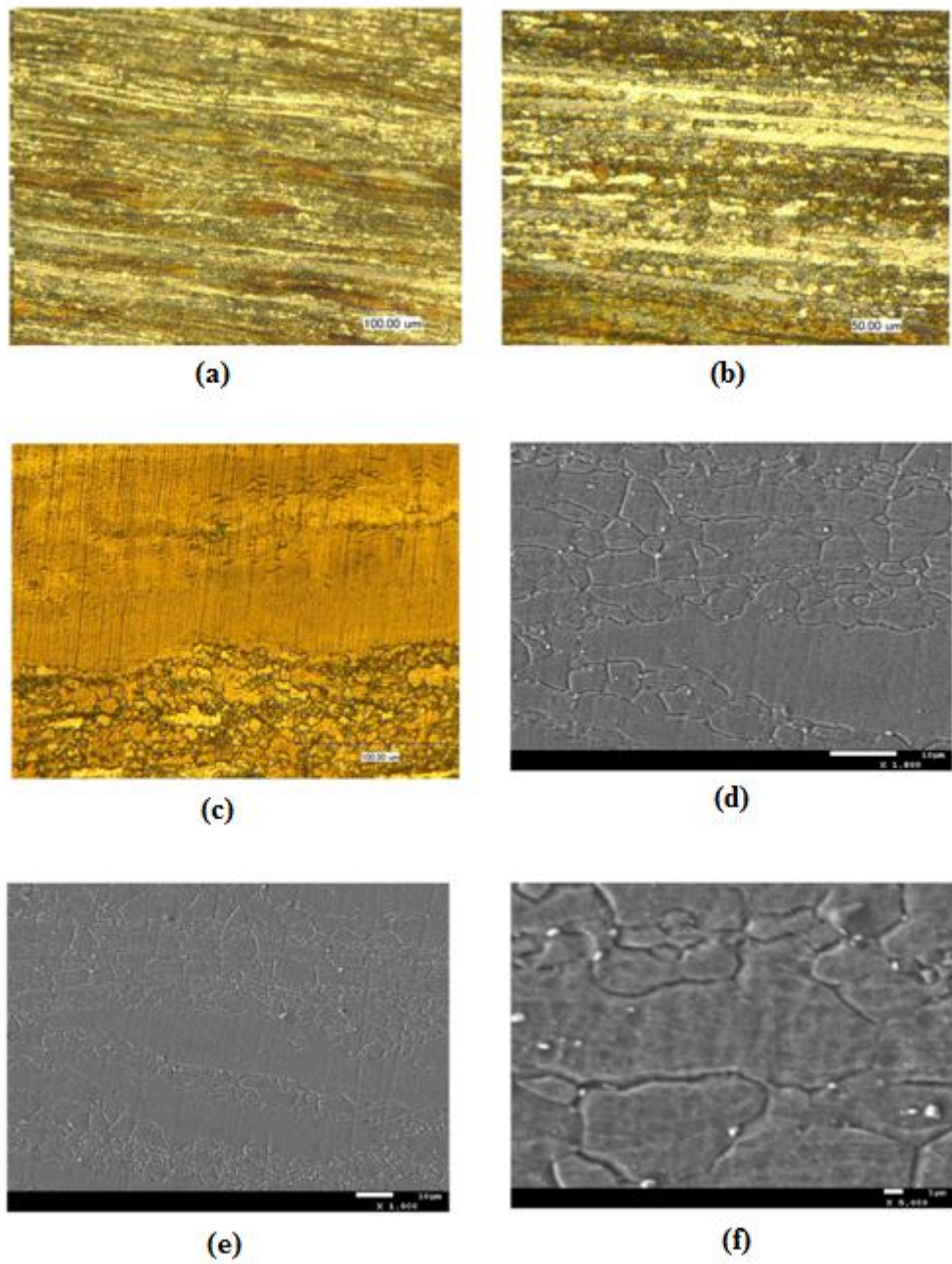


Figure 3.3.1. Optical microscopy images from flow plane of the as-received sample S4 with magnifications (a) X300 (b) X1000 (c) X1000 and SEM images from flow plane of the as-received sample S4 with magnifications (d) X1000 (e) X1000 (f) X5000.

Microstructure at extrusion plane is also studied by optical microscopy. The images are given in Figure 3.3.2.

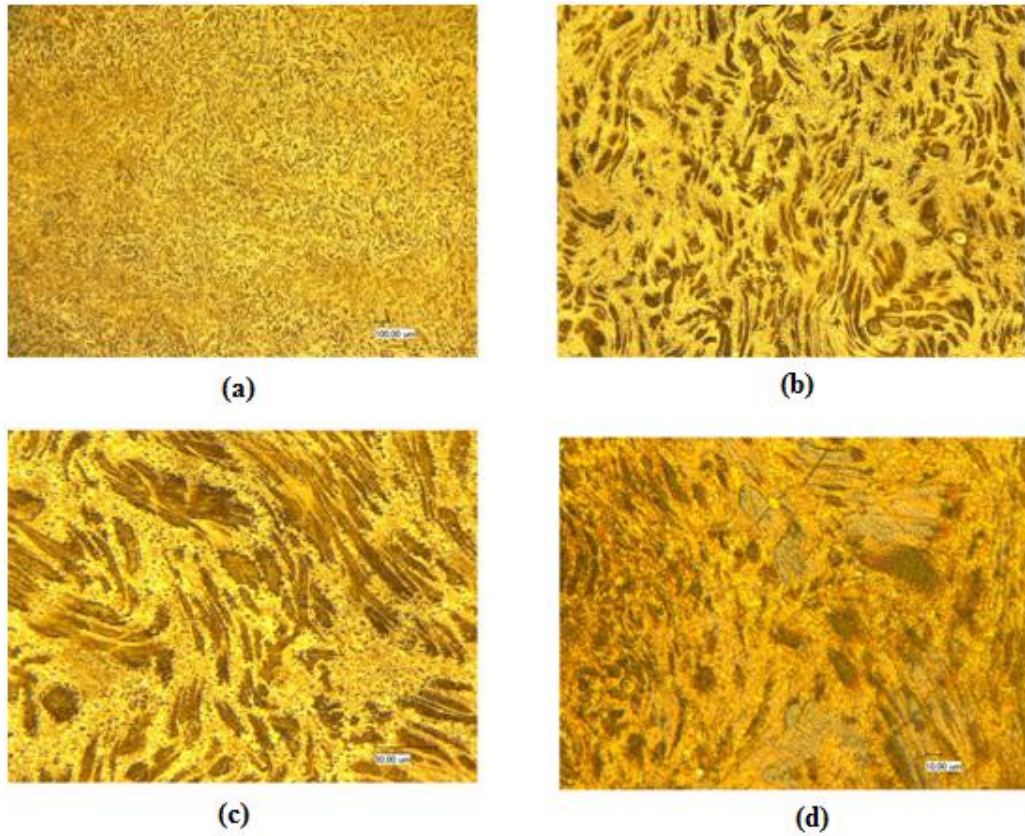


Figure 3. 3. 2. Optical microscopy images from extrusion plane of the as-received sample S4 of magnifications (a) X100 (b) X400 (c) X800 (d) X1000.

The extrusion plane microstructure is rather unusual at first sight, but remembering that this is an extruded alloy, it is quite typical. Shahzad and Wagner [32] studied the extrusion of ZK60 alloy and presented a similar microstructure, as shown in Figure 3.3.3.

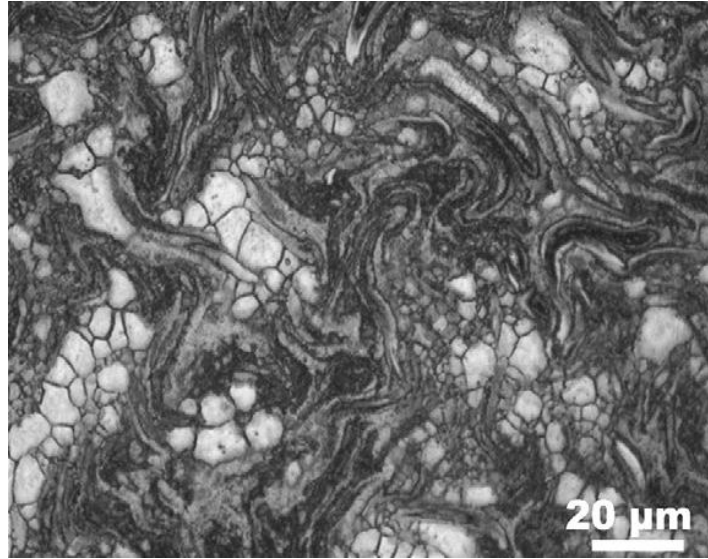


Figure 3.3.3. Cross-sectional view of the ZK60 alloys extruded at 300 °C and at ratio 44 [33].

Such “curling” behavior on extrusion planes is actually a phenomenon observed during axis-symmetric deformation [125]. In polycrystalline materials, uniform distribution of stress or strain is only within bounds and is not exact. There is plenty of room for conditions on mesoscopic scale to deviate from the bulk macroscopic conditions. This gives rise to intergranular or intragranular inhomogeneities where local plane strain conditions exist rather than macroscopic iso-strain condition. During deformation, these grains form ribbons and wrap around one another [125].

Figure 3.3.4 shows the measured basal and prismatic pole figure of as-received samples. The analysis showed that the as-received material exhibits a typical extrusion Magnesium texture [80, 138] where the basal poles are radially distributed perpendicular to the extrusion axis, forming a circular basal pole figure on extrusion plane, as seen in Figure 3.3.4 (a). The texture is also measured from the flow plane (Figure 3.3.4 (b)) and the upcoming discussions will be made on flow plane pole figures.

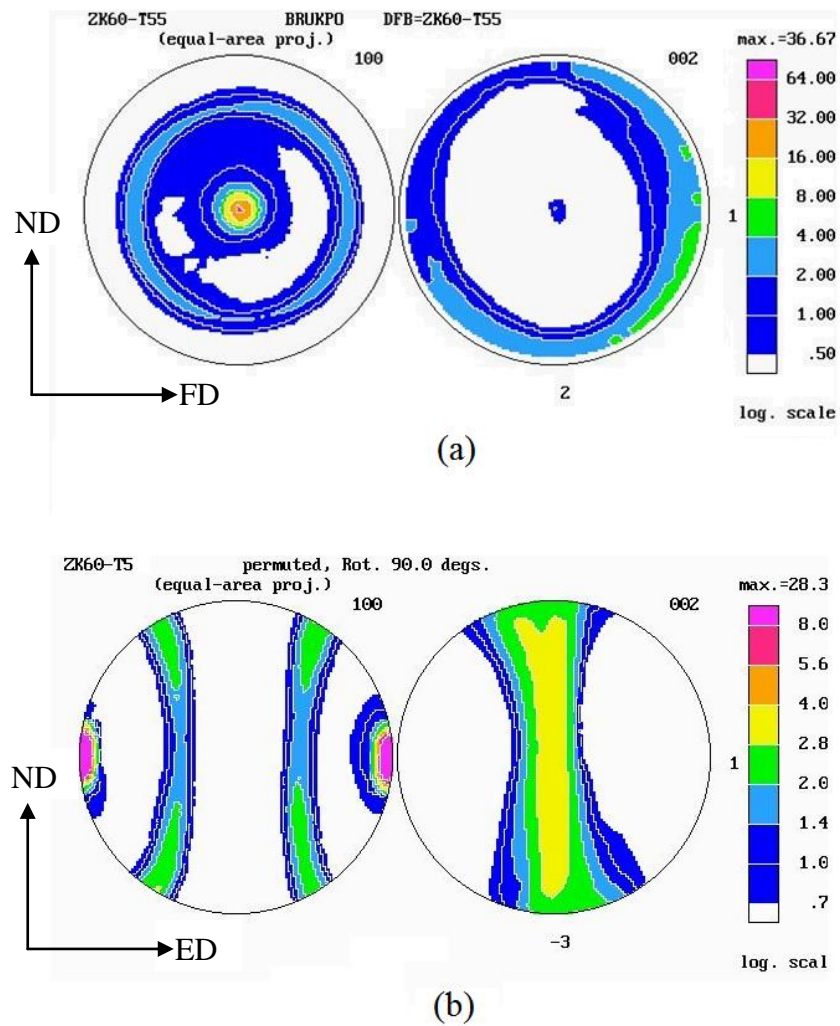


Figure 3.3.4. Prismatic and basal pole figures of S4 from (a) extrusion plane (b) flow plane.

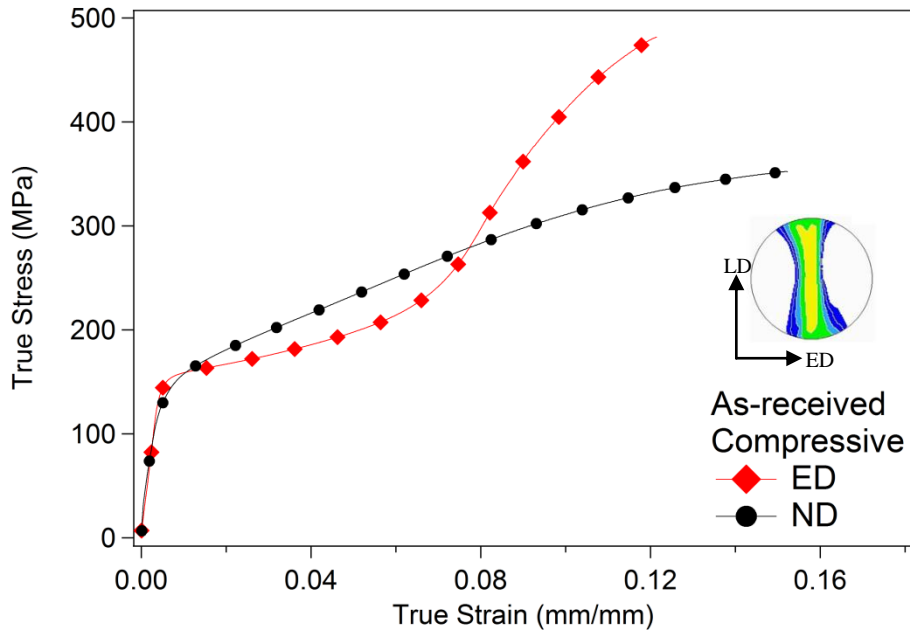
Mechanical response of the as-received material is determined by tension and compression tests. Conventional bar extrusion is an axis-symmetric process, and the directions that define the mechanical behavior are the extrusion direction, ED and the normal direction, ND. The tests are performed at room temperature, and the responses are given in Figure 3.3.5 (a) and (b). Under compression, the

material yielded at 143 MPa when tested through ED, and 165 MPa when tested through ND. Under tension, the yield stresses are 308 MPa through ED, and 143 MPa through ND. The mechanical properties of the as-received material are summarized in Table 3.3.1.

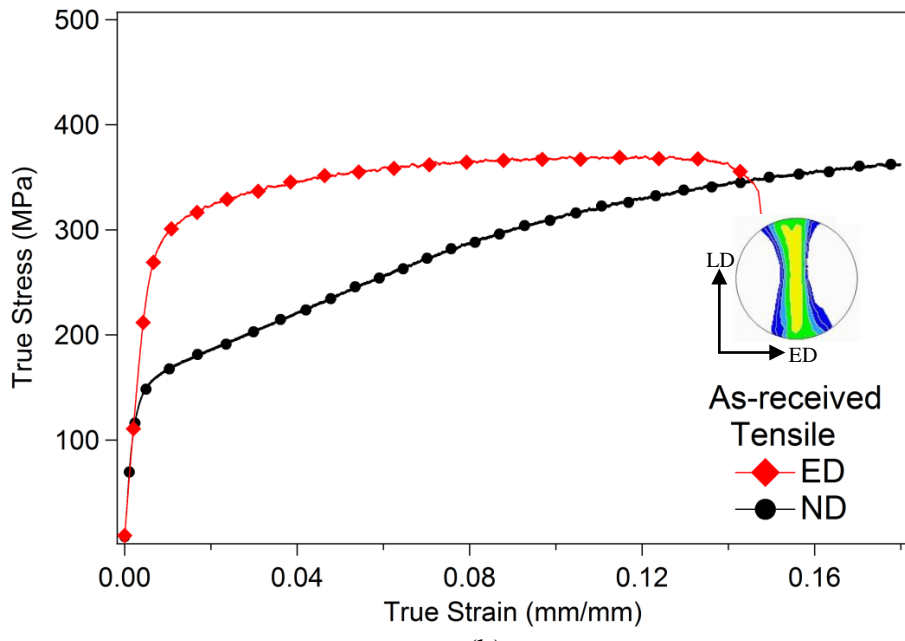
Table 3.3.1. Mechanical properties of S4.

	TENSION			COMPRESSION		
	σ_Y (MPa)	σ_{UTS} (MPa)	%strain (mm/mm)	σ_Y (MPa)	σ_{max} (MPa)	%strain (mm/mm)
ED	308 ±7	371 ±12	13.9 ±0.4	144 ±6	480 ±3	12 ±1.5
ND	144 ±4	370 ±8	19.8 ±0.5	166 ±12	351 ±7	14.9 ±0.2

The anisotropic mechanical response of the material under both loadings is noticeable. This anisotropy is due to the strong texture. The details of this argument will be given in the following chapters.



(a)



(b)

Figure 3.3.5. (a) Compressive (b) tensile response of the as-received material.

3.3.2. ECAE Processed Samples: Conventional Routes

The first part of the study focuses on the ECAE processing of ZK60 Mg alloy following conventional routes. The effect of applying only one pass of ECAE on ZK60 has been reported in literature, especially by Agnew et.al. [27, 28, 139]. The group conducted important studies on ZK60, carrying out detailed microstructural, textural and mechanical analysis on samples that are processed through conventional ECAE routes. They reported the properties for the samples processed through 1A, 2A, 4A and 8A; and 4B and 4C. These studies would form a strong reference for the verification of our initial findings. As mentioned before, this study aims to produce hybrid routes that would yield improved mechanical properties. Understanding the effect of processing route is very beneficial for selection of these hybrid routes.

3.3.2.1 Effect of Processing Route: S10 and S22

Processing route is the most important design and application parameter for ECAE processing of any material [33]. It is the main factor in the formation of the microstructure, texture and determination of the accompanying mechanical behavior.

In this study, two billets are processed upto four passes by ECAE, following routes in A and B_C. In route A, the sample is pressed without rotation in between the passes, whereas in route B_C the sample is rotated by 90° in the same sense (either clockwise or counter clockwise), as mentioned in Section I.1.2. The billet that underwent deformation following route 4A is named S10, and the one that is deformed through route B_C is S22. Both samples are processed at 150 °C. The investigation of these processed samples' microstructure and texture evolution, with the resulting mechanical properties form a reliable database for hybrid

route design. Such routes would enable the achievement of the desired properties in the material.

S10, processed through 4A@150, exhibited a bimodal grain distribution as in the as-received sample. The large elongated grains are embedded in a matrix of equiaxed grains that are refined due to the severe deformation. The average equiaxed grain size of S10 is 1.89 μm with a standard deviation of 0.09 μm . When compared to S4, this is a significant decrease in grain size. The elongated grains, however, are still present in the structure as mentioned before. Some of these grains underwent refinement, whereas most of them are curled and elongated throughout the specimen. This grain refinement has considerable effects on the mechanical behavior of the sample, when accompanied with the texture evolution.

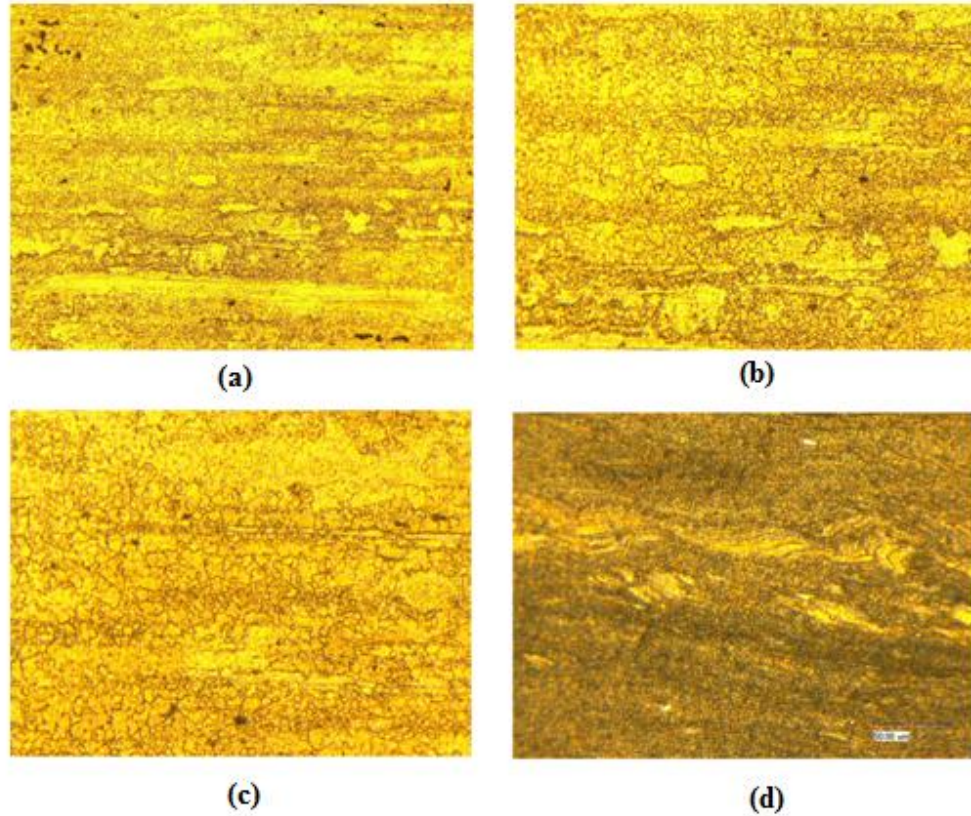


Figure 3.3. 6. S10 under optical microscope with magnifications of (a) X400 (b) X700 (c) X1000 (d) X1000.

The optical microscope images of S22, which is processed following the route 4B_C at 150 °C are given in Figure 3.3.7. The image shows that the elongated grains are almost all gone, and the structure is formed of equiaxed grains of size around 1.42 μm . The microstructural evolution in S22 is quite different than that of S10. The obvious reason is the difference in the deformation route.

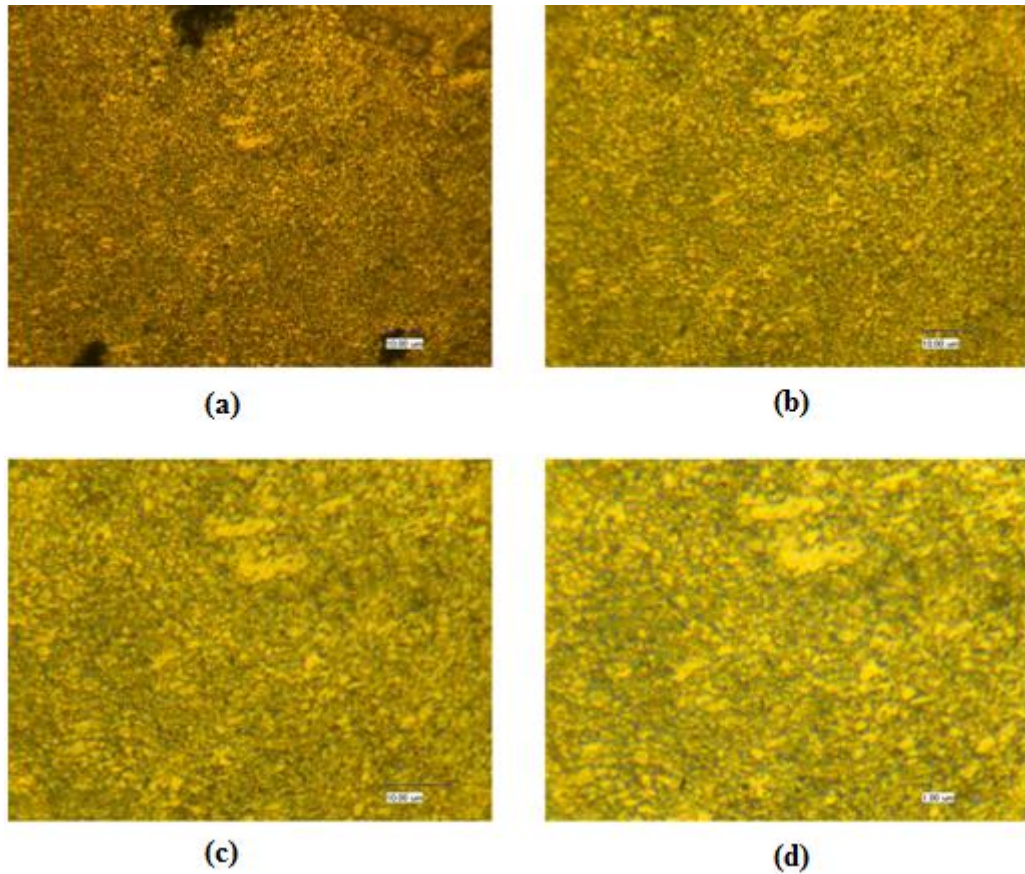


Figure 3. 3. 7. S22 under optical microscope microscope with magnifications of (a) X2000 (b) X3000 (c) X4000 (d) X5000.

This grain refinement and microstructural features would surely have considerable effects on the mechanical behavior of the samples, when accompanied with the texture evolution.

Considering that the starting texture is an extrusion texture anyway, the evolution in texture during route “A” processing would enhance the features of the basal pole figure.

The stability of the basal texture component parallel to FD after one pass of ECAE was interrogated in [140]. However, it was mentioned that further processing of the ZK60 samples in ECAE via route A gradually suppressed the basal preferential orientation. The resulting basal fiber is oriented almost parallel to the LD and slightly rotated counterclockwise around FD. This is not a simple stable texture feature, as found in a monotonic-straining process, because the ECAE deformation enforces a rigid-body rotation. Thus, during each pass, the grains rotate in a consistent way, generating a similar texture at the end of the processing step.

The study presented the pole figures of the ZK60 deformed in ECAE using different routes (A, B_c, and C), 4 passes. These pole figures are given in Figure 3.3.8.

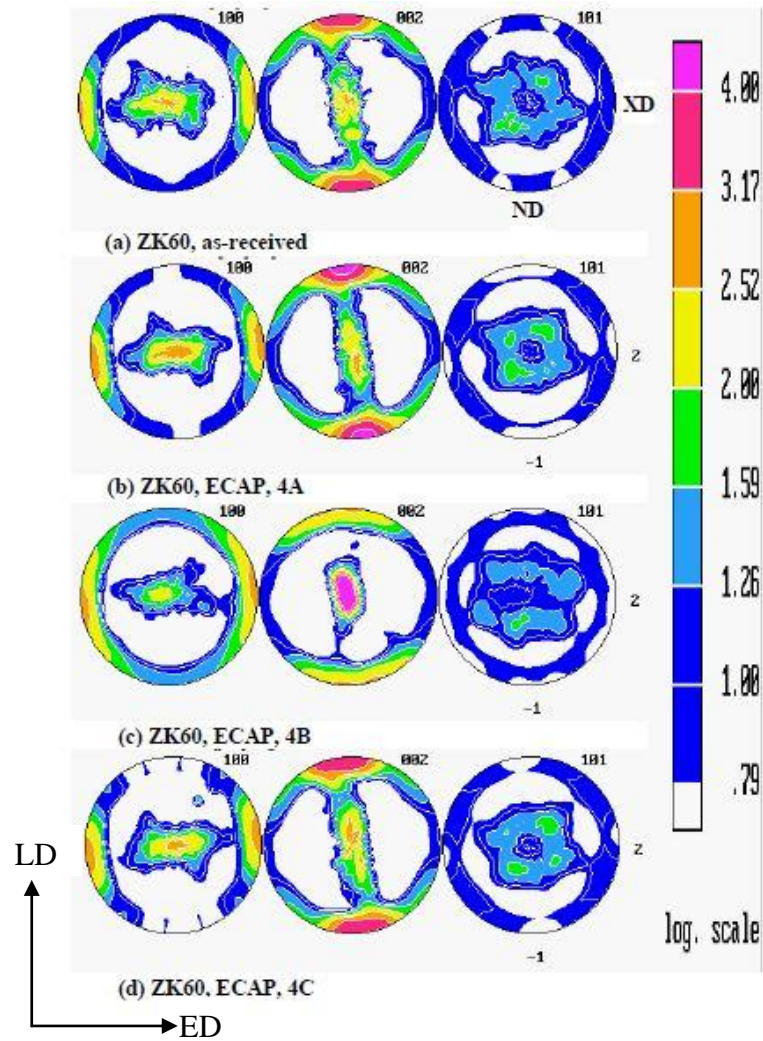


Figure 3.3.8. Pole figures of the ZK60 deformed in ECAE using different routes, 4 passes [109].

According to the figure, although the routes A and C give similar results, the route B demonstrates a different behavior. An intense basal fiber, oriented parallel to FD can be seen in Figure 3.3.8 (c) for the route 4B_C. As the billet is rotated 90° around its ED axis, before each pass, it is possible to consider this texture component as remnant from the previous step. The authors have mentioned that the degree of redundancy in the case of the route B_C (a consecutive rotation of 90° between the passes) is the leading factor for this

behavior. Thus, the two basal fibers seem to persist along a B processing path of ZK60, at least for relatively small number of passes.

The prismatic and basal pole figures of the S10 and S22 samples are measured and presented in Figure 3.3.9 with the reference sample S4.

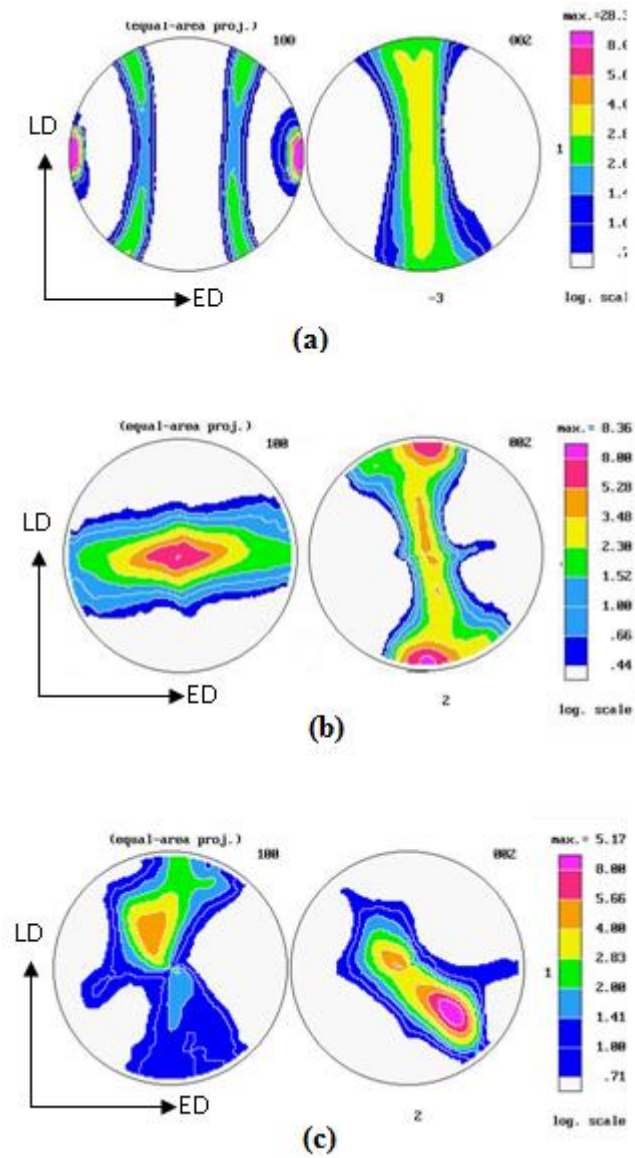


Figure 3. 3. 9. Prismatic and basal poles figures of (a) S4, (b) S11 and (c) S22.

Samples which were deformed following Route A tend to strengthen the basal texture components parallel to LD, which, then would result in activation of prismatic slip and twinning while loading under certain directions [12, 24, 141]. Tensile loading parallel to the c-axis (basal poles) of most Mg alloys are expected to result in tensile twinning [142]. The proof of this behavior can be observed at the mechanical test data. A plateau region with almost steady stress level and no hardening, followed by an upward curvature with a high hardening rate is the indication of the activation of twinning in HCP materials [24, 134]. Twinning and non-basal slip mechanisms have considerably low Schmidt factors and higher CRSS values, and this results in delayed yielding and high yield and ultimate tensile strengths. Since the basal poles are lying on LD, tension along LD results in expansion along this direction and tensile twinning is the active mode of deformation, as observed in the Figure 3.3.9. A similar tensile twinning behavior is observed when the processed samples are compressed along ED and FD, since the loading direction is perpendicular to the c-axis of the crystallites in these cases.

Studying the texture evolution of Route B_C processed samples, it can easily be observed that the distinct texture components along LD are softened and the basal peak orientations become more spread along the orthogonal directions. This is expected since the billet is rotated along its extrusion axis in between each pass. This rotation hinders the trend of the crystals to orient themselves along a certain direction. As it can be observed from the mechanical responses, the more the texture is spread, the less the flow stress anisotropy and T/C asymmetry are observed. At this point, it must be remembered that twinning is actually unidirectional and it only activates in a certain direction and is the main factor that leads to T/C asymmetry. Accordingly, when compared to strongly basal textured materials, that property is expected to be less pronounced.

Another conventional case that was not studied in this current work, Route C processing, results in the formation of basal peaks at a certain angle with LD in addition to the existing basal peaks that are parallel to LD in the pole figures [24, 95, 99, 134]. These crystals that are oriented with a certain angle to LD would activate basal slip to a certain extent, whose basal peak is ideally at 45° with the loading direction. Basal slip is the easiest deformation mode that would take place during the deformation of all HCP materials including ZK60, and thus, such textured materials tend to yield at very low stress levels. However, this disadvantage can be put up with due to the significant increase in ductility that comes with the ease of slip.

For a billet with a starting texture of that of extrusion, processing in Route A and Route C results in increased yield and ultimate tensile strengths under certain directions; whereas $4B_C$ results in a more homogeneous microstructure as shown in Figure 3.3.9. Besides, the strengths obtained by the tension and compression testing are not promising. Accordingly, Routes A and C are better candidates to conduct more processing on them, since improving the mechanical properties of the ZK60 alloy by ECAE is our primary aim.

Since the routes A and C are the only ones employed in this study, the resulting texture after deformation is expected to be A, or its combination with C. These are schematically shown in Figure 3.3.10.

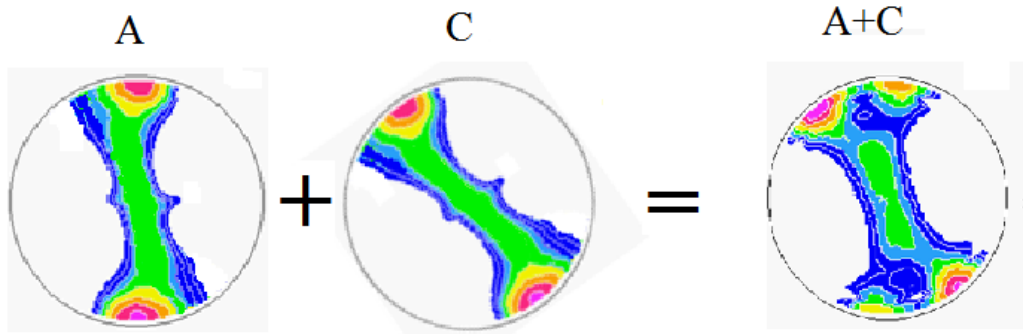


Figure 3.3.10. Expected textures in the study.

The effect of the processing route is very significant on the mechanical response as well. Combined with the microstructure, the formed textures associated with the routes determine the mechanical properties. The tension and compression tests are performed on both cases under three orthogonal directions. The results of the compression tests are given in Figure 3.3.11 (a) and (b) for S10 and S22, respectively. Based on the above arguments, the mechanical response can be explained truly.

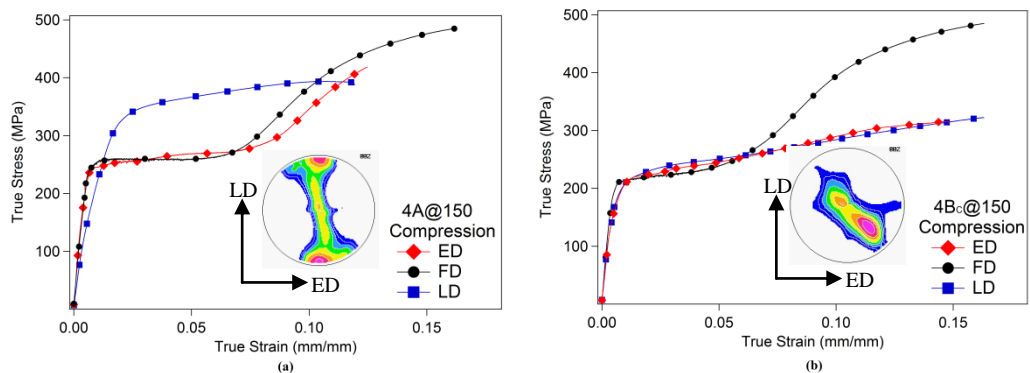


Figure 3.3.11. Compressive response of (a) S10 and (b) S22.

The mechanical properties of the specimens are summarized in the following Tables 3.3.2 and 3.3.3.

Table 3.3.2. Mechanical properties of S10.

		TENSION			COMPRESSION		
		σ_Y (MPa)	σ_{UTS} (MPa)	%strain (mm/mm)	σ_Y (MPa)	σ_{max} (MPa)	%strain (mm/mm)
S10	ED	345 ±5	396 ±12	10.5 ±0.2	239 ±11	484 ±8	16 ±0.6
	FD	373 ±11	382 ±14	14.9 ±0.4	236 ±7	417 ±4	12.4 ±0.3
	LD	247 ±6	364 ±7	15.7 ±0.4	312 ±6	394 ±9	11 ±0.2

Table 3.3.3. Mechanical properties of S22.

		TENSION			COMPRESSION		
		σ_Y (MPa)	σ_{UTS} (MPa)	%strain (mm/mm)	σ_Y (MPa)	σ_{max} (MPa)	%strain (mm/mm)
S22	ED	156 ±3	290 ±10	14.7 ±0.4	212 ±4	485 ±6	16.3 ±0.3
	FD	294 ±4	380 ±8	18.7 ±0.8	210 ±6	316 ±3	14.7 ±1.5
	LD	231 ±7	320 ±8	14.5 ±0.2	215 ±7	323 ±6	16.1 ±1.1

The most striking feature that catches one's eyes is the difference in the compressive behaviors along LD in both cases. S22, which is processed through 4B_C route, underwent 90° rotation between each pass, which results in the formation of a more homogeneous microstructure, as discussed above. Accordingly, it is expectable to observe similar behavior along different directions. In other words, the flow strength anisotropy shall be reduced by homogenizing the microstructure. This homogenization is also visible in the pole figure, since the basal poles are spread much more widely throughout the figure. When loaded under compression through LD, the flow plane's in-plane directions; i.e. ED and LD behave similarly since the basal poles are oriented

similarly for these directions, at around 45° away from each. This results in the activation of basal slip first, causing the lower yield strength for both directions. T/C asymmetry is also insignificant in this case due to the same reasons. When tested under compression, the twinning along FD is observed, naturally, since the loading direction is perpendicular to FD and this results in the activation of tensile twinning. The plateau region is followed by rapid hardening; the very characteristic of tensile twinning.

For S10, however, this is not the case. Due to the strong basal pole orientation along LD, the mechanical response when loaded in this direction is completely different than those of the other two directions. When compressed along ED and FD, the tensile twinning is activated in the material. It can be argued that basal slip is also activated to a certain extent, since the plateau region is not straight, but also a little hardening is noticed. The plateau is followed by rapid hardening, as usual, until the material fails. The compression along LD cannot activate basal slip as the basal pole orientation is not appropriate. Since compressive twinning is not favored in Mg and its alloys, the material does not yield until the CRSS of the non-basal slip is reached. The CRSS of pyramidal slip is still much higher than prismatic slip, as mentioned before [143]. After yielding, material hardens with non-basal slip and fails.

The investigation of the tensile test results of the specimens also yielded important findings. Figure 3.3.12 gives the tensile behaviors of the specimens deformed by both cases along the orthogonal directions.

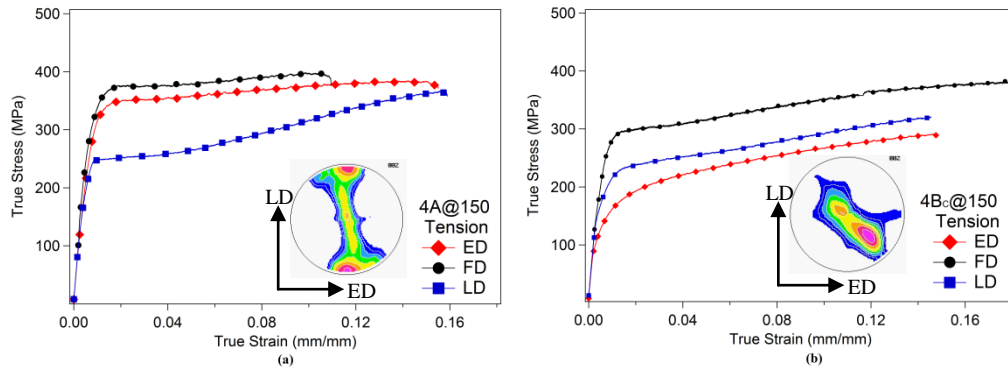


Figure 3.3.12. Tensile response of (a) S10 and (b) S22.

For both cases, the highest yield strength levels are achieved along FD under tensile loading. For S10, the material simply hardens by basal and prismatic slip after yielding. For S22, however, the specimen showed a plateau region followed by rapid hardening; the characteristic of tensile twinning. This behavior can be explained by the strong basal fiber along FD for S22. Accordingly, when pulled along FD, the sample will exhibit tensile twinning and the characteristics of it; the yield strength elongation followed by hardening. The basal pole figure of S22 does not have any strong components along ED and LD, thus deformation by basal and prismatic slip is expected and observed in those cases. S22 undergoing slip when tested along LD, created a difference between it and S10. S10 has a strong basal fiber lying along LD and accordingly, it will undergo twinning when loaded under tension along that direction. The characteristic nature of twinning is observed in that case. Both of the specimens that are tested along ED exhibited hardening by slip since neither of the two case's basal poles lie parallel to pulling direction.

3.3.2.2 Effect of Processing Temperature: S11 and S10

Processing temperature is a quite important parameter in ECAE procedure, especially if the material to be processed has low workability or is prone to DRX. Due to their HCP structure and the limited ductility associated with it, Mg alloys are usually processed at high temperatures. Since they have relatively low melting temperature, the homologous temperature is relatively high for these alloys; therefore, dynamic recovery and recrystallization take place during processing. DRX will affect the mechanical properties since it produces new unstrained grains that are dislocation free.

Because of the high critical resolved shear stresses required for the activation of non-basal slip systems, dynamic recrystallization plays an important role in the high temperature deformation of magnesium [144].

The DRX grain size increases with the increase in deformation temperature and decrease in strain rate, i.e. with the decrease in Zener-Hollomon parameter Z , given in the following equation:

$$Z = \dot{\epsilon} \exp(Q / RT) \quad (3.3.1)$$

Where Q is the activation energy and R is the gas constant.

As mentioned before, the deformation of Mg and its alloys by slip is accommodated mainly by the glide of $\langle a \rangle$ dislocations on (0001) basal and (10-10) prismatic planes and $\langle c+a \rangle$ dislocations on (112-2) pyramidal planes. According to some reports on Mg single crystals, the CRSS of a non-basal system on prismatic and pyramidal planes is approximately 100 times of the

CRSS of a basal slip system at room temperature [18, 145, 146]. Therefore, plastic deformation in polycrystalline alloys has been thought to occur almost entirely by basal slip. However, increases in processing temperature would change the ease of deformation by effecting CRSS of a non-basal system on prismatic and pyramidal planes. This effect is studied widely and yielded important conclusions. Yoo explains the activation of the additional non-basal slip systems and thus increased workability by increasing temperature [14, 82]. Agnew et al. reported $\langle c+a \rangle$ slip being responsible for improved workability at elevated temperature as well and adds that DRX improves ductility. [92]. The relationship between DRX and $\langle c+a \rangle$ slip and DRX behavior at the temperatures between 150°C and 350°C for ZK60 under compression is studied by Galiyev et.al. [130-132]. Their published work states that DRX is important in activation of $\langle c+a \rangle$ slip and it is also associated with basal slip and $\langle c+a \rangle$ pyramidal slip as the operating mechanisms, while the operation of $\langle c+a \rangle$ slip promotes the formation of HAGB at 200°C. Gottstein et.al. reported similar findings, stating when the processing temperature is larger than 200 °C; DRX takes place besides thermal activation of $\langle c+a \rangle$ slip [147]. One very important conclusion of this study is that texture becomes less pronounced when processed at high temperatures. Al-Samman and Gottstein, found that DRX grain size is very strain rate sensitive at high temperature (400 °C) [148]. No significant change of the texture was observed by changing the strain rate at low temperature (200 °C). However, at 400° C, different strain rates lead to a conspicuously different texture evolution. When specimen tested in compression along direction parallel to basal planes (basal slips are suppressed because of zero Schmid factor) and at high temperature (400 °C), deformation was accommodated by prismatic and pyramidal $\langle c+a \rangle$ slip. Although this initial orientation could promote (10-12) twinning, the low strain rate 10^{-4} and high deformation temperature render twinning less important for deformation. The

texture lost its sharpness with amount of strain; therefore, authors concluded that the texture randomization cannot be attributed to slip activity but rather to DRX. Another point is emphasized by Tan and Tan, who stated that low temperature DRX (DRX at 200 °C) occurs in magnesium due to the lack of easily activated slip systems at low temperature [149]. They mention that the low stacking fault energy of magnesium and high grain boundary diffusivity also promote LTDRX.

DRX is effective in high temperature ECAE deformation in two ways. First, it leads to the formation of new strain free grains. This is not a desired situation for the cases where strength enhancement is aimed since it would be a disadvantage in achieving high yield strengths. However, the formation of these new grains results in a more uniform microstructure and may even break down the possible elongated grains that are formed during extrusion process. The possible strain softening due to DRX is always in competition with the hardening associated with dislocation accumulation, twin formation (Hall-Petch effect) and texture changes.

Agnew et al. [28] and Beausir et al. [150] have separately shown that it is possible to perform ECAE of Mg alloys at higher temperatures (around 250 °C) due to the increased activities of non basal slip systems at these temperatures. Kang et al. [136] carried out ECAE of AZ31 alloy below 200 °C, however they had fractures at their billets through strain localization, although they have employed very low deformation speed. Ding et al. [77] reported stepping down to 115 °C at the 12th pass of hybrid route. However, the possibility of lowering the ECAE temperature without fracture remained unexplored until the work of Biswas et.al.[120] was published. Biswas et al. presented the first study at which, pure Mg is ECAE processed at room temperature at the 8th pass of Route A.

As observed, the literature considers 200 °C a “low temperature” for the ECAE processing of Mg and its alloys. This study aimed for processing at lower temperatures and benefit from the low temperature grain refinement effects for the increase in mechanical properties.

The deformed microstructure of S11 is given in Figure 3.3.13. In S11, the grains are nearly equiaxed with grain size of 1.99 μm , with a standard deviation of 0.08 μm after processing. However, the grain size structure still exhibit a bimodal distribution, which consisted of coarse grains of several microns embedded in relatively large amount of fine grains. This structure is due to the inhomogeneous structure of the starting material.

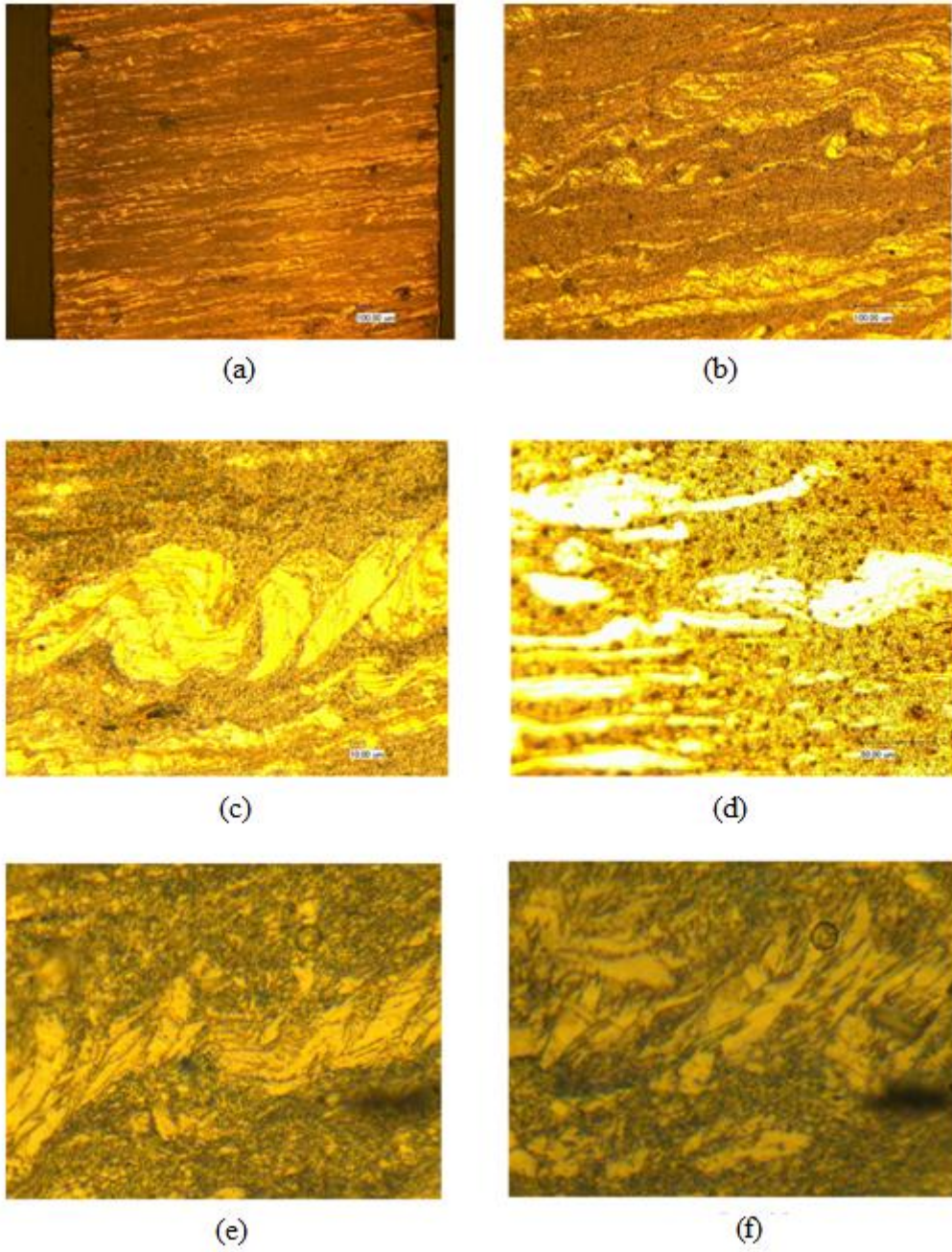


Figure 3.3.13. S11 under optical microscope with magnifications of (a) X100 (b) X500 (c) X1000 (d) X1000 (e) X3000 (f) X5000.

One striking feature about these images is that elongated grains observed in the as-received structure are not refined, and are not straight anymore as in Figure 3.4.2 (d) and (e); but instead are deformed through a pattern, almost curled. This microstructural evolution is also verified with SEM analysis (Figure 3.3.14).

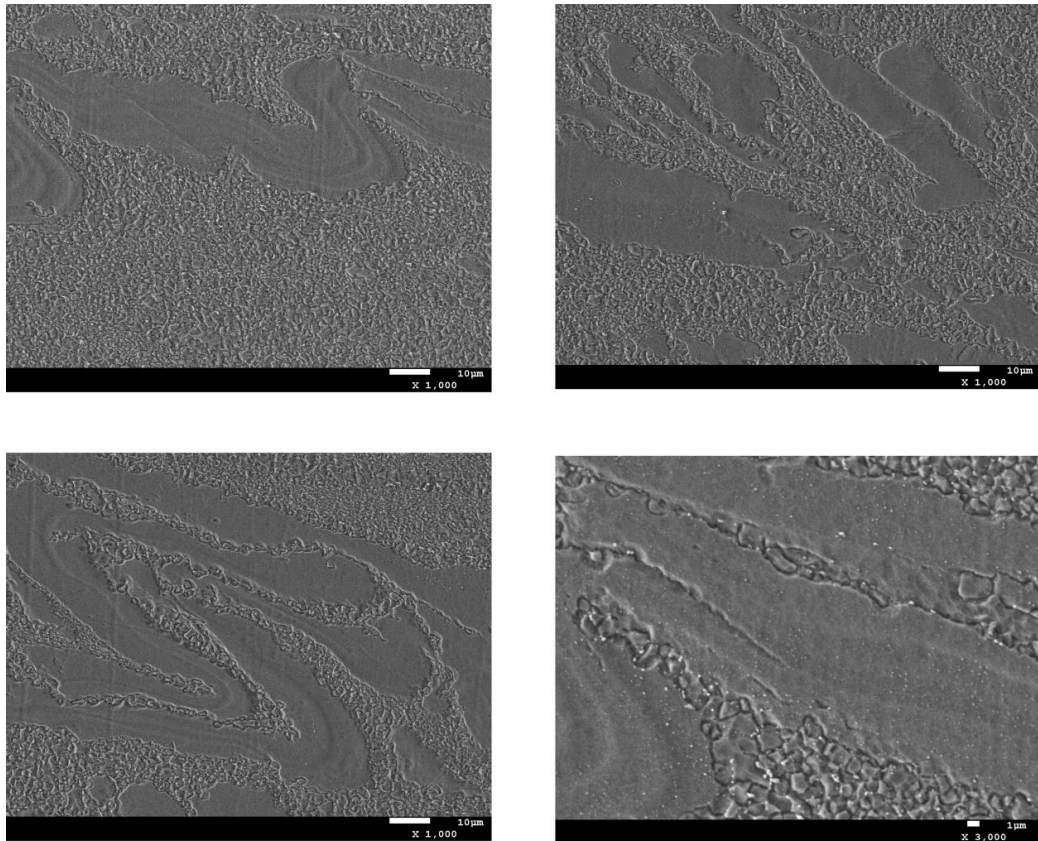


Figure 3.3.14. Microstructural analysis on S11 (SEM images).

The situation is quite similar in S10, where bimodal distribution is observed with coarse grains are embedded in fine equiaxed grains as seen in Figure 3.3.13. The average size of the equiaxed grains is 1.89 μm with a standard deviation of 0.8 μm, slightly different than that of S11.

The same “curling” behavior is also observed for S10 at some regions (Figure 3.4.10). However, there are also regions where these curled large grains underwent fracture; or more truly, refinement; as shown in Figure 3.3.9. This so-called “refinement” was not observed in S11. Regarding this, it can be deduced that the lower temperature processing helped the grain refinement, and was able to refine the elongated grains to some extent.

The aforementioned studies would form a strong reference for the verification of our initial findings. However, it should be noted that almost all of them performed the ECAE processes above 200 °C, which would not benefit from the strengthening by grain size reduction effect, since this temperature is comparatively high. As mentioned before, this study aims to go to lower ECAE processing temperature values to overcome this effect.

The processing temperature also plays an important role in texture evolution during deformation. Agnew [27, 28] reported the pole figures they obtained for 4A processed sample at 260 °C. Comparing their data with our findings (Figure 3.3.15), it can easily be observed that the aforementioned statement is in good agreement with the results.

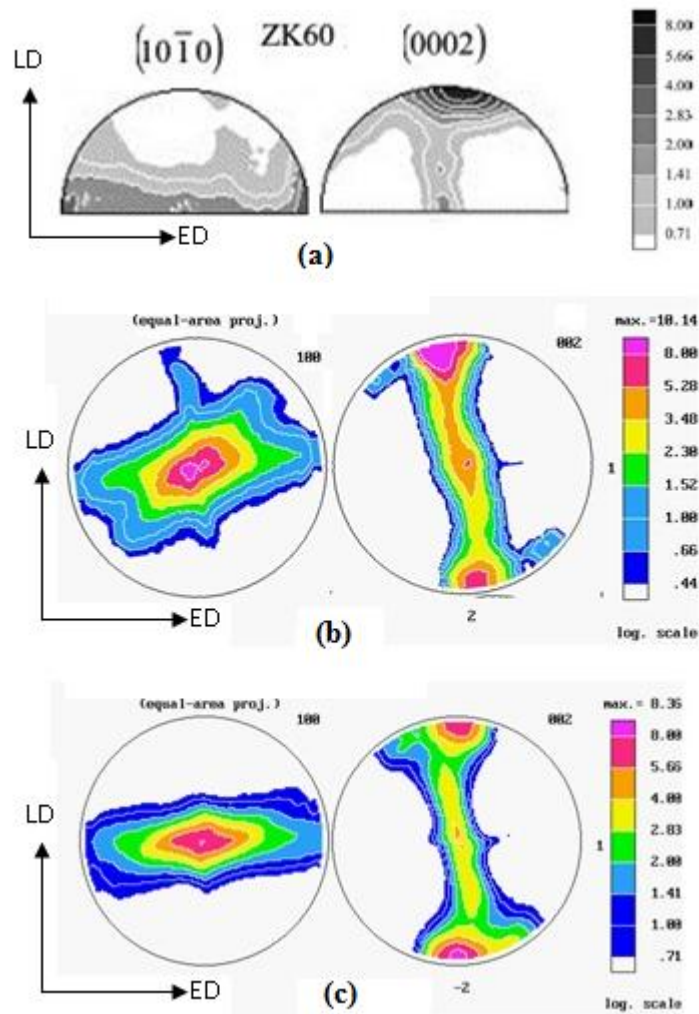


Figure 3.3.15. (a) Prismatic and basal pole figures of 4A processed ZK60 at 260 °C [28, 29]

(b) Prismatic and basal pole figures of 4A processed ZK60 at 200 °C.

(c) Prismatic and basal pole figures of 4A processed ZK60 at 150 °C.

As observed in the figure, decreasing processing temperature sharpens the basal and prismatic textures. The basal fibers become more away from LD as temperature increases. Especially, when basal textures of S10 and S11 are studied and compared with the literature data [27, 28], it can be observed that as

the ECAE temperature increases, the basal pole components tend to spread with a certain angle from LD, and the intensity of the basal poles that lie along LD decreases. These findings are verified by the reports in literature. Al-Samman et.al reported that increasing the processing temperatures results in the tendency for splitting of basal pole around LD for pure Mg and the intensity decreases as the temperature increases [151]. These widening and splitting of the poles may lead to activation of basal slip, as discussed in the previous chapter. This would be an important factor that leads to the decreased yield strength with increasing temperatures and surely will affect the flow stress anisotropy.

The texture surely does affect the mechanical behavior; but the microstructure due to the processing temperature also plays an important role, as mentioned. The tension and compression tests are performed on both cases under three orthogonal directions to explore these effects. The results of the compression tests are given in Figure 3.3.16 (a) and (b) for S10 and S11, respectively.

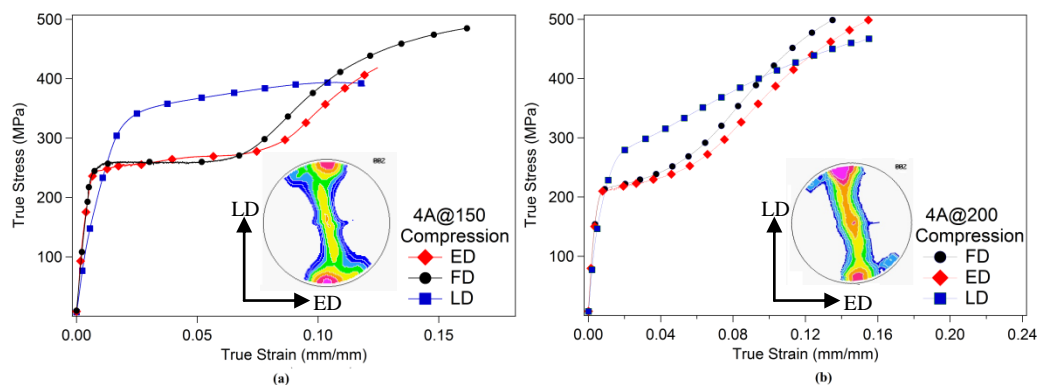


Figure 3.3.16. Compressive response of (a) S10 and (b) S11.

For S10, yield strength elongation is observed when compressed along FD and LD. This is again due to tensile twinning, which was expected when the pole figures are investigated. The behavior of LD, however, is different than that of FD and ED. The sample undergoes more elastic deformation and yields at a

larger stress value by pyramidal slip and maybe even compressive twinning. This is much pronounced in S10 since the LD is almost parallel to the c-axis of the basal fibers. When compressed along their c-axis, the HCP materials need to be able to deform along that axis and pyramidal slip ($\langle c+a \rangle$ slip) or twinning is required to satisfy the structural integrity and the force equilibrium between the grain boundaries. Since the material is under compression, tensile twinning is not expected. Accordingly, the deformation is thought to take place by basal, pyramidal slip and compressive twinning, but the mechanism is not clear. The lower Young's modulus, E , is another sign of basal slip taking place, but this does not necessarily mean that basal slip is the only mechanism.

S11 also shows a similar behavior, where twinning in ED and FD is less compared to S10; and the samples compressed along LD exhibit more hardening than its companion. The reason for this is again the deformation modes that are active during the testing.

Figure 3.3.17 gives the behaviors of S10 and S11 specimens under tensile loading.

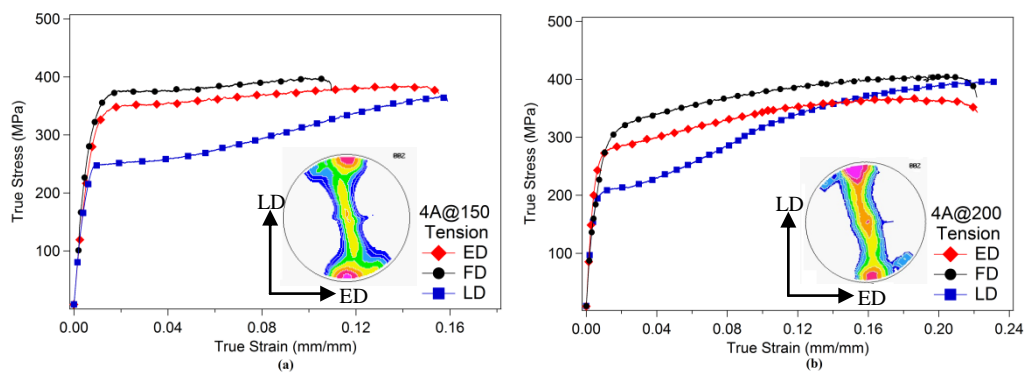


Figure 3.3.17. Tensile response of (a) S10 and (b) S11.

The mechanical properties of S11 are summarized in Table 3.3.4.

Table 3.3. 4. Mechanical properties of S11.

		TENSION			COMPRESSION		
		σ_y (MPa)	σ_{UTS} (MPa)	%strain (mm/mm)	σ_y (MPa)	σ_{max} (MPa)	%strain (mm/mm)
S11	ED	281 ±3	361 ±7	21.2 ±0.1	197 ±9	513 ±14	15.5 ±0.3
	FD	320 ±4	403 ±4	21.1 ±0.4	209 ±7	519 ±21	14.8 ±1.1
	LD	202 ±4	400 ±4	23.9 ±1.2	255 ±6	468 ±24	15.5 ±0.4

He et al. [137] reported a tensile YS of 120 MPa and an UTS of 221 MPa for ZK60, processed through route 4A at 240 °C. Their as-received sample's tensile YS and UTS are 166 MPa and 250 MPa, respectively. Their results showed that the strength values of the samples decreased after processing under the stated conditions. The as-received sample's mean grain size, which was around 80 μm is decreased to 1.8 μm . It should be noted that the decrease in the strength took place despite this grain refinement. Since ECAE process in the study was carried out at 240 °C, which is above the recrystallization temperature of ZK60 alloy (around 200 °C), the authors concluded that the DRX took place and played an important role during the deformation.

Our as-received sample, S4 has a tensile YS and UTS of 271 MPa and 371 MPa, respectively. These values for S10, which is processed at 150 °C are 344 MPa and 396 MPa, respectively. S11, however, yielded at 280 MPa, and has an UTS value of 361 MPa. Studying these results, it can be observed that S11, being processed at around the recrystallization temperature of ZK60 alloy, 200 °C, has not shown a significant increase in mechanical properties. This can be attributed to the effect stated above; DRX being competent to hardening and their effects

are somehow equalized. For S10, the increase in the YS is intense. It seems that hardening due to dislocation accumulation and twinning (Hall-Petch effect) and basal pole sharpening won the battle against DRX in this case, and resulted in such increased strength values. When studied carefully, it is observed that the basal fibers rotated along LD to some extent, as seen in Figure 3.3.18 for S11. This makes the basal slip more possible and results in the yielding of the material earlier than S10, whose basal fiber lies almost parallel to LD. The processing temperature is way below the recrystallization temperature, and the decrease in grain size from 1.99 μm to 1.89 μm ; combined with the sharp basal texture explains this behavior perfectly.

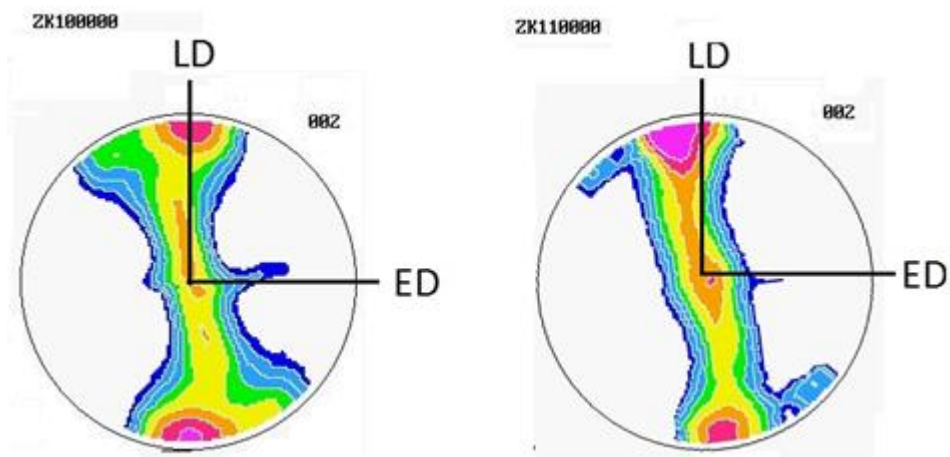


Figure 3.3.18. Comparison of the basal fibers of (a) S10 and (b) S11.

3.3.3. ECAE Processed Samples: Hybrid Routes

The nature of the initial structure of the starting materials is very critical in microstructure evolution during ECAE procedure. As fine grained materials are more adjustable to severe plastic deformation, a fine grained material may exhibit better workability compared to larger grained companions [137].

Regarding this, the researchers aimed to process materials with low grain sizes through ECAE to achieve better formability. One approach to follow this method is to develop two step ECAE procedures like EX-ECAE [152]. In this process, the ZK60 billet goes through simple extrusion before entering the ECAE channel. The extrusion process results in refined grain size, which facilitated the subsequent 200 °C ECAE deformation. Second approach is to process the sample by ECAE at high temperature, then subsequently at lower temperatures. This method is employed by Jin et.al, and their study reported an ultra-fine grain of 0.5 μm , and significant improvement in both the ductility and strength of the alloy after the processing [153]. The authors explain this improvement by grain refinement as well as incomplete dynamic recovery and recrystallization during the processing. This successful work pioneered the “hybrid route” development, where the material is processed at higher temperatures first, to obtain a homogenized microstructure with smaller grain sizes. The following steps are processed at decreasing temperatures to benefit from the low temperature processing effects and using the advantage of formation of fine grains in the previous passes since they are more prone to handling severe plastic deformation. Following this approach, Mg and its alloys are processed at lower temperatures at the increasing number of passes; and finally; processing of Mg at room temperature at 8th pass with ECAE is reported by Biswas et.al [120], as mentioned before.

In this study, hybrid route formation is employed to achieve optimum properties for the ECAE processed ZK60 billets. Accordingly, 200 °C was selected as the starting temperature in most of the hybrid cases since most of the ECAE studies on Mg and its alloys reported that this is the minimum temperature that extensive shear localization is not observed [27]. Although shear localization is not observed for the specimens that are processed at 150 °C, the amount of back pressure employed to achieve this is quite high, resulting in the excessive

material loss during machining process in between the consequent passes. Besides, as mentioned, 200 °C still allows benefiting from the positive effects DRX; developing fine grains and potentially increasing material strength and allowing grain boundary sliding [154, 155].

Hybridizing is realized not only by altering the processing temperatures; but also processing routes would change throughout the whole process. As mentioned in Section 3.3.2.1, the texture of the workpieces processed by route A exhibits a noticeable feature. The (0002) poles are aligned almost all through the longitudinal direction. This texture, in fact, causes in the distinctive mechanical response of the processed samples. The main characteristic of the billets with “A textures” is that they exhibit high strength values under tension and compression but their ductility is not extraordinary. The (0002) poles around the FD causes decreases in expected strength in FD as it would result in tensile twinning under compression along FD and inhibits extra hardening. This can be observed by the plateau following the elastic deformation at the true stress-true strain curve. Since ECAE is a plane strain process, these components are unavoidable. Route B_C only strengthens this component causes the same effect. This, when combined with the more homogeneous grain distribution and size obtained, results in less increase in strength. Route C, on the other hand, results in components that lie with an angle to the LD that do not contribute the strengthening much, but increases the ductility [12, 24]. This is simply due to the easy activation of basal slip when the specimen is tested through LD or ED, that is, since the (0002) poles lie at the angle that basal slip takes place. As a result, ECAE process can be hybridized to benefit from the high strength values coming from the “A texture” and the high ductilities associated with “C texture”; combined with the desired temperature effects discussed above.

The case S20 imitated the study performed on Mg alloy AZ31 by Modarres Razavi et.al (to be published in Scripta Materialia), which yielded exceptionally improved results. However, S20 did not exhibit that much of increase in mechanical properties despite going through the same deformation conditions. This is attributed to the difference in starting textures and deformation behaviors of the Mg alloys.

ECAE of S11, S27 and S21 aimed a systematic study that investigates the changes in the microstructure, mechanical properties and textures step by step, through the stages of processing, S21 (4A@200 °C+180°rot+2A@150 °C +180°rot+2A@150 °C) yielding improved results.

S23 is slightly different from these cases, since its first step is not a 4A processing; but is a 2A@200 °C, continued by 2A@150 °C and 1A@125 °C; applying rotations of 180° between these 3 stages. Surprisingly, this case yielded very large compressive strengths.

S28 is studied for the ECAE temperature lowering attempts, and the first step of the process is 4A@150 °C, not 4A@200 °C. The obtained results are very promising, emphasizing that the starting grain size is a more important factor than decreased processing temperatures in achieving better mechanical properties.

Details of these cases are given below.

3.3.3.1 A “Step-by-Step” Approach: S11, S27 and S21

While developing the hybrid routes, the data obtained from the performed experiments, theoretical information and literature study results are considered. Those data should be evaluated carefully and used at the right steps of a successful ECAE deformed materials through hybrid routes.

Studying the literature, and the studies performed at MESAM Lab, it is very common to observe that the hybrid processing of Mg and its alloys, including ZK60, a temperature around the recrystallization temperature is generally chosen for the early stages of the hybrid route processing. This temperature is 200 °C for ZK60 alloy [137]. Deformation at 200 °C would bring an advantage of microstructural homogenization and introduce DRX to the material. This may seem like a disadvantage; however, DRX leads to the formation of new strain free grains which results in a more uniform microstructure and may even break down the possible elongated grains that are formed during extrusion process. Considering that extruded Mg is already a very hard-to-deform material, relieving the stored energy by DRX would result in the ease of ECAE operation. Another point is that, this deformation and those new strain-free grains are good for avoiding the twin formation. Although twinning is known to increase the strength of the materials during mechanical testing, they are not wanted in the billets, if the billet is going to be deformed through more ECAE passes. Twin boundaries are possible micro-crack nucleation sites and the micro-cracks may lead to the failure of the billet in the following passes due to those potential cracks.

Considering this, almost the entire hybrid routes are designed such that they are ECAE processed at 200 °C first. S21 is an example for this, and 4A@200 processing is applied as the starters. In other words, S11 is continued to process

in this hybrid route. The properties of S11 were already discussed in Section 3.3.2.2, but the mechanical properties and the prismatic and basal pole figures are shown here for the sake of the continuity of the discussion.

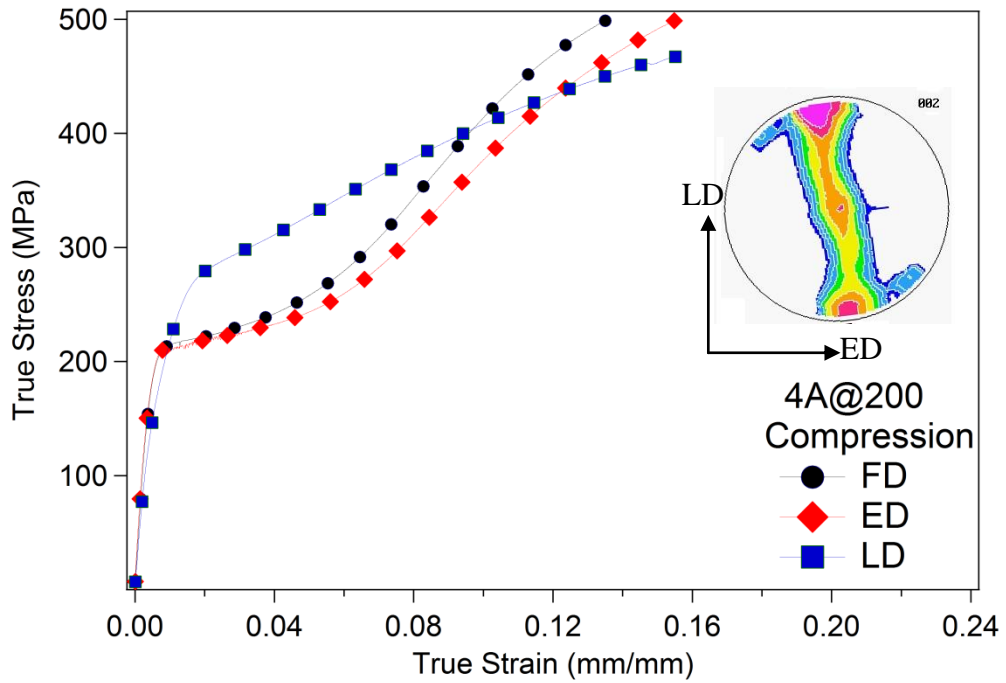


Figure 3.3.19. Compressive response of S11 along three orthogonal directions.

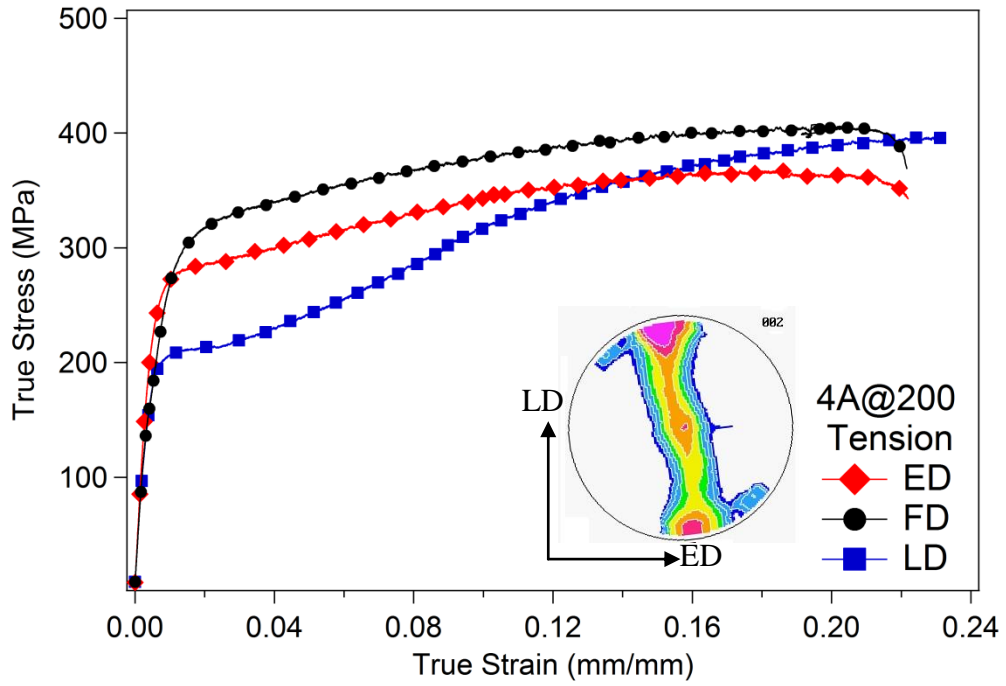


Figure 3.3.20. Tensile response of S11 along three orthogonal directions.

Table 3.3.5. Mechanical properties of S11.

		TENSION			COMPRESSION		
		σ_y (MPa)	σ_{UTS} (MPa)	%strain (mm/mm)	σ_y (MPa)	σ_{max} (MPa)	%strain (mm/mm)
S11	ED	281	361	21.2	197	513	15.5
	FD	320	403	21.1	209	519	14.8
	LD	202	400	23.9	255	468	15.5

The textural evolution of S11 was as follows:

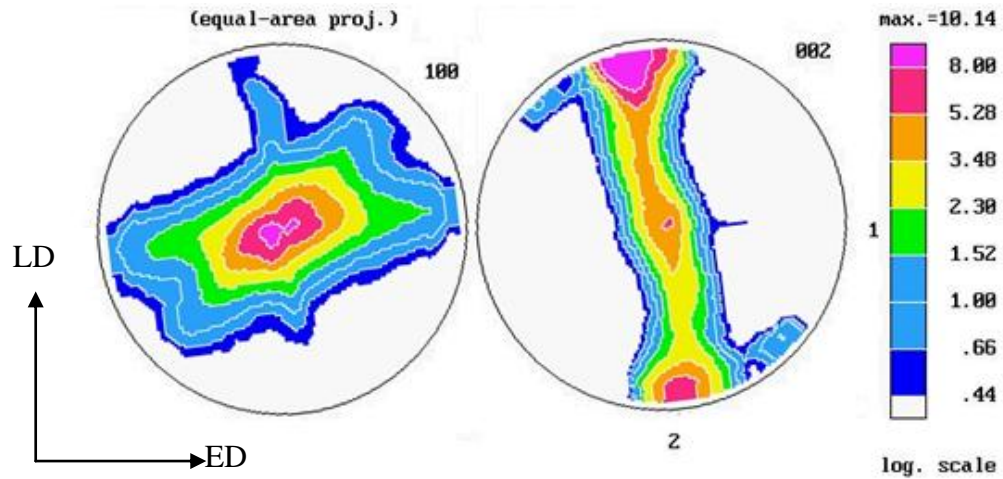


Figure 3.3.21. Prismatic and basal pole figures of S11.

After obtaining the 4A@200 processed billets, it was decided to benefit from the step down effect. The mechanical properties were still enhanced compared to the as-received form, but since DRX took place, forming new strain free grains, processing at lower temperatures was necessary to use the mechanical property advantages that come with grain size refinement at those temperatures. Regarding this, next two passes are decided to be run at 150 °C.

As mentioned before, benefiting the lower temperature processing is not the only feature of hybrid route development. Remembering that the “A” texture that is evolved through the first four steps would increase the strength, ductility is not affected very positively from this deformation especially in certain directions. Besides, the texture of the material gets sharper and sharper through “A” processing, and it may come to a point that the stress state in the billet during ECAE would require twinning to take place. Twins, being the potential crack nucleation sites, are not much desired if the material is to be processed

more through ECAE. Accordingly, a rotation of 180° is applied after the 4th pass, to achieve a more spread texture and prevention of the twin formation.

The product at the end of this second step, 6th pass, is named as S27. The microstructure of S27 is given in Figure 3.3.22.

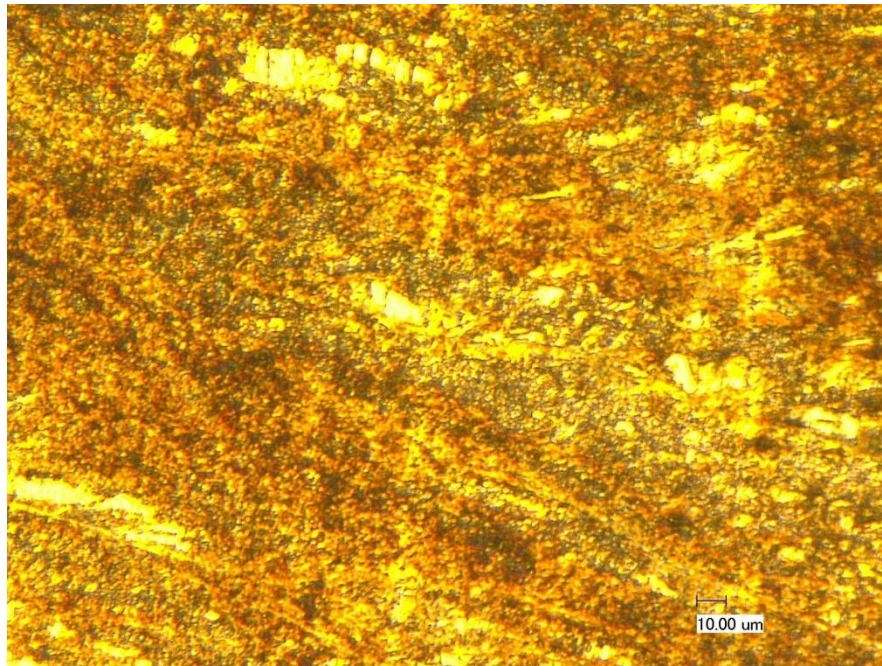


Figure 3.3.22. Microstructure of S27.

As observed, despite the bimodal grain distribution is still present in the sample, the elongated grains are observed to start breaking down. This shows that 4A+1C+1A deformation did not contribute to the refinement of the elongated grains much, since they were already present in S11 (Figure 3.3.12). The equiaxed grain size was measured to be $1.61 \mu\text{m}$ with a standard deviation of 0.6. The refinement in equiaxed grains and partial disintegration of the elongated grains would surely be advantageous while the mechanical properties are studied, since 150°C and 125°C are quite below the recrystallization temperature of ZK60 and would let the Hall-Petch effect be pronounced in the

mechanical behavior. This, combined with the textural features (Figure 3.3.23), will determine the mechanical response of the samples.

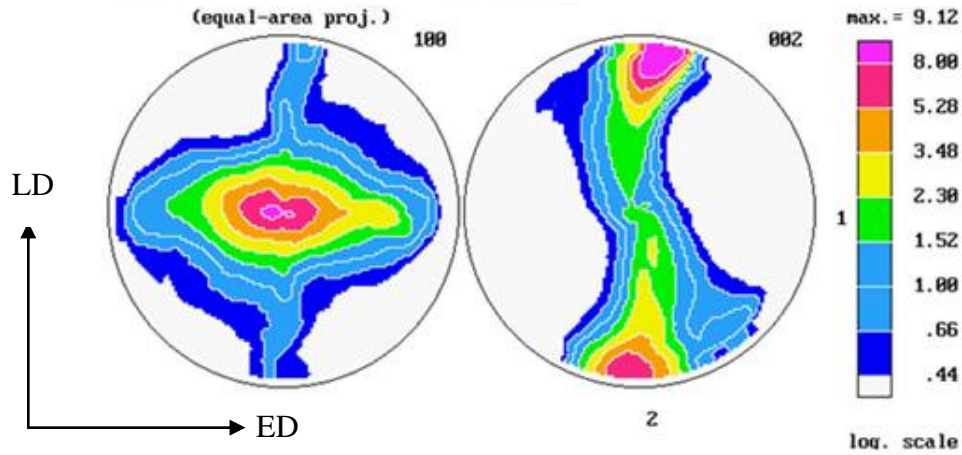


Figure 3.3.23. Prismatic and basal pole figures of S27.

As observed from the pole figures, the basal peak splitting is not much pronounced despite applying a 180° rotation in between the 4th and the 5th steps. Instead, a spreading of the basal peak around LD is observed. However, the basal peak's intensity is increases as well. This texture is expected to yield improved mechanical properties, when accompanied by the refined microstructure. This expectation is observed to be met when the compression and tension test results along three orthogonal directions are studied. The stress-strain curves of these cases are given in Figures 3.3.24 and 3.3.25, respectively.

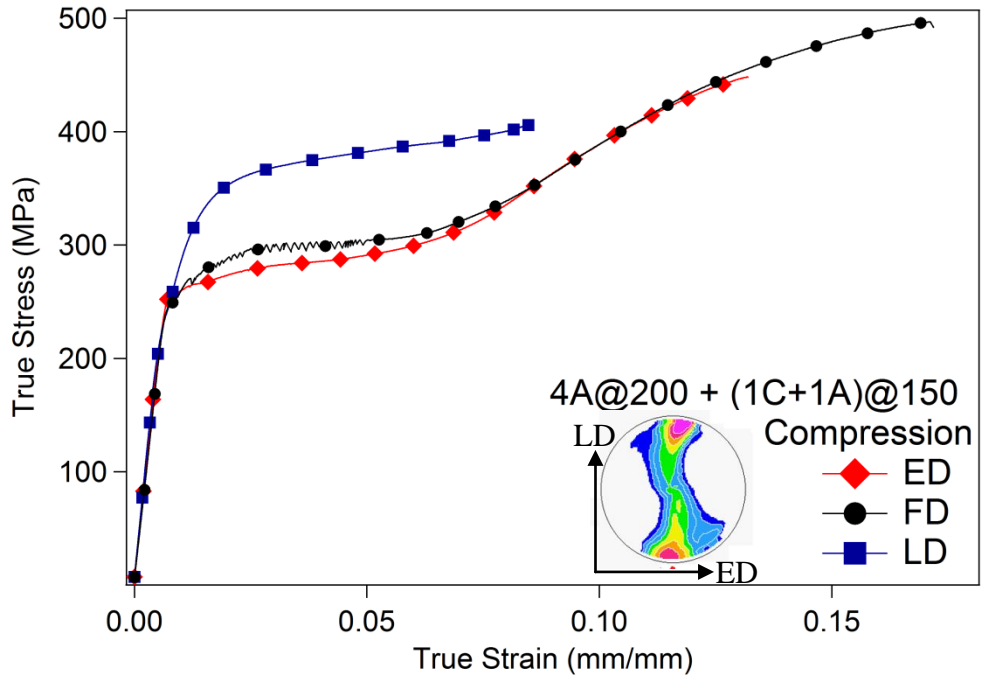


Figure 3.3.24. Compressive response of S27 along three orthogonal directions.

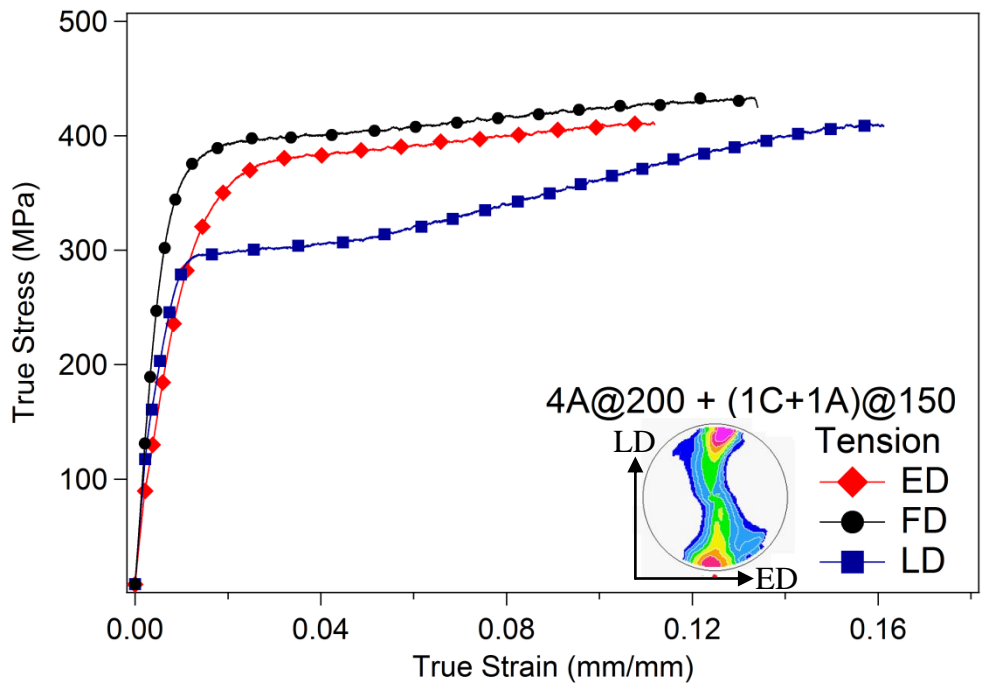


Figure 3.3.25. Tensile response of S27 along three orthogonal directions.

Studying the figures, it is observed that when the sample is compressed along its LD, yielding takes place at higher stress values. This is due to the fact that the stress required for the activation of non-basal slips is much higher than that of the basal slip. Since the orientation is not favored by basal slip; and the contraction along LD requires dimension change along the c-axis, pyramidal slip is accepted to take place. Compressive twinning, as mentioned, is not favored much by ZK60. However, it may also be activated at the last stages of the testing along LD and cause the failure. Behavior of the sample along ED and FD are quite similar, since application of compressive load along these direction acts as if there is tension along LD. Accordingly, tensile twinning takes place and the material rapidly hardens until fracture. A similar explanation can be used for the tensile testing. When tested along LD, the tensile specimen shows tensile twinning and undergoes yield stress elongation, followed by hardening. This hardening is not as rapid as the post-twinning hardening that is observed under compressive loads. This behavior is related to the activation of different slip modes in these cases. Samples pulled along FD and ED of the specimen exhibits hardening by non-basal, mainly prismatic slip. The improved mechanical properties are summarized in the following Table 3.3.6.

Table 3.3.6. Mechanical properties of S27.

		TENSION			COMPRESSION		
		σ_Y (MPa)	σ_{UTS} (MPa)	%strain (mm/mm)	σ_Y (MPa)	σ_{max} (MPa)	%strain (mm/mm)
S27	ED	355 ±4	410 ±7	11.1 ±0.1	249 ±7	450 ±9	13.2 ±0.2
	FD	376 ±4	433 ±6	13.3 ±0.2	274 ±6	496 ±7	16.9 ±0.2
	LD	296 ±7	410 ±6	16.0 ±0.1	350 ±7	406 ±5	8.5 ±0.4

The third part of the route aimed to benefit the deformation still at 150 °C, however a rotation of 180° is employed to avoid any possibility of fracture due to the application of “4A@150” and to have A+C texture. That was performed successfully in S10 but due to the increased number of passes; the rotation was decided to be necessary. Applying the 2A@150 after 180° rotation of the billet, S21 is obtained.

After applying 8 passes, the billet became pretty short (Figure 3.3.26). Despite this, the tensile and compressive test specimens were obtained from the fully deformed region.



Figure 3.3.26. Processed billet S21.

The microstructure of the S21 is investigated by optical microscopy. The images are shown in Figure 3.3.27.

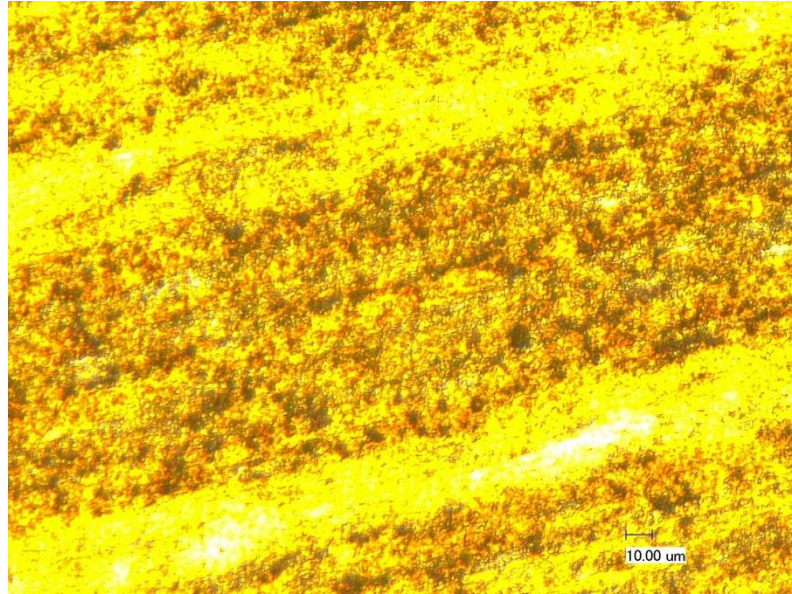


Figure 3.3.27. Microstructure of S21.

The average grain size of the sample is measured to be 1.69 μm with a standard deviation of 0.06 μm.

When the textural evolution of S21 is investigated, an unexpected feature is observed. The prismatic and basal pole figures of S21 are given in Figure 3.3.28.

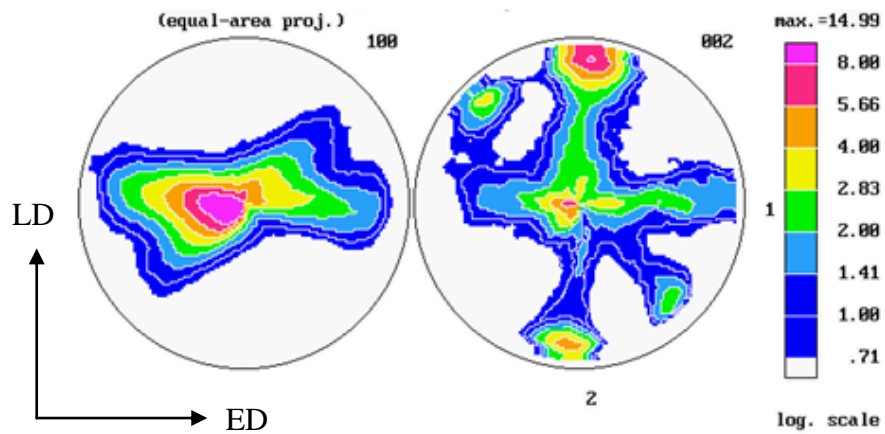


Figure 3.3.28. Prismatic and basal pole figures of S21.

The basal pole splitting catches one's eye at first sight. The textural evolution resembles that of C, since the split peaks around LD are present. There is also a tendency to lie along ED at basal fibers, however this effect is insignificant.

The mechanical response of S21 is presented in Figures 3.3.29 and 3.3.30 for compressive and tensile testing, respectively.

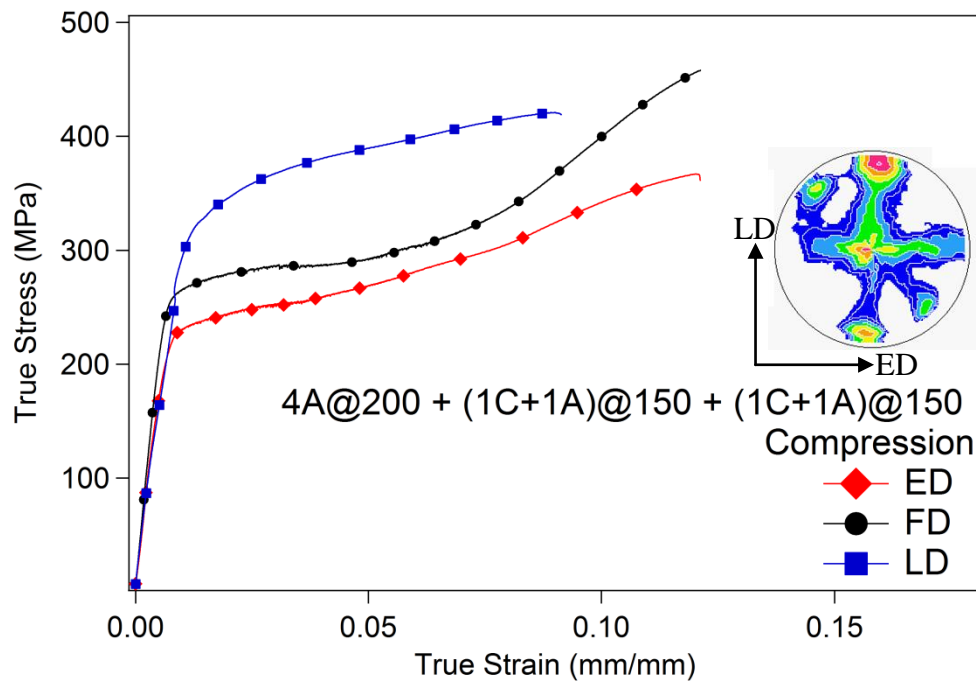


Figure 3.3.29. Compressive response of S21 along three orthogonal directions.

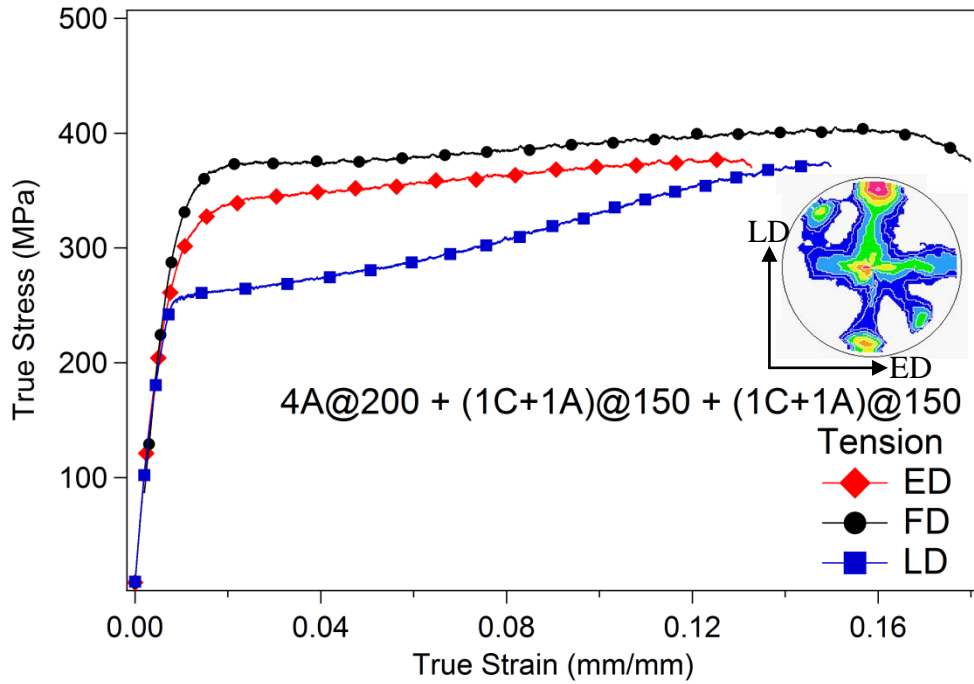


Figure 3.3.30. Tensile response of S21 along three orthogonal directions.

Remembering that the compressive behavior of S27 when tested along FD and ED are almost the same, the curves' moving apart from each other is interesting. Here, a difference of 40 MPa in yield stress values are observed. Other than that, the curves show characteristics that were mentioned in the previous section. The mechanical properties obtained from these tests are summarized in Table 3. 3.7.

Table 3.3. 7. Mechanical properties of S21.

		TENSION			COMPRESSION		
		σ_y (MPa)	σ_{UTS} (MPa)	%strain (mm/mm)	σ_y (MPa)	σ_{max} (MPa)	%strain (mm/mm)
S21	ED	326 ±6	377 ±4	15.1 ±0.2	223 ±5	367 ±11	12.0 ±0.3
	FD	366 ±7	401 ±11	16.6 ±0.3	251 ±6	456 ±14	12.0 ±0.3
	LD	253 ±9	367 ±12	14.2 ±0.2	333 ±3	421 ±16	8.9 ±0.5

After giving the mechanical behavior data of the samples that are obtained after each step, their comparison is necessary. The evolution of yield stress under tension and compression are given in Figure 3.3.31 (a) and (b), respectively.

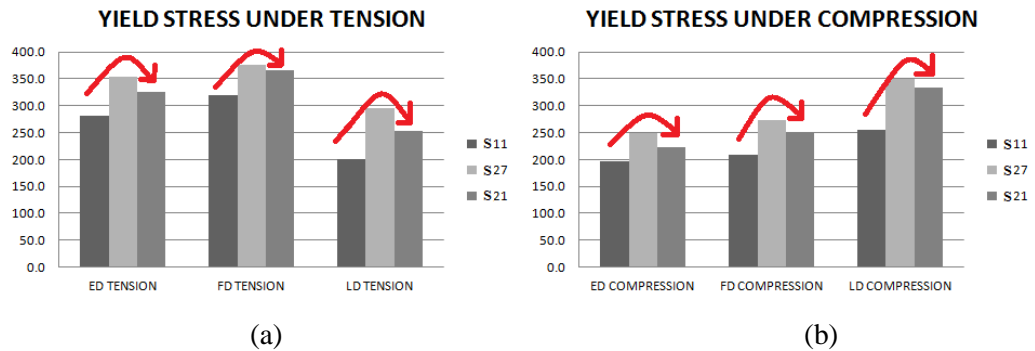


Figure 3.3.31. Yield stress through the processing steps of S21.

In all of the cases, yield stress is observed to be in an increasing trend until the final step. Despite undergoing further deformation at a comparatively lower temperature, the final step did not result in any increase in these values. On the contrary, an important amount of decrease is observed. The effect of DRX is eliminated at this point, since the last step was applied at 150 °C, which is way below the recrystallization temperature of ZK60. Observing that the grain size did not change significantly as well, the only factor that explains this behavior is the texture evolution.

Figure 3.3.32 (a) and (b) gives the prismatic and basal pole figures of S27 and S21, respectively.

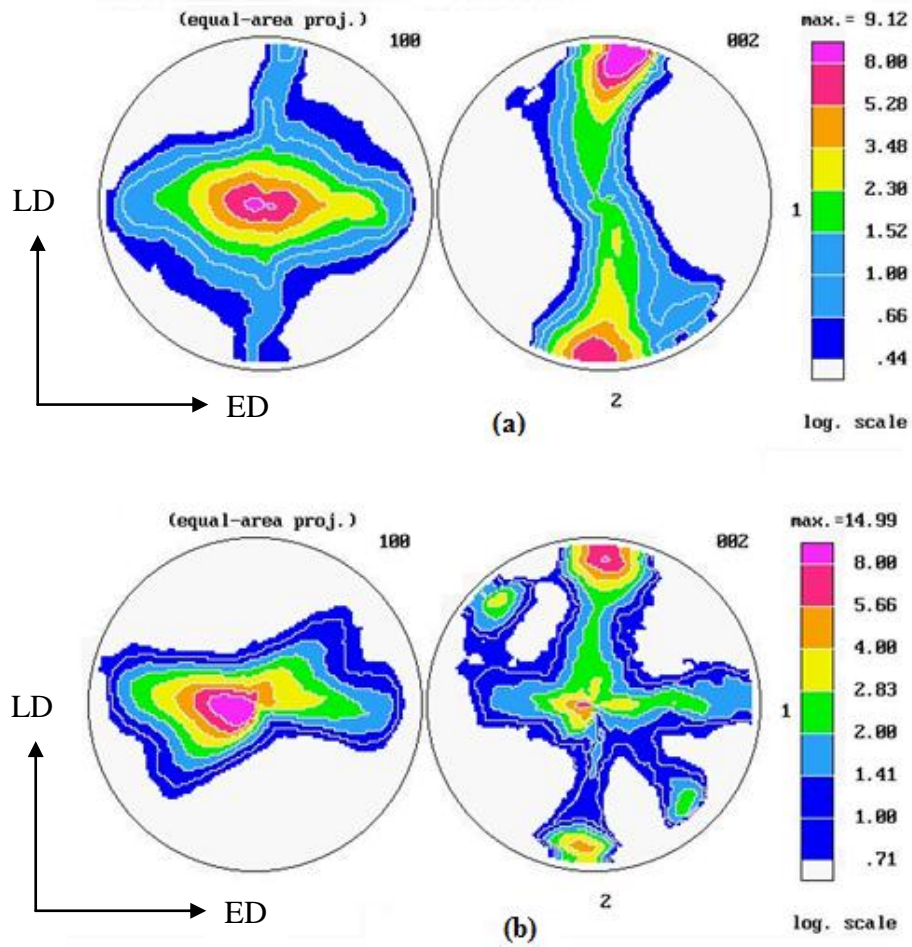


Figure 3.3.32. Prismatic and basal pole figures for (a) S27 and (b) S21.

The basal pole figure of S21 has peaks that are oriented at around 45° from LD. Those were not present in S27's basal pole figure. That means there are basal fibers that lie in the direction that is favorable for basal slip to take place. Since the CRSS for basal slip is way lower than that of non-basal slips, it is inevitable to observe decreased yield strength values once those peaks are formed. This is a very solid proof that shows textural evolution plays a very important role in mechanical property enhancement, maybe even more than we anticipate.

3.3.3.2 Help from Literature: S20

S20 is deformed under the hybrid route of 4A@200+1C@150+1C@125. This case is studied on AZ31 by Modarres Razavi of MESAM Lab, Texas A&M University. The scientist obtained very promising results in her study. Inspired by this success, the same route was applied on ZK60 as well. However, as will be discussed in the following paragraphs, same amount of improvement in mechanical properties could not be achieved for our material. Nevertheless, the improvement is still significant and is worth mentioning here.

The microstructure of the S20 processed sample is investigated by optical microscopy. The images are shown in Figure 3.3.33.

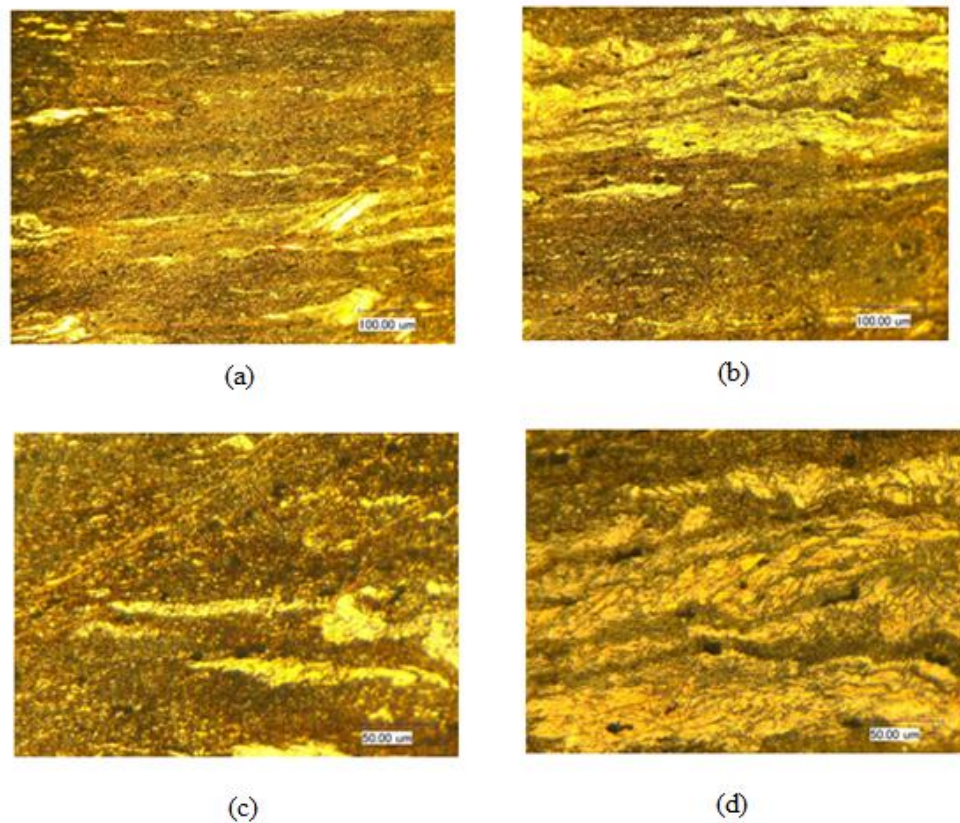


Figure 3.3.33. Optical microscopy images of S20 with magnifications of (a) X800, (b) X800, (c) X1000, (d) X1000.

As observed, bimodal grain size is preserved in the sample. However, the fracture of the elongated grains is significantly observed. The equiaxed grain size was measured to be $1.63 \mu\text{m}$ with a standard deviation of $0.08 \mu\text{m}$ for the sample. This decrease, combined with the textural features (Figure 3.3.34), will determine the mechanical response of the samples.

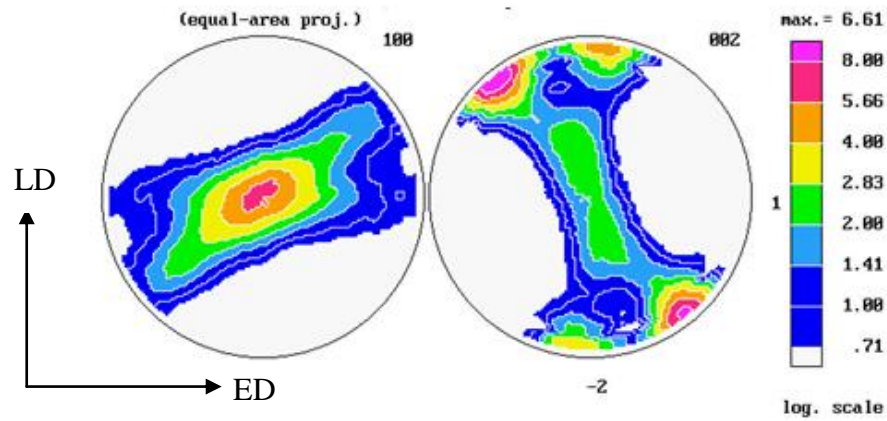


Figure 3.3.34. Prismatic and basal pole figures for S20.

The route successfully employs step-down effect and almost benefits the C+A texture (mentioned in Section 3.3.2.1) the important point of going down to 125 °C while processing, surely would give interesting results and different mechanical responses.

These mechanical responses are again studied in terms of tension and compression behavior. The compression test results of this case are presented in Figure 3.3.35.

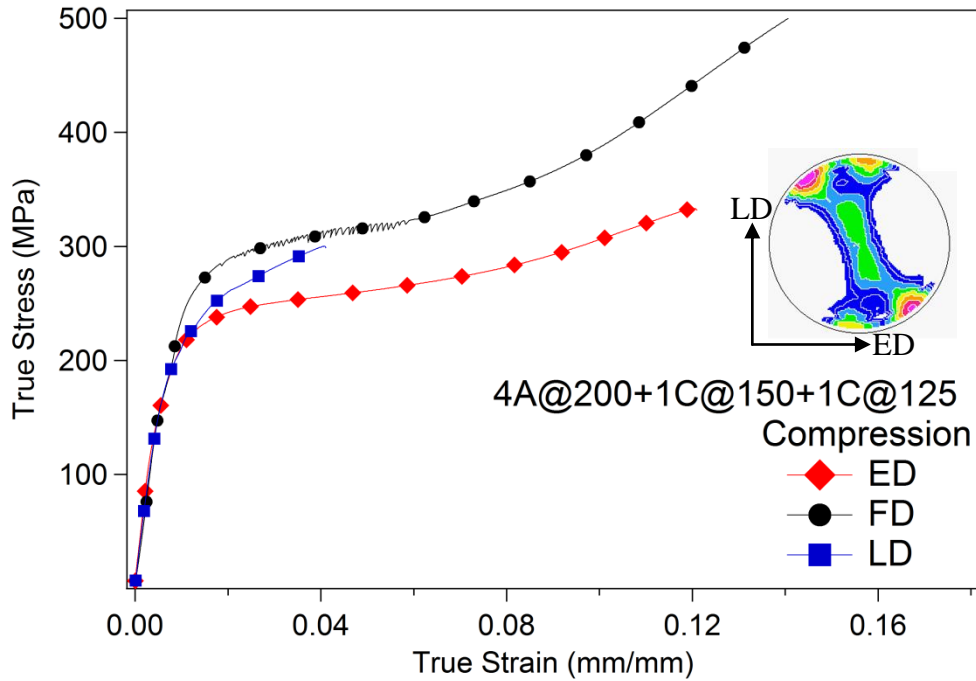


Figure 3.3.35. Compression test results of S20 in three orthogonal directions.

While studying the curve, it is observed that the sample tested along FD exhibited the highest yield stress again. The sample is expected to undergo tensile twinning, when the texture (Figure 3.3.34.) is considered, and so is the case. The twinning is so intense that the striations at the stress-strain curve became visible. The plateau with these striations is spotted in the case; however, one easily notices the slight work hardening during the twinning takes place as well. This is due to basal slip and expected since the basal poles are more spread along LD, and fibers aligned even by approximately 41 degrees are present as shown in Figure 3.3.36. The peak splitting is common for A+C textures, as mentioned before.

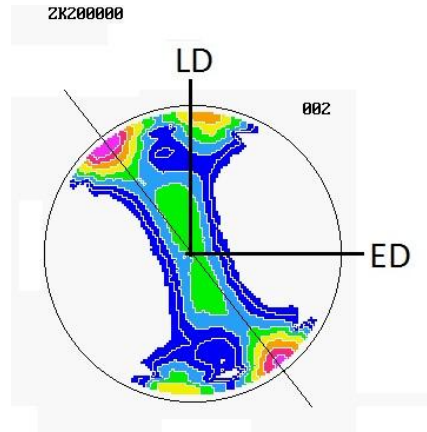


Figure 3.3.36. Peak splitting in S20.

The tensile stress-strain curve of S20 is given in Figure 3.3.37.

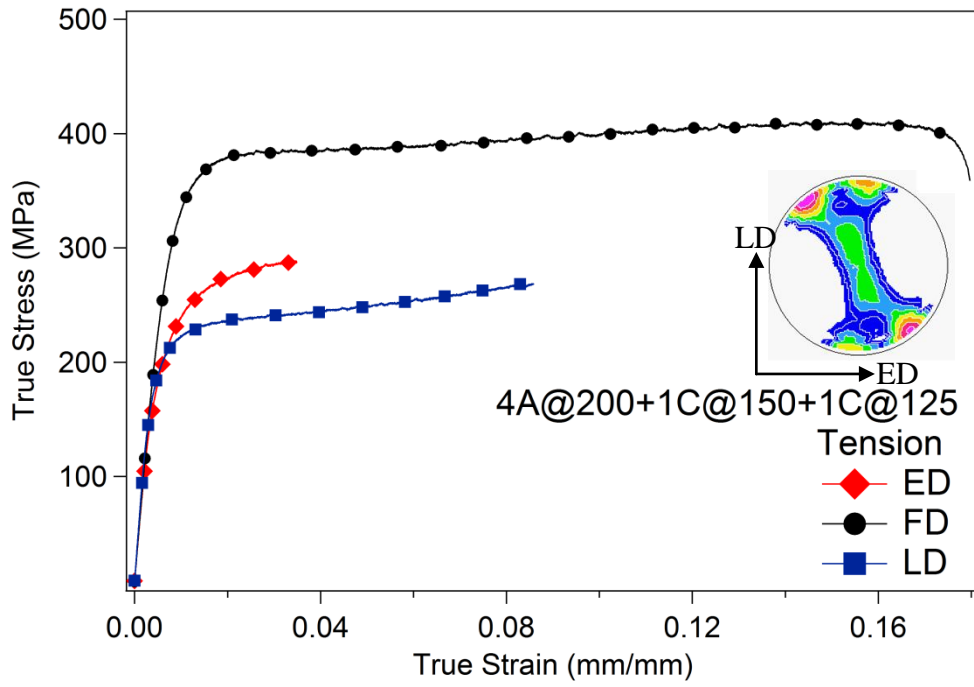


Figure 3.3.37. Tensile test results of S20 in three orthogonal directions.

The mechanical properties associated with these curves are given in Table 3.3.8.

Table 3.3.8. Mechanical properties of S20.

		TENSION			COMPRESSION		
		σ_Y (MPa)	σ_{UTS} (MPa)	%strain (mm/mm)	σ_Y (MPa)	σ_{max} (MPa)	%strain (mm/mm)
S20	ED	238 ± 6	285 ± 7	3.4 ± 0.1	212 ± 9	333 ± 8	12.1 ± 0.8
	FD	367 ± 9	407 ± 5	16.9 ± 2.9	264 ± 8	534 ± 15	15.5 ± 0.9
	LD	211 ± 2	267 ± 5	8.5 ± 1.2	259 ± 4	299 ± 8	4 ± 0.1

Tensile twinning is actually not expected when tested along FD since the loading direction is perpendicular to FD and pulling along FD would result in the “fattening” of the basal fiber, and non-basal slip with compressive twinning by the end of the deformation are assumed to be present.

The reason for the “less improvement in ZK60” compared with the striking improvement at AZ31 is mainly attributed to the differences in starting texture. It is stated in literature that the most important factor for texture evolution in a material is the starting texture [12, 24]. For AZ31, the billet was cut from a hot rolled plate, with an initial texture as shown in Figure 3.3.38.

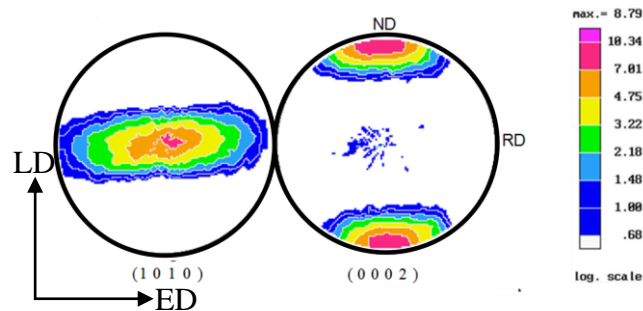


Figure 3.3.38. Characteristic prismatic and basal pole figures of a hot rolled plate.

In the pole figure, it is observed that the basal fibers are aligned almost along LD. There is no FD component in basal pole figure. This is important because the FD components reduce the strength values. In extruded ZK60, the basal fibers lying along FD is inevitable due to the starting texture. Remembering that ECAE is a plane-strain process, there is no way to get rid of this component. AZ31 uses the advantage of the absence of those components, and yield better results accordingly.

Comparing this case with S21, the previously mentioned case, one can make some very important deductions. Despite going to a very low temperature of 125 °C in S20, the improvement in mechanical properties is not much striking. When the comparison between S10 and S11 is considered, the only variable being the processing temperature, one would expect tremendous improvement in mechanical properties for S20 when compared to S21. For tension tests, yield strengths along ED, FD and LD are 238 MPa, 367 MPa and 210 MPa, respectively. The tensile stress value for S21 when tested along FD is 365.6 MPa, almost the same with S20.

3.3.3.3 Insisting on Lower Temperatures: S28

After successfully processing the as-received ZK60 billets at 150 °C without any strain localizations or fracture, the possibility of continuing the low temperature deformation was questioned. In almost all the cases in this study, lowering the processing temperature increased the mechanical properties if the evolved texture is also on our side. Hybrid processed sample ZK28 aimed to benefit the advantages associated with processing at 150 °C further. However, it was found to be too risky to continue with straight “A” route due to the reasons stated at Section 3.4.3.1. Accordingly, a 180 rotation of the billet between the 4th and 5th

pass is decided to be necessary. Considering these factors, S28 is processed as 4A@150+180° rotation+2A@150.

To be on the safe side, a back pressure around 70 MPa was applied during processing. The accompanying material loss, when combined with the small surface cracks appeared on the upper side of the billet by the end of the 6th pass, made us to decide not to process the sample further.

The microstructural evolution of S28 is shown in Figure 3.3.39.

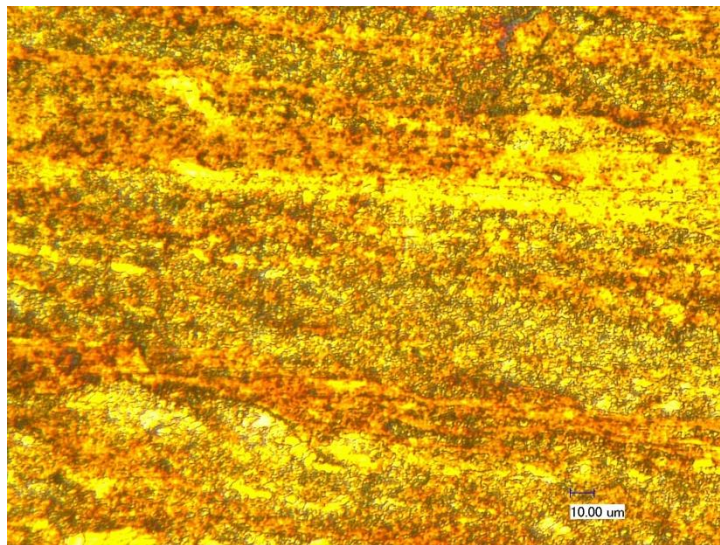


Figure 3.3.39. Optical image of S28.

The equiaxed grain size was measured to be 1.72 μm with a standard deviation of 0.09 μm. This, combined with the resulting texture (Figure 3.3.40), will determine the mechanical response of the samples.

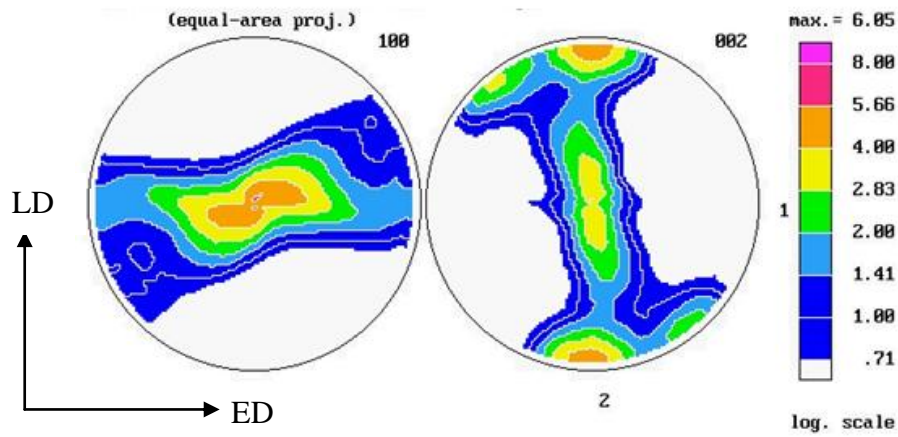


Figure 3.3.40. Prismatic and basal pole figures of S28.

Studying the figure, it can be mentioned that S28 is one of the samples whose pole figures are evolved such that the basal peak splitting is significant. The pole figure looks closer to the ideal “A+C” texture. The FD components are still present. This splitting, however, is expected to cause an increase in the activation of basal slip when compressed along FD and ED; or pulled along LD. This would obviously cause a decrease in the strength values, but of will compete the advantages that comes with increasing number of passes at the same temperature and the accompanying microstructural features. The winner of this fight is ZK28, whose compression and tension test results along three orthogonal directions are presented in Figures 3.3.41 and 3.3.42, respectively.

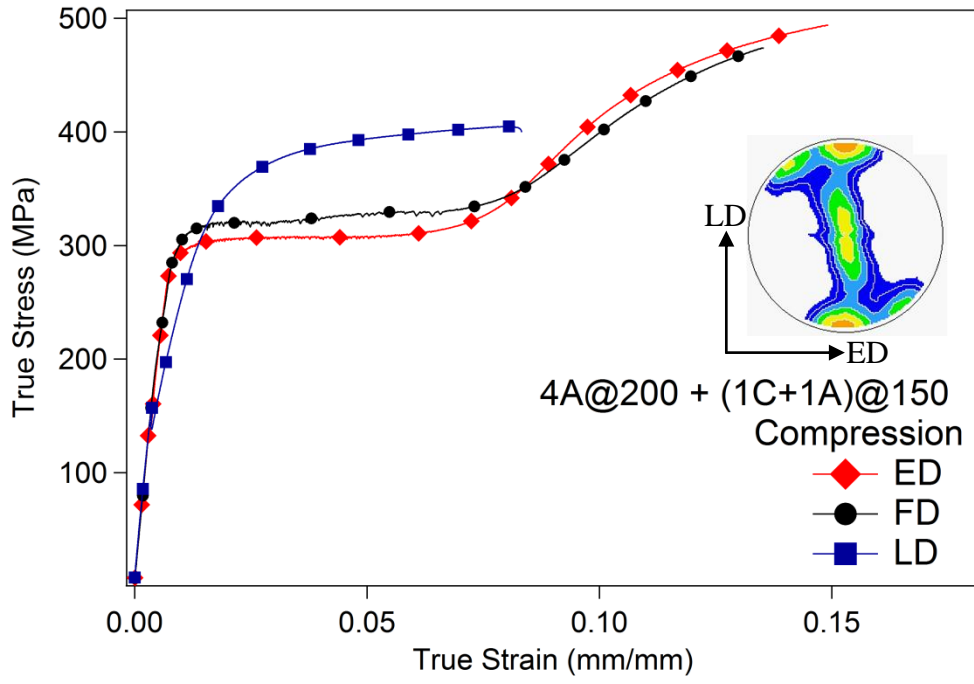


Figure 3.3.41. Compressive response of S28 along three orthogonal directions.

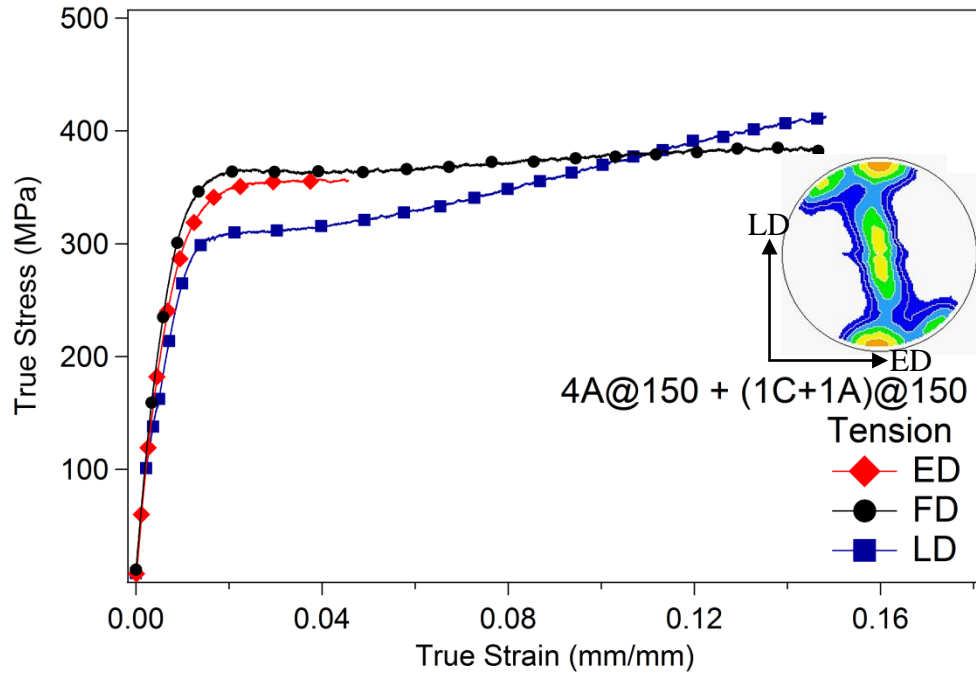


Figure 3.3.42. Tensile response of S28 along three orthogonal directions.

The behaviors are quite similar to those of S20, where the texture is very close to each other. The change in the mechanical property values is now attributed to the differences in microstructural evolution and grain size.

The mechanical properties of S28 are summarized and presented in the following Table 3.3.9.

Table 3.3. 9. Mechanical properties of S28.

		TENSION			COMPRESSION		
		σ_y (MPa)	σ_{UTS} (MPa)	%strain (mm/mm)	σ_y (MPa)	σ_{max} (MPa)	%strain (mm/mm)
ZK28	ED	401 ±6	407 ±8	4.5 ±0.2	293 ±6	493 ±6	14.8 ±0.3
	FD	406 ±7	436 ±12	14.7 ±0.6	305 ±6	473 ±9	13.4 ±0.4
	LD	304 ±3	411 ±8	11.6 ±0.9	339 ±4	405 ±6	8.1 ±0.2

3.3.3.4 A Slightly Different Case: S23

In this study, 200 °C was selected as the starting temperature in most of the hybrid cases since most of the ECAE studies on Mg and its alloys reported that this is the minimum temperature that extensive shear localization is not observed [27]. Remembering that shear localization is not observed for the specimens that are processed at 150 °C, the greed associated with low temperature processing and the success of S28 lead us to benefit the lower temperature processing passes for more number of passes. Since the length of the billet is limited, and so is the workability of the material; the possible number of passes are also limited. Accordingly route is designed to observe if high number of ECAE processing at lower temperatures is possible without any failure. Accordingly, the first step of the route is decided to be limited by 2 passes at 200 °C. The 180° rotation is applied between the 2nd and 3rd passes, to increase the workability and benefit the advantages of “C” texture. The processing temperature is decreased to 150 °C, and 2 passes at this temperature are applied. The next step would be going to lower temperatures, thus one pass at 125 °C is applied on the billet after another 180° rotation. The case aimed to go to lower temperatures according to compete the findings in the literature but a slight strain localization is observed after the last pass. Accordingly, the processing stopped at that point. The same case is

retried, but it was not successful either. So the hybrid route design of “2A@200+180°rotation+2A@150+180°rotation+1A@125” is used on the as-received billet and named as S23.

As mentioned, the last processing step at 125 °C gave a billet with slight strain localization. This might have caused inhomogeneities in microstructure, and mechanical behaviors accordingly. The microstructural evolution of S23 is presented in Figure 3.3.43.

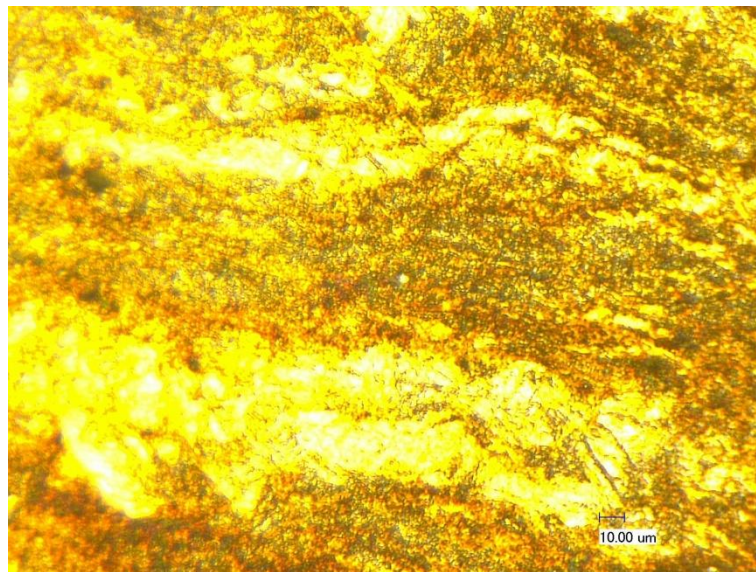


Figure 3.3.43. Optical image of S23.

The texture is measured and given in the following figure.

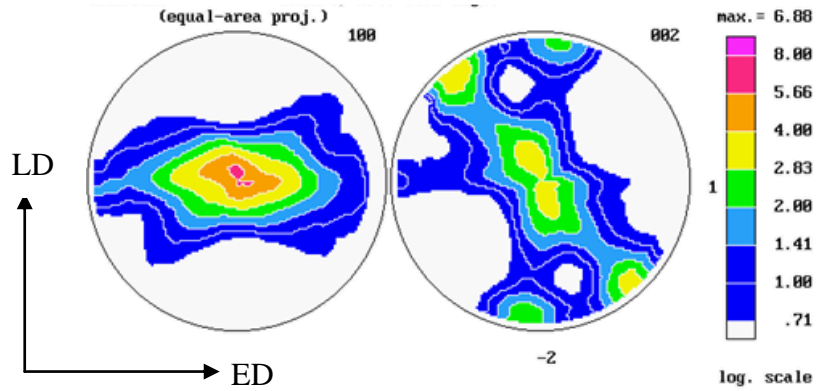


Figure 3.3.44. Prismatic and basal pole figures of S23.

As observed from the figure, the peak splitting is observed in this case. That makes the texture closer to “C” texture. Accordingly, we expect to see the mechanical response close to other “C” textured specimens. The mechanical response of the specimen is given in Figures 3.3.45 and 3.3.46.

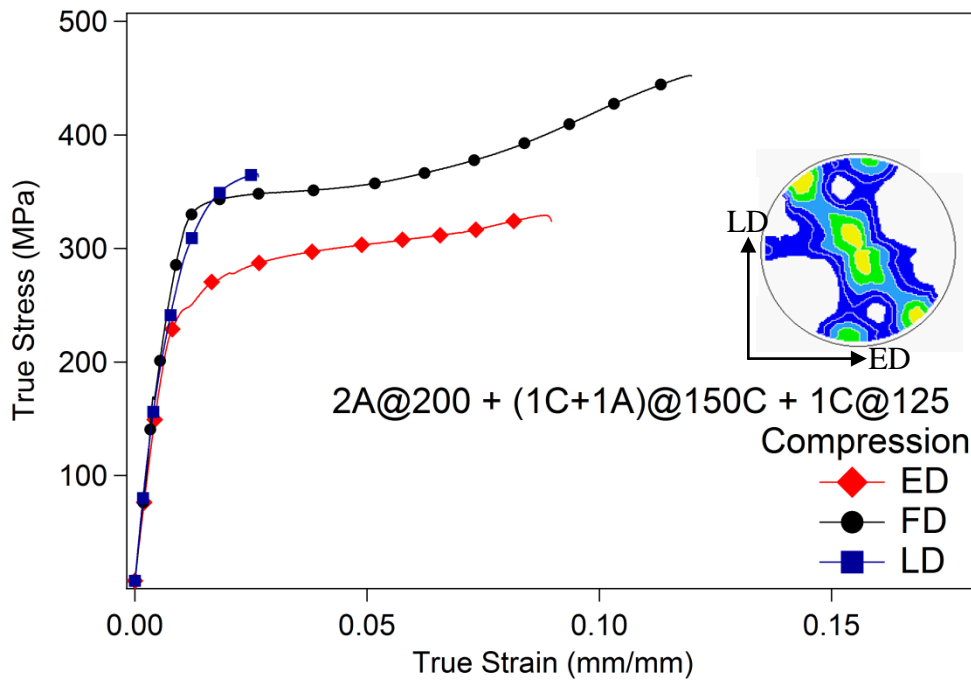


Figure 3.3.45. Compressive response of S23 along three orthogonal directions.

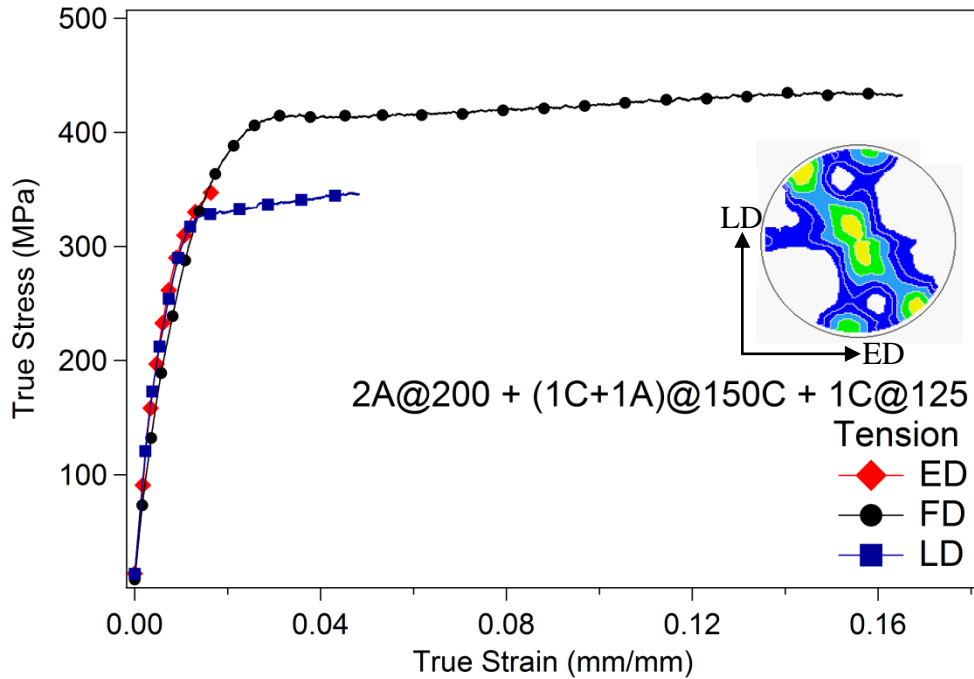


Figure 3.3.46. Tensile response of S23 along three orthogonal directions.

Lower ductility in tensile curves is probably due to strain localization and and/or possible micro-crack formation, since the last step of the processing yielded a billet with slight shear localization.

Table 3.3.10. Mechanical properties of S23.

		TENSION			COMPRESSION		
		σ_Y (MPa)	σ_{UTS} (MPa)	%strain (mm/mm)	σ_Y (MPa)	σ_{max} (MPa)	%strain (mm/mm)
S23	ED	346 ±2	347 ±3	1.7 ±0.1	268 ±4	329 ±7	8.8 ±0.2
	FD	395 ±4	431 ±4	16.6 ±0.5	329 ±7	452 ±5	11.9 ±0.6
	LD	323 ±6	345 ±6	4.8 ±0.1	346 ±4	366 ±5	2.6 ±0.1

The important observation from these curves is the effect of the thermo-mechanical hybrid processing on the activity of twins during compression along FD. The compressive yield strength of the hybrid samples is higher than that of the conventionally ECAE processed samples. The differences between these samples are the grain sizes and morphology and the amount of dislocations. The lower processing temperature at the final stages of the hybrid processing is expected to reduce dynamic recovery and recrystallization and, hence, increase the dislocation density inside the grains and at the grain boundaries. As discussed before, dynamic recovery and DRX have detrimental effects on yield strength of the material by reducing the dislocation density and introducing new unstrained grains. However, no effects of dynamic recovery and DRX were observed on the compressive yield strength along several directions. During this compression, plastic deformation is accommodated mainly by slip.

3.3.4 ECAE Failures

Deformation homogeneity is a vital necessity for ECAE to be considered “successful”. The homogeneity of the plastic strain field is fundamental condition to ensure homogeneity of microstructure and mechanical properties. However, depending on specific properties of the material, the tool geometry and conditions, process parameters like processing temperature, back pressure application and strain rate can change from the expected homogeneous simple shear to a complex inhomogeneous strain field; resulting in unsuccessful ECAE attempts. These factors are studied widely in many researches [2, 116, 156, 157].

However, it should be realized that failure during ECAE is generally due to combination of two or more of these factors and their effects should be considered accordingly.

There were several attempts in this study that resulted in specimen failure. For convenience, only S6, S7, S12 and S13 are presented here.

3.3.4.1 Shear Localization: S6, S7 and S12

A very common deduction from the ECAE literature is that slower deformation speeds are utilized to avoid any inhomogeneities that would originate from this effect [78, 122, 136, 157, 158]. Since the processing temperature is also proved to be one of the most important factors for shear localization especially in difficult to work alloys; one should remember that this effect shall not be considered alone, since higher speeds can also induce temperature rises during deformation [2, 116] and these rises may result in the changes in deformation mechanisms, as discussed in the previous sections. Higher temperatures may activate additional deformation mechanisms as in most of the HCP materials and contribute the progression and homogeneity of the processing [156, 157]. Lower temperatures, however, do not let this happen since the deformation is limited with some mechanisms and directionality becomes a very important factor.

Considering this, the processing speeds in the current study is maintained very low. Extrusion rates were kept at 0.075 mm/s for all the passes except for the passes at 100 °C and below, which was reduced to 0.038 mm/s to suppress shear localization [12, 135]. Kang et al. [136] reported uniform flow when AZ31 Mg alloy is pressed by 0.417 mm/sec at 200 °C; while segmented flow was observed at the same alloys when pressed at 0.17 mm/sec at 150 °C. It was observed 0.075 mm/s was sufficiently slow at this temperature for ZK60, but even going down to the extrusion rate 0.038 mm/sec was not enough to obtain uniform deformation; and resulted in segmented flow and total fracture at 100 °C and room temperature.

As mentioned in Section 3.4.3.2, there are a lot of studies carried out at elevated temperatures on Mg and Mg alloys, and even 200 °C is considered as “low temperature”. The only one that could go down to room temperature was reported by Biswas et.al.[120]. They succeeded processing pure Magnesium to structures with grain sizes around 250 µm using route A, at 8th pass, without any cracks. They carried out the first 4 passes at 250 °C; 5th at 200 °C; 6th at 150 °C; 7th at 100 °C and finally, 8th pass at room temperature.

ECAE deformation of S6 was attempted at room temperature at the very beginning of the work. The pressing speed was very low; 0.038 mm/s, and the maximum available back pressure for the alloy; its yield strength was applied. However, the result was a catastrophic failure; the billet was shattered into pieces around sizes of a few centimeters. The failure started right after loading, the billet could not even move in the exit channel after going through simple shear at the die channel intersection. The structural integrity was out of question.

S7 was aimed to be processed at 100 °C, but its end is very much the same with S6. The pressing speed and the applied back pressure were the same, but the catastrophic failure was inevitable. However, the billet managed to reach the exit channel this time, but fracture came in a few millimeters. The rest of the billet was shattered into pieces again and the part that went through the shear deformation at the channel cross section while maintaining its structural integrity, exhibited severe strain localization. When combined with Biswas’ findings, this gave the hope of lowering the temperatures and using the step-down effect while hybrid route design.

Strain localization and segmented flow, which was the characteristic of the failure that is observed at S7, was extensively experienced by S12 as well.

Despite maintaining structural integrity, the billet was exhibited extreme inhomogeneity in deformation; shear bands went all through the length of the billet. (Figure 3.3.47). The processing temperature of S12 was 200 °C, and the pressing speed was 0.075 mm/s. Considering that the processing temperature is quite high and the pressing speed was low, the reason for this behavior is attributed to the absence of back pressure.



Figure 3.3.47. S12 after ECAE (2A@200 °C).

During the deformation of S12, the load-displacement curve was monitored carefully, as in all other cases. The plot is given in Figure 3.3.48. The main characteristic of the shear localization is the sudden decrease of load during pressing. That drop in the load was observed while processing S12; and the “zero” back pressure was increased gradually to 10 MPa and 20 MPa. However, the inhomogeneous flow continued and the load fell down again. The sinus-like behavior evidenced the shear localization of the billet even before it is taken out from the die.

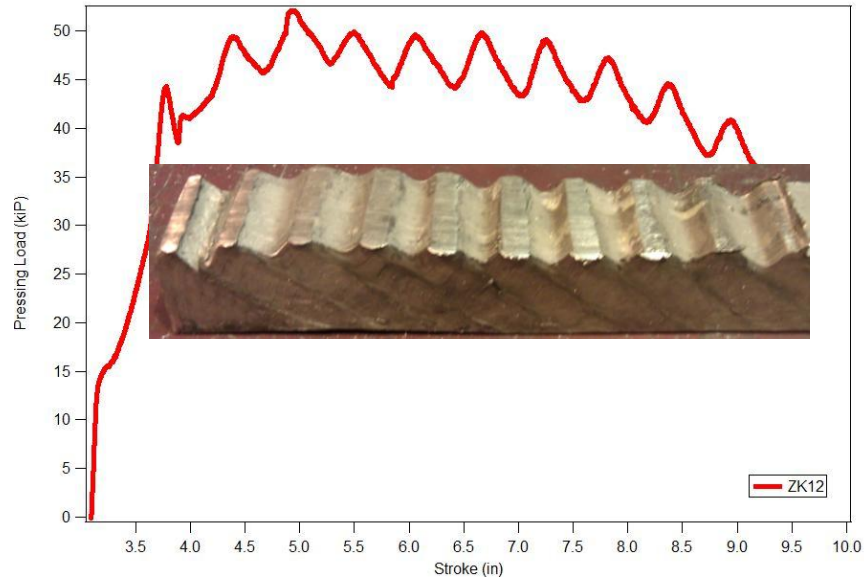


Figure 3.3.48. Load vs. displacement curve for S12.

The attempt to introduce and increase the back pressure for maintaining more homogeneous flow is employed in this study for almost all of the samples. The most important features of the back pressure application is prevention of the formation of the possible corner gaps [78, 122] and thus contributing the deformation homogeneity by making the process much more similar to ideal pure shear conditions. Without back pressure, the sample does not fill up the outer corner of the die. Additionally, the applied back pressure enhances hydrostatic force on the billet, resulting in the suppressing the tendency to shear localize and/or crack formation due to the more difficult processing temperatures involved [124]. However, if back pressure is used excessively, it can result in catastrophic failures of the specimens, as in S13.

3.3.4.3 Extreme Mushrooming: S13

As mentioned before back pressure is extensively applied for ECAE processing of ZK60, especially at lower temperatures. For most cases, back pressure is increased after each pass considering two main effects. The first one is the altered microstructure and texture after each pass. Since the material undergoes heavy deformation, it is expected to be harder to process. The crystallites can be aligned in hard-to-deform orientations and workability may decrease, accordingly. Decreased temperature and deformation mechanisms change and the deformation is limited to some mechanisms while directionality becomes a very important factor. Besides this, since the processing temperature decreases in some cases between the following passes, back pressure is applied for the ease of the processing without fracture or significant shear localization.

The back pressure is applied by the sliding bottom controlled by a hydraulic system. A schematic of this system was given in Figure 3.2.1.

The die design of the back pressure tool in MESAM Labs is quite similar to the one in schematics. One important difference is the diverging die walls at exit channel. The exit channel's upper wall has a diverging feature, which is designed for the ease of removal of the processed sample. According to the design, the extruded billet would relax in the diverged exit channel and would not stick in the die. However, when the back pressure system is added to the tool, the diverging die wall still remained in the die. Accordingly, when the back pressure is applied, the material tends to fill the diverged channel first. This does not create a problem as long as the back pressure applied is reasonable. The processed specimen, however, experiences an increase in cross section, other than elastic recovery. This phenomenon is called "mushrooming". Mushrooming is an insurance against strain localization. However, it should be limited to a

certain extent since excessive mushrooming would cause excessive material loss during the machining of the billet that is done in between each pass. The process is applied to make the billet machined to the correct dimension so that it can fit in the entrance channel.

If the applied back pressure is extremely high during ECAE, the enlarged billet is forced into the narrower channel, which, would result in a catastrophic failure, as in specimen S13. The billet is stuck in the die, and the only way to get it out is to disintegrate the die. The S13 sample is shown in Figure 3.3.49, after removal from the die. The enlargement of the specimen in the mid-section is obvious and this stopped the billet from moving forward.

Summing up these, one should be very careful while choosing the back pressure values that are to be applied. If there is no back pressure in the process, the billet still can undergo deformation without shear localization. However, this would result in the formation of the corner gap, and implies negative effects on the deformation homogeneity. If the billet is obtained from a hard-to-deform material, absence of back pressure may lead to shear localization, which would result in inhomogeneous microstructure and mechanical properties, accordingly. Such a billet that experiences this inhomogeneity can even undergo structural disintegration and fracture. On the other hand, applying excessive back pressure to avoid shear localization may have adverse effects that would cause mushrooming and thus excessive material loss. This mushrooming can lead to the complete opposite of the expected homogeneous deformation and even losing the original shape of the billet. Remembering that ECAE is proud to be the process that does not impose any shape changes, Considering all these, one should decide on the necessity and the level of back pressure carefully.



Figure 3.3.49. Failure of S13 due to extreme mushrooming (1A@ 200 °C).

3.3.5 Effect of Evolved Texture on Mechanical Response and Deformation Mechanisms

It is well known that Mg and Mg alloys exhibit plastic anisotropy and tension-compression asymmetry as a result of texture and the strong dependence of deformation mechanisms on crystal orientation. In this section, the effect of texture changes on room temperature plastic anisotropy in tension and compression are reported.

One distinct evidence of the effect of different texture evolutions is the tension/compression (T/C) asymmetry. This asymmetry takes place since the material exhibits different behaviors under tension and compression, depending on its texture. Twinning is mainly responsible from this asymmetry. When a material is deformed under tension, activation of twinning results in a complete different stress-strain behavior.

The different characteristics in T/C asymmetry and flow stress anisotropy in the processed Mg alloys can be explained by considering the textures that develop as a result of the starting texture through processing, and the straining path imposed when going from one pass to another and from ECAE shearing to uniaxial testing. The strong orientation dependence with respect to the direction of loading can be attributed to the ease of $\{10\bar{1}2\}$ twinning and the high ratio of CRSS between the slip modes in Mg alloys.

Assuming a CRSS criterion for slip and twinning, the CRSS values were characterized via single crystal model of pure Mg tested in various orientations [159]. The two easiest modes were tensile twinning (1 MPa) and basal slip (4 MPa) in comparison with for prismatic (12.5 MPa) and pyramidal $\langle c+a \rangle$ slip (63.2 MPa). The relative ease and directionality of twinning causes the stress-strain response to be highly sensitive to orientation of the c-axis with respect to tensile stress states generated under the applied loading. The relative ease of basal slip leads to flow responses highly dependent on the orientation of shearing with respect to the orientation of the basal slip planes.

As discussed in the previous sections, different routes of ECAE yield different textures. “A texture” results in increase strength values, whereas “C texture” contributes to ductility due to the alignment of the basal poles with a certain angle to the LD. Accordingly, conventional and hybrid routes are employed in this study.

At almost all of the cases in the current study, there are basal poles aligned through the LD on basal pole figures. When such textured materials are loaded under tension, through the LD, tensile twinning occurs. Tension along FD and ED would not activate tensile twinning; the most common twinning mechanism in Mg, but instead prismatic slip is activated with some extent of compressive

twinning to achieve homogeneous deformation. On the contrary, when compressed through LD, the material would not undergo tensile twinning since the crystals whose c-axis is almost concurrent with the LD tend to “fatten and shorten”, which is not favored at this alloy. Compressive loading through ED and FD of the same textured material, however, would tend to get the crystals “thinner and elongated”; and act like tensile twinning in this matter and responds accordingly. The plateau region, followed by rapid hardening, is observed for these cases at the stress-strain curves. However, a careful eye would realize that the twinning starts around the same stress value both under tension and compression, regardless of the loading direction (Figure 3.3.50). This also emphasizes the role of twinning in T/C asymmetry.

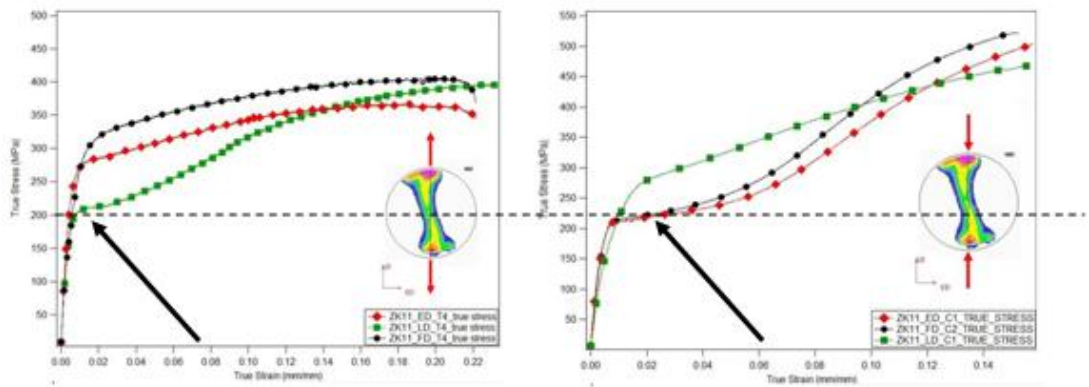


Figure 3.3. 50. Tensile behavior of S11 compared to its compressive behavior.

In literature, T/C asymmetry is represented by the stress differential (SD) effect, and can be quantified by the ratio:

$$\Delta = \frac{\sigma_y^c - \sigma_y^t}{0.5 (\sigma_y^c + \sigma_y^t)} \quad (3.3.1)$$

Where σ_y^t is the yield strength in forward tension and σ_y^c is the yield strength in forward compression The evolution of the stress differential (SD) [160] for all cases is listed in Table 3.3.11 and plotted as a function of ECAE routes in Figure 3.3.51.

Table 3.3.11. Stress differential values.

		TENSION			COMPRESSION			%SD
		σ_Y (MPa)	σ_{UTS} (MPa)	%strain (mm/mm)	σ_Y (MPa)	σ_{max} (MPa)	%strain (mm/mm)	
S4	ED	308	371	13.9	144	480	12	-72.8
	ND	144	370	19.8	166	351	14.9	14.2
S10	ED	345	396	10.5	239	484	16	-36.2
	FD	372	382	14.9	236	417	12.4	-44.9
	LD	247	364	15.7	312	393	11	23.1
S11	ED	281	361	21.2	197	513	15.5	-35.2
	FD	320	403	21.1	209	519	14.8	-42.1
	LD	202	400	23.9	255	468	15.5	23.5
S20	ED	238	285	3.4	212	333	12.1	-11.8
	FD	367	407	16.9	264	534	15.5	-32.7
	LD	211	267	8.5	259	299	4	20.4
S21	ED	326	377	15.1	223	367	12	-37.3
	FD	366	401	16.6	251	456	12	-37.2
	LD	253	367	14.2	333	421	8.9	27.2
S22	ED	156	290	14.7	212	485	16.3	30.9
	FD	294	380	18.7	210	316	14.7	-33.4
	LD	231	320	14.5	215	322	16.1	-7.3
S23	ED	346	347	1.7	268	329	8.8	-25.2
	FD	395	431	16.6	329	452	11.9	-18.2
	LD	323	345	4.8	346	366	2.6	6.8
S27	ED	354	410	11.1	249	450	13.2	-35.1
	FD	376	433	13.3	274	496	16.9	-31.5
	LD	296	409	16	350	406	8.5	16.9
S28	ED	342	407	4.5	293	493	14.8	-15.3
	FD	355	436	14.7	305	473	13.4	-15.3
	LD	304	411	11.6	339	405	8.1	10.9

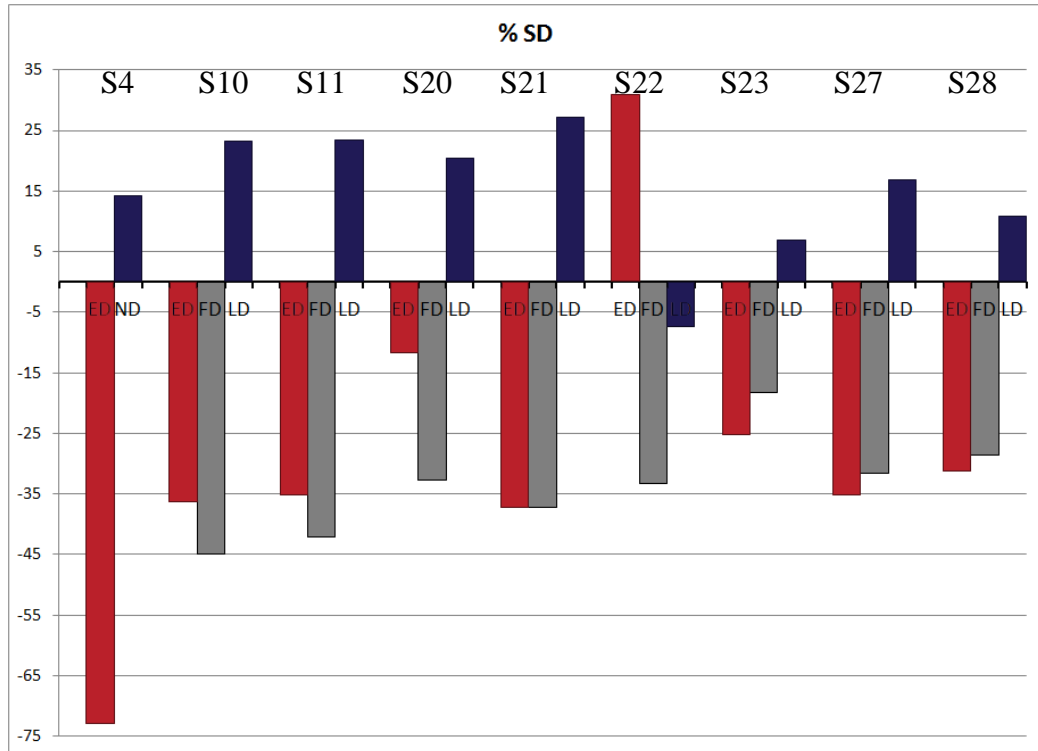


Figure 3.3.51. Stress differential values.

Al-Maharbi measured the SD values for two AZ31 alloys that have different initial textures, processed by ECAE [161]. One main conclusion he had is that the stronger the texture, the more the T/C asymmetry.

The increase in strength, as mentioned, is due to the non-basal slip. The (0002) texture component lies along LD. Under compression, when the material is tested along ED, tensile twinning will be observed, which causes the plateau region at the true stress-true strain curve, and inhibits further strengthening for some time. This period is also called yield stress elongation. When compressed along LD, compressive twinning is expected. However, compressive twinning is not a very common process in ZK60 alloys. Before that happens, prismatic slip takes place for deformation to continue, and significant hardening is observed at the curve, since CRSS for pyramidal slip is much higher than that of basal slip.

The material cannot undergo basal slip since the plane that basal slip takes place, (0002), is not aligned at the favorable easy glide direction. The compressive behavior along LD is different due to this texture.

The general difference of the SD of LD is due to the basal texture being aligned along or around that direction.

The first observation from the SD values for the cases curves is the similar behavior of all of the samples except S22 along both ED and FD in tension and compression. These samples yield at very close stress values when tested along ED and FD. The same thing can be said about the hardening behavior along LD of these samples; since their yield stress under tension is higher than compression.

In the samples, most grains have basal poles aligned with or just a few degrees away from LD, and almost perpendicular to ED and FD. Therefore, the deformation during tension along LD will be accommodated mostly by tensile twinning [162, 163]. The strain hardening behavior observed along LD is an evidence of the activation of twins, i.e. a plateau region with relatively steady stress [163] or low hardening coefficient followed by an upward curvature with a high hardening rate. This kind of hardening behavior is not seen when the alloy is pulled along ED or FD. Instead, the sample exhibits typical downward hardening curvature associated with slip dominated deformation. During this compression along LD, however, the material deforms mainly via basal and pyramidal $\langle c+a \rangle$ slip [162].

One other feature is that the hardening behavior is different in tension and compression along the same direction in the samples. This is, again due to the activated deformation mechanisms and thus, ECAE texture. This phenomenon

of opposite hardening behavior in tension and compression is seen in most of the samples; especially when tested along FD and ED.

Another clear observation from Figure 3.3.52 is that SD is always positive along the LD, i.e., the compressive yield strength is higher than the tensile one along this direction for the cases except S22. The basal poles of most of the grains in all those samples are aligned along the LD since the intensity of the basal peaks closer to the rim of the pole figure along LD is very large. Tension along LD will, then, activates tensile twinning. The strain hardening behavior observed along LD under tension is, also, evidence of the activation of twins, i.e. a plateau region with relatively steady stress [163] or low hardening coefficient followed by an upward curvature with a high hardening rate. This strain hardening behavior is observed in some samples; however the rates are not always the same. Hardening rate is high in cases like S11, whereas it is comparatively low for S10. This is because that the amount of grains that have c-axis parallel to the tension direction, LD, is higher in the latter. Therefore, it has higher Schmidt factor of basal slip than that of S11 sample. This will result in a high amount of twinning to compensate for the lack of basal slip and hence higher amount of T/C asymmetry as can be clearly seen in Figure 3.4.51. The influence of tensile twinning on T/C asymmetry is also the cause of high positive SD values along LD of the samples except S22. Along this direction, the samples have higher compressive yield strength, because of the activity of tensile twins, than its tensile yield stress.

The reason for the “discrimination” of S22 in this discussion was obviously the distinct texture that it has. On the contrary to every other case that is investigated in this study, S22 has a positive SD value along ED, whereas its SD value for LD is negative. SD along FD is not much different than that of others in terms of sign and magnitude, simply because every sample has a peak at their

basal pole figure that was there in the first place (at the as-received material), and is not intending to diminish since ECAE is a plane strain process. The basal pole figure of S22 might have lost its components along LD, but it preserves its components along FD. Besides, the basal poles in the structure can even be considered as lying at around 45 with LD and ED. Actually, tension along ED resulted in higher yield stress values in other cases since most of their basal poles were aligned at or around LD. ED, being the “weakest” direction under tension means the slip was much easier in that case, and the active deformation mechanism is most probably basal slip. This results in a positive SD value for this case. Remembering that SD is a signature of T/C asymmetry, and T/C asymmetry is directly related to the texture, observing a different behavior in this case is not surprising.

3.4. Conclusions

The increasing demand for better fuel economy, higher operating efficiency, and for the related reduction of exhausts has prompted the intensive search for the light-weight structural materials. Magnesium as the lightest metallic structural material with a density of 1.74 g/cm^3 , one-third dense than aluminium and four-fifth dense than iron, offers great potential for automobile and many industrial parts production. Apart of the lowest density, the high specific strength, good castability as well as the high possibility of recycling have made magnesium alloys as an attractive alternative for further technical applications. In fact the industrial usage of these alloys as a wrought material, however, has been shrunken by the fact that most magnesium alloys are hard to deform at relatively low temperature. The low formability is originally caused by the hexagonal crystallographic structure, which results in the limited number of active deformation modes. Moreover, due to these reasons the single crystals of magnesium alloys exhibit a pronounced anisotropy in many mechanical

properties. This anisotropy is inherited also into the polycrystalline state if the crystallites are not randomly oriented, namely, if the materials have a crystallographic texture. Since most magnesium alloys show a strong texture after typical thermo-mechanical processes such as rolling, extrusion or annealing, the orientation distribution of the crystallites (texture) is one of the most important parameters influencing on mechanical properties.

This part of the study was carried out to contribute to a basic understanding of the interrelationship among texture and microstructure evolution, activation of various deformation systems and mechanical properties of the magnesium alloy, ZK60. Since the texture reflects the deformation history and the deformation mechanism, the systematic study of the texture evolution under ECAE (Equal Channel Angular Extrusion) provides some meaningful knowledge on the mutual influences of an initial texture on the activity of theoretically possible deformation systems. It is known that the processing route has very important consequences on the evolved texture and the mechanical behavior.

Accordingly, this part of the study aimed to process ZK60 alloy by conventional and hybrid routes of to determine the best processing conditions for obtaining high strength and ductility in the alloy. To do this, the effect of the different ECAE routes, temperatures and the evolved texture with the active deformation modes are explored. The samples produced through these different parameters were mechanically tested, and the results were evaluated according to the evolved texture and microstructure. Besides, the mechanical anisotropy and tension compression (T/C) symmetry were determined. The investigation of microstructural and textural evolutions as well as the mechanical responses of ECAE processed materials; with the support of the data in literature, the governing deformation mechanisms were studied, and the process was attempted

to be optimized in order to achieve the desired mechanical properties for the specific applications; mainly a combination of good strength and ductility.

The following conclusions were made by the end of the Mg study:

- The starting texture is very important for texture evolution in following passes. The supplied material had extrusion texture in as-received form, where the basal fibers are located all through LD to FD. The FD (in-plane) components are shown to decrease the expected stress values. ZK60 will always have the disadvantage that comes with those basal fibers. Since ECAE is a plane strain process, it was not possible to get rid of the FD fibers and the remnant basal components through this direction causes decrease in the mechanical properties. The Mg alloys that are supplied in hot rolled sheets, for example, does not suffer this decrease that comes with the FD components and the relative increase in strength values in those alloys will be more pronounced. A secondary basal peak and its location in the basal pole figure can highly influence the slip activities during ECAE and hence the evolving texture.
- Back pressure in ECAE, when applied properly, can prevent the formation of a possible corner gap, which is a characteristic of ECAE. Without back pressure, the sample does not fill up the outer corner of the die. That characteristic is pretty unwanted since it deteriorates the deformation homogeneity. Shear localization is a very dangerous phenomenon in ECAE. It also caused failures and negative effects on ductility of the processed samples; some of them even resulting in failure. Being this advantageous, back pressure can also result in

catastrophic failure if used excessively. Accordingly, it should be applied with caution.

- The flow stress anisotropy and tension-compression asymmetry depend on the orientation of the basal planes with respect to the testing directions. The more random distribution of the basal planes the lower are the flow anisotropy and tension-compression asymmetry. Tensile twinning is the main factor for T/C asymmetry.
- Dynamic recrystallization (DRX) has a very significant role on microstructural and mechanical property evolution. Dynamic recovery and DRX have detrimental effects on yield strength of the material by reducing the dislocation density and introducing new unstrained grains. However, these effects are equalized and even outrivalled by the hardening due to Hall-Petch effect due to the decreases in grain sizes and twinning. Also, the activity of prismatic slip during ECAE significantly reduces the amount of DRX. Prismatic slip activity acts as a relaxation mechanism that reduces the likelihood of DRX.
- In literature, 200°C is called as “low temperature” for ECAE processing of Mg and its alloys, and there is not any study reporting the behavior under this temperature. In this study, it was clearly observed that the average grain size was decreased in the samples processed at lower temperature, where the basal component of the texture becomes sharper and the mechanical properties improve. However, it was also concluded that one should be careful about the possible further processing steps since those cases would not benefit from the DRX effect on microstructural evolution, and this may lead to shear localizations and early failures at the following steps. Besides, the deformation modes that

are activated at higher temperatures should be considered. Increased temperatures are known to decrease the CRSS of some of the possible deformation mechanisms of ZK60 and alter the deformation mode completely.

CHAPTER 4

CLOSING COMMENTS AND FUTURE WORK

The current work aimed to contribute the literature of FEM of ECAE process and Aluminum and Magnesium alloys and their processing technologies. The author believes that this general aim is fulfilled by studying the texture evolution and mechanical flow response and anisotropy in ZK60 Magnesium alloy and carrying out systematic FE simulations for ECAE. Most of the results presented here are firsts in their area; especially in Part 3, and the best mechanical properties achieved by using ECAE as a processing tool. The main reason is that the processing temperatures in literature are very high compared to the temperatures used in this study. Accordingly, the work gives fruitful results and discussions to the ones who would like to work in this area.

A possible future study about the ECAE processing of ZK60 alloy may include the effect of precipitates and heat treatments on microstructural evolution and mechanical properties. This would require detailed TEM studies for the evaluation of grain subdivision and cell formation mechanisms that take place during severe plastic deformation. The effect of precipitates on basal and non-basal slip and other deformation mechanisms shall be studied extensively. Heat treatments procedures before, after or in-between the passes may be practiced to evaluate this effect in every detail.

Another suggestion by the author would be the numerical modeling of the process for ZK60. VPSC model is commonly used for texture evolution of industrially common Mg alloys like AZ31. The same model can be run for ZK60, since the beginning texture is rather complicated compared to the hot rolled plates of AZ31 and its companions. Besides, it was observed that the VPSC studies mainly model the conventional routes and development of the model for the prediction of the texture evolution in hybrid routes would yield important and interesting results.

When modeling is considered, FEM of Mg alloys with all of its anisotropic properties defined in the model. A very sophisticated model that considers the grain size evolution, deformation mechanisms and the mechanical properties associated with those would be a very enlightening and useful for both Mg and FEM literature.

Besides all these, the author believes that the ECAE process cannot go anywhere further than a lab-scale application that is designed to study simple shear and fulfill scientific curiosity in the future; the process is still far away from industrialization in her point of view. The process is not continuous, thus production of “industrially long” parts is extremely hard, if not impossible. Such a situation requires extreme forces and huge dies to process long and wide billets. Another point that withholds ECAE from industrialization is that it almost always requires very low speeds. The process is highly energy consuming; accordingly, it is not preferred over conventional deformation methods. Considering all these, at this point, the author only hopes that she supplied helpful and enlightening information to the reader on ZK60 Mg alloy, and invokes the reader’s interest on the importance of the texture evolution in the Mg alloys and its effects on mechanical behavior, so that its usage in industrial processes would increase.

LIST OF REFERENCES

1. Segal, V.M., et al., *Plastic Working of Metals by Simple Shear* Russian Metallurgy-translation 1981. **1**: p. 99–105.
2. Valiev, R.Z. and T.G. Langdon, *Principals of equal-channel angular pressing as a processing tool for grain refinement* Progress in Materials Science, 2006. **51**: p. 7.
3. Alexandrov, I.V., *Multiscale studies and modeling of SPD materials*. Materials Science and Engineering a-Structural Materials Properties Microstructure and Processing, 2004. **387-89**: p. 772-776.
4. Alexandrov, I.V., et al., *Simulation of Equal-Channel Angular Extrusion Pressing*. Materials Science Forum, 2006. **503-504**: p. 201-208.
5. Yapici, G.G., et al., *Plastic flow anisotropy of pure zirconium after severe plastic deformation at room temperature*. Acta Materialia, 2009. **57**(16): p. 4855-4865.
6. Yapici, G.G., I. Karaman, and H.J. Maier, *Mechanical flow anisotropy in severely deformed pure titanium*. Materials Science and Engineering a-Structural Materials Properties Microstructure and Processing, 2006. **434**(1-2): p. 294-302.
7. Yapici, G.G., I. Karaman, and Z.P. Luo, *Mechanical twinning and texture evolution in severely deformed Ti-6Al-4V at high temperatures*. Acta Materialia, 2006. **54**(14): p. 3755-3771.
8. Tome, C.N., et al., *The relation between texture, twinning and mechanical properties in hexagonal aggregates*. Textures of Materials, Pts 1 and 2, 2002. **408-4**: p. 263-268.

9. Safi-Naqvi, S.H., W.B. Hutchinson, and M.R. Barnett, *Texture and mechanical anisotropy in three extruded magnesium alloys*. Materials Science and Technology, 2008. **24**(10): p. 1283-1292.
10. Ohyama, R., et al., *Texture dependence of elongation anisotropy in an AZ61 magnesium alloy sheet*. Journal of the Japan Institute of Metals, 2004. **68**(1): p. 27-33.
11. Hutchinson, B., et al., *Deformation modes and anisotropy in magnesium alloy AZ31*. International Journal of Materials Research, 2009. **100**(4): p. 556-563.
12. Foley, D.C., et al., *Grain refinement vs. crystallographic texture: Mechanical anisotropy in a magnesium alloy*. Scripta Materialia, 2011. **64**(2): p. 193-196.
13. Chino, Y., et al., *Mechanical anisotropy due to twinning in an extruded AZ31 Mg alloy*. Materials Science and Engineering a-Structural Materials Properties Microstructure and Processing, 2008. **485**(1-2): p. 311-317.
14. Yoo, M.H., *Interaction of Slip Dislocations with Twins in Hcp Metals*. Transactions of the Metallurgical Society of Aime, 1969. **245**(9): p. 2051-&.
15. Yapici, G.G. and I. Karaman, *Common trends in texture evolution of ultra-fine-grained hcp materials during equal channel angular extrusion*. Materials Science and Engineering a-Structural Materials Properties Microstructure and Processing, 2009. **503**(1-2): p. 78-81.
16. Vogel, S.C., et al., *Investigation of texture in ECAP materials using neutron diffraction*. Thermec'2003, Pts 1-5, 2003. **426-4**: p. 2661-2666.
17. Mukai, T., et al., *Effect of grain refinement on tensile ductility in ZK60 magnesium alloy under dynamic loading*. Materials Transactions, 2001. **42**(7): p. 1177-1181.

18. Koike, J., et al., *The activity of non-basal slip systems and dynamic recovery at room temperature in fine-grained AZ31B magnesium alloys*. *Acta Materialia*, 2003. **51**(7): p. 2055-2065.
19. Hartley, C.S., et al., *A Comparison of Deformation Textures and Mechanical Properties Predicted by Different Crystal Plasticity Codes*. *Materials Processing and Texture*, 2009. **200**: p. 701-712
20. Brown, D.W., et al., *Internal strain and texture evolution during deformation twinning in magnesium*. *Materials Science and Engineering a-Structural Materials Properties Microstructure and Processing*, 2005. **399**(1-2): p. 1-12.
21. Beausir, B., et al., *Analysis of microstructure and texture evolution in pure magnesium during symmetric and asymmetric rolling*. *Acta Materialia*, 2009. **57**(17): p. 5061-5077.
22. Alexandrov, I.V., R.G. Chembarisova, and V.D. Sitdikov, *Analysis of the Deformation Mechanisms in Bulk Ultrafine Grained Metallic Materials*. *Materials Science and Engineering a-Structural Materials Properties Microstructure and Processing*, 2007. **463**: p. 27-35.
23. Robson, J.D., N. Stanford, and M.R. Barnett, *Effect of precipitate shape on slip and twinning in magnesium alloys*. *Acta Materialia*, 2011. **59**(5): p. 1945-1956.
24. Al-Maharbi, M., et al., *Importance of Crystallographic Texture of AZ31B on Flow Stress Anisotropy and Tension-Compression Asymmetry*. *Magnesium Technology 2010*, 2010: p. 445-450
25. Barnett, M.R., *A Taylor model based description of the proof stress of magnesium AZ31 during hot working*. *Metallurgical and Materials Transactions a-Physical Metallurgy and Materials Science*, 2003. **34A**(9): p. 1799-1806.
26. Balogh, L., et al., *The contributions of grain size, dislocation density and twinning to the strength of a magnesium alloy processed by ECAP*.

- Materials Science and Engineering a-Structural Materials Properties Microstructure and Processing, 2010. **528**(1): p. 533-538.
27. Agnew, S.R., et al., *Texture evolution of five wrought magnesium alloys during route A equal channel angular extrusion: Experiments and simulations*. Acta Materialia, 2005. **53**(11): p. 3135-3146.
 28. Agnew, S.R., et al., *Crystallographic texture evolution of three wrought magnesium alloys during equal channel angular extrusion*. Materials Science and Engineering a-Structural Materials Properties Microstructure and Processing, 2005. **408**(1-2): p. 72-78.
 29. Barnett, M.R., *Twinning and the ductility of magnesium alloys Part I: "Tension" twins*. Materials Science and Engineering a-Structural Materials Properties Microstructure and Processing, 2007. **464**(1-2): p. 1-7.
 30. Barnett, M.R., *Twinning and the ductility of magnesium alloys Part 3. "Contraction" twins*. Materials Science and Engineering a-Structural Materials Properties Microstructure and Processing, 2007. **464**(1-2): p. 8-16.
 31. Orlov, D., et al., *Improvement of mechanical properties of magnesium alloy ZK60 by integrated extrusion and equal channel angular pressing*. Acta Materialia, 2011. **59**(1): p. 375-385.
 32. Shahzad, M. and L. Wagner, *The role of Zr-rich cores in strength differential effect in an extruded Mg-Zn-Zr alloy*. Journal of Alloys and Compounds, 2009. **486**(1-2): p. 103-108.
 33. Valiev, R.Z. and I.V. Alexandrov, *Nanostructured Materials From Severe Plastic Deformation*. NanoStructured Materials, 1999. **12**: p. 35-40.
 34. Segal, V.M., *Equal channel angular extrusion: from macromechanics to structure formation*. Materials Science and Engineering a-Structural

- Materials Properties Microstructure and Processing, 1999. **271**(1-2): p. 322-333.
35. Wei, W. and C. Guang, *An Upper Bound Analysis of Equal Channel Angular Pressing*. Journal of Metastable and Nanocrystalline Materials, 2005. **23**: p. 109-113.
 36. Wei, W., et al., *Origin of inhomogenous behavior during equal channel angular pressing*. Scripta Materialia, 2006. **54**(11): p. 1865-1869.
 37. Wu, P.D., Y. Huang, and D.J. Lloyd, *Studying grain fragmentation in ECAE by simulating simple shear*. Scripta Materialia, 2006. **54**(12): p. 2107-2112.
 38. Xu, S., et al., *Finite element analysis and optimization of equal channel angular pressing for producing ultra-fine grained materials*. Journal of Materials Processing Technology, 2006. **184**(1-3): p. 209-216.
 39. Furukawa, M., Z. Horita, and T.G. Langdon, *Factors influencing the shearing patterns in equal-channel angular pressing* Materials Science and Engineering A, 2002. **332**: p. 97-109.
 40. Beyerlein, I. and L. Tóth, *Texture evolution in equal-channel angular extrusion*. Progress in Materials Science, 2009. **54**: p. 427-510.
 41. Bowen, J.R., et al., *Analysis of the billet deformation behavior in equal channel angular extrusion*. Materials Science and Engineering a-Structural Materials Properties Microstructure and Processing, 2000. **287**: p. 87-99.
 42. Kim, H.S., M.H. Seo, and S.I. Hong, *On the die corner gap formation in equal channel angular pressing*. Materials Science and Engineering a-Structural Materials Properties Microstructure and Processing, 2000. **291**(1-2): p. 86-90.
 43. Iwahashi, Y., et al., *Principle of equal-channel angular pressing for the processing of ultra-fine grained materials*. Scripta Materialia, 1996. **35**(2): p. 143-146.

44. Enikeev, N.A., H.S. Kim, and I.V. Alexandrov, *Kinetic Dislocation Model of Microstructure Evolution During Severe Plastic Deformation*. Materials Science and Engineering a-Structural Materials Properties Microstructure and Processing, 2007. **460-461**: p. 619-623.
45. Pei, Q.X., et al., *A finite element study of the temperature rise during equal channel angular pressing*. Scripta Materialia, 2003. **49**(4): p. 303-308.
46. Prangnell, P.B., C. Harris, and S.M. Roberts, *Finite element modelling of equal channel angular extrusion*. Scripta Materialia, 1997. **37**(7): p. 983-989.
47. Kim, H.S., *Finite element analysis of equal channel angular pressing using a round corner die*. Materials Science and Engineering a-Structural Materials Properties Microstructure and Processing, 2001. **315**(1-2): p. 122-128.
48. Kim, H.S., *Finite element analysis of deformation behaviour of metals during equal channel multi-angular pressing*. Materials Science and Engineering a-Structural Materials Properties Microstructure and Processing, 2002. **328**(1-2): p. 317-323.
49. Kim, H.S., *On the effect of acute angles on deformation homogeneity in equal channel angular pressing*. Materials Science and Engineering a-Structural Materials Properties Microstructure and Processing, 2006. **430**(1-2): p. 346-349.
50. Kim, H.S., M.H. Seo, and S.I. Hong, *Plastic deformation of analysis of metals during equal channel angular pressing*. Journal of Materials Processing Technology, 2001. **113**: p. 622-626.
51. Alkorta, J. and J.G. Sevillano, *A comparison of FEM and upper-bound type analysis of equal-channel angular pressing (ECAP)*. Journal of Materials Processing Technology, 2003. **141**(3): p. 313-318.

52. Dumoulin, S., et al., *Finite element modeling of equal channel angular pressing: Effect of material properties, friction and die geometry*. Materials Science and Engineering a-Structural Materials Properties Microstructure and Processing, 2005. **410**: p. 248-251.
53. Nagasekhar, A.V. and Y. Tick-Hon, *Optimal tool angles for equal channel angular extrusion of strain hardening materials by finite element analysis*. Computational Materials Science, 2004. **30**(3-4): p. 489-495.
54. Nagasekhar, A.V., et al., *Effect of acute tool-angles on equal channel angular extrusion/pressing*. Materials Science and Engineering a-Structural Materials Properties Microstructure and Processing, 2005. **410**: p. 269-272.
55. Nagasekhar, A.V., Y. Tick-Hon, and H.P. Seow, *Deformation behavior and strain homogeneity in equal channel angular extrusion/pressing*. Journal of Materials Processing Technology, 2007.
56. Perez, C.J.L., P. Gonzalez, and Y. Garces, *Equal channel angular extrusion in a commercial Al-Mn alloy*. Journal of Materials Processing Technology, 2003. **143**: p. 506-511.
57. Srinivasan, R., *Computer simulation of the equichannel angular extrusion (ECAE) process*. Scripta Materialia, 2000. **44**: p. 91-96.
58. Stoica, G.M., et al., *An analysis of the shear zone for metals deformed by equal-channel angular processing*. Materials Science and Engineering a-Structural Materials Properties Microstructure and Processing, 2005. **410**: p. 239-242.
59. Suh, J.Y., et al., *Finite element analysis of material flow in equal channel angular pressing*. Scripta Materialia, 2001. **44**(4): p. 677-681.
60. Xu, S., et al., *Numerical studies on processing routes and deformation mechanism of multi-pass equal channel angular pressing processes*. Journal of Materials Processing Technology, 2006. **176**(1-3): p. 251-259.

61. Leo, P., et al., *Properties and deformation behaviour of severe plastic deformed aluminium alloys*. Journal of Materials Processing Technology, 2006. **182**(1-3): p. 207-214.
62. Oh, S.J. and S.B. Kang, *Analysis of the billet deformation during equal channel angular pressing*. Materials Science and Engineering a-Structural Materials Properties Microstructure and Processing, 2003. **343**(1-2): p. 107-115.
63. O'Brien, M.J., et al., *A finite element analysis of the superplastic forming of an aluminum alloy processed by ECAP*. Materials Science and Engineering a-Structural Materials Properties Microstructure and Processing, 2006. **456**: p. 236-242.
64. Suo, T., et al., *The simulation of deformation distribution during ECAP using 3D finite element method*. Materials Science and Engineering a-Structural Materials Properties Microstructure and Processing, 2006. **432**(1-2): p. 269-274.
65. Zhernakov, V.S., et al., *A numerical modelling and investigations of flow stress and grain refinement during equal-channel angular pressing*. Scripta Materialia, 2001. **44**(8-9): p. 1765-1769.
66. Baik, S.C., et al., *Dislocation density-based modeling of deformation behavior of aluminium under equal channel angular pressing*. Materials Science and Engineering a-Structural Materials Properties Microstructure and Processing, 2003. **351**(1-2): p. 86-97.
67. Kim, S.J., et al., *Finite Element Analysis of Equal Channel Angular Pressing Based on a Dislocation Density and Cell Size Evolution Model*. Journal of Metastable and Nanocrystalline Materials 2003. **15-16**: p. 231-234.
68. Karpuz, P., C. Şimşir, and C.H. Gür. *Simulation of equal channel angular pressing applied to produce structures with nano-size grains*. in

13. *Uluslararası Metalurji-Malzeme Kongresi*. 2006. TURKEY, Istanbul.
69. Li, S., et al., *Finite element analysis of the plastic deformation zone and working load in equal channel angular extrusion*. *Materials Science and Engineering a-Structural Materials Properties Microstructure and Processing*, 2004. **382**(1-2): p. 217-236.
70. Rosochowski, A. and L. Olejnik, *Numerical and physical modelling of plastic deformation in 2-turn equal channel angular extrusion*. *Journal of Materials Processing Technology*, 2002. **125**: p. 309-316.
71. Şimşir, C., P. Karpuz, and C.H. Gür, *Quantitative analysis of the influence of strain hardening on equal channel angular pressing process*. *Computational Materials Science*, 2010. **48**(3): p. 633-639.
72. Wu, Y. and I. Baker, *An experimental study of equal channel angular extrusion*. *Scripta Materialia*, 1997. **37**(4): p. 437-442.
73. Karpuz, P., C. Simsir, and C.H. Gür, *Investigating the effects of hardening of aluminium alloys on equal-channel angular pressing—A finite-element study*. *Materials Science and Engineering: A*, 2009. **503**(1–2): p. 148-151.
74. Yoon, S.C., et al., *Die design for homogeneous plastic deformation during equal channel angular pressing*. *Journal of Materials Processing Technology*, 2007. **187**: p. 46-50.
75. Baik, S.C., et al., *Calculation of Deformation Behavior and Texture Evolution During Equal Channel Angular Pressing of IF Steel Using Dislocation Based Modeling of Strain Hardening*. *Materials Science Forum*, 2002. **408-421**: p. 697-702.
76. Alexandrov, I.V. and R.Z. Valiev, *Developing of SPD processing and enhanced properties in bulk nanostructured metals*. *Scripta Materialia*, 2001. **44**(8-9): p. 1605-1608.

77. Ding, S.X., et al., *Improvement of strength of magnesium alloy processed by equal channel angular extrusion*. Scripta Materialia, 2008. **59**(9): p. 1006-1009.
78. Boulahia, R., et al., *Deformation behaviour and mechanical properties of polypropylene processed by equal channel angular extrusion: Effects of back-pressure and extrusion velocity*. Polymer, 2009. **50**(23): p. 5508-5517.
79. Barber, R.E., et al., *Product yield for ECAE processing*. Scripta Materialia, 2004. **51**(5): p. 373-377.
80. Cottam, R., et al., *Dynamic recrystallization of Mg and Mg–Y alloys: Crystallographic texture development*. Materials Science and Engineering: A, 2008. **485**(1-2): p. 375-382.
81. Graff, S., W. Brocks, and D. Steglich, *Yielding of magnesium: From single crystal to polycrystalline aggregates*. International Journal of Plasticity, 2007. **23**(12): p. 1957-1978.
82. Yoo, M.H., *Slip, Twinning, and Fracture in Hexagonal Close-Packed Metals*. Metallurgical Transactions a-Physical Metallurgy and Materials Science, 1981. **12**(3): p. 409-418.
83. Kuhlmann-Wilsdorf, D. and N. Hansen, *Geometrically necessary, incidental and subgrain boundaries*. Scripta Metallurgica et Materialia, 1991. **25**(7): p. 1557-1562.
84. Philippe, M.J., *Texture Formation in Hexagonal Materials*. Materials Science Forum 1994. **157-162**: p. 1337-1350.
85. K.B., M., *Direct and Indirect Extrusion of AZ31*, in *Magnesium Technology, 2002, TMS Annual Meeting*, H.I. Kaplan, Editor 2002, The Materials Society: Seattle, WA. p. 187-192.
86. Barrett, C. and T.B. Massalskim, *Structure of metals* 1980: Pergamon Press.

87. Dillamore, I.L. and W.T. Roberts, *Preferred orientation in wrought and annealed metals*. Metall. Review, 1965. **10**.
88. Kelley, E.W. and W.F. Hosford Jr., *The deformation characteristics of textured magnesium*. Trans. TMS-AIME, 1968. **242**: p. 654–661.
89. Kaiser, F., *Anisotropic properties of magnesium sheet AZ31*. Materials Science Forum, 2003. **315**: p. 419-422.
90. Barnett, M.R., M.D. Nave, and C.J. Beatles, *Deformation microstructures and textures of some cold rolled magnesium alloys*. Materials Science and Engineering a-Structural Materials Properties Microstructure and Processing, 2004. **386**.
91. Pérez-Prado, M.T., J.A. del Valle, and O.A. Ruano, *Effect of sheet thickness on the microstructural evolution of an Mg AZ61 alloy during large strain hot rolling*. Scripta Materialia, 2004. **50**(5): p. 667-671.
92. Agnew, S.R. and Ö. Duygulu, *Plastic anisotropy and the role of non-basal slip in magnesium alloy AZ31B*. International Journal of Plasticity, 2005. **21**(6): p. 1161-1193.
93. Pérez-Prado, M.T., et al., *Microstructural evolution during large strain hot rolling of an AM60 Mg alloy*. Scripta Materialia, 2004. **50**(5): p. 661-665.
94. Agnew, S.R., M.H. Yoo, and C.N. Tome, *Application of texture simulation to understanding mechanical behavior of Mg and solid solution alloys containing Li or Y*. Acta Materialia, 2001. **49**(20): p. 4277-4289.
95. Beyerlein, I.J. and L.S. Tóth, *Texture evolution in equal-channel angular extrusion*. Progress in Materials Science, 2009. **54**(4): p. 427-510.
96. Beyerlein, I.J., et al., *Statistical analyses of deformation twinning in magnesium (vol 90, pg 2161, 2010)*. Philosophical Magazine, 2010. **90**(30): p. 4073-4074.

97. Beyerlein, I.J., et al., *Statistical analyses of deformation twinning in magnesium*. Philosophical Magazine, 2010. **90**(16): p. 2161-2190.
98. Beyerlein, I.J., R.A. Lebensohn, and C.N. Tome, *Polycrystal constitutive modeling of ECAP: Texture and microstructural evolution*. Ultrafine Grained Materials 3, 2002: p. 585-594
99. Beyerlein, I.J., R.A. Lebensohn, and C.N. Tome, *Modeling texture and microstructural evolution in the equal channel angular extrusion process*. Materials Science and Engineering a-Structural Materials Properties Microstructure and Processing, 2003. **345**(1-2): p. 122-138.
100. Beyerlein, I.J., et al., *Heterogeneity in texture development in single pass equal channel angular extrusion*. Ultrafine Grained Materials 3i, 2004: p. 185-192
101. Beyerlein, I.J., et al., *Non-uniform microstructure and texture evolution during equal channel angular extrusion*. Philosophical Magazine, 2005. **85**(13): p. 1359-1394.
102. Beyerlein, I.J. and C.N. Tome, *A dislocation-based constitutive law for pure Zr including temperature effects*. International Journal of Plasticity, 2008. **24**(5): p. 867-895.
103. Beyerlein, I.J. and C.N. Tome, *A probabilistic twin nucleation model for HCP polycrystalline metals*. Proceedings of the Royal Society a-Mathematical Physical and Engineering Sciences, 2010. **466**(2121): p. 2517-2544.
104. Beyerlein, I.J., et al., *Role of twinning on texture evolution of silver during equal channel angular extrusion*. Philosophical Magazine, 2007. **87**(6): p. 885-906.
105. Beyerlein, I.J. and C.N. Tome, *Analytical modeling of material flow in equal channel angular extrusion (ECAE)*. Materials Science and Engineering a-Structural Materials Properties Microstructure and Processing, 2004. **380**(1-2): p. 171-190.

106. Beyerlein, I.J. and C.N. Tome, *Modeling compression reloads in copper prestrained by equal channel angular extrusion (ECAE)*. *Materialwissenschaft Und Werkstofftechnik*, 2005. **36**(10): p. 541-545.
107. Beyerlein, I.J. and C.N. Tome, *Modeling directional anisotropy in grains subjected to large strains and strain path changes*. *Ultrafine Grained Materials IV*, 2006: p. 63-71
108. Beyerlein, I.J. and C.N. Tome, *Modeling compression and tension reloads in copper prestrained by rolling*. *Thermec 2006, Pts 1-5*, 2007. **539-543**: p. 3383-3388
109. Beyerlein, I.J. and C.N. Tome, *Modeling transients in the mechanical response of copper due to strain path changes*. *International Journal of Plasticity*, 2007. **23**(4): p. 640-664.
110. Bhowmik, A., et al., *Evolution of Grain-Boundary Microstructure and Texture in Interstitial-Free Steel Processed by Equal-Channel Angular Extrusion*. *Metallurgical and Materials Transactions a-Physical Metallurgy and Materials Science*, 2009. **40A**(11): p. 2729-2742.
111. Tome, C.N., et al., *Simulations of Texture Development in Calcite - Comparison of Polycrystal Plasticity Theories*. *Journal of Geophysical Research-Solid Earth and Planets*, 1991. **96**(B7): p. 11865-11875.
112. Bunge, H.J., *Texture analysis in material science. Mathematical Methods* 1993, Gottingen.
113. Karpuz, P., C. Simsir, and C.H. Gür, *Investigating the effects of hardening of aluminium alloys on equal-channel angular pressing—A finite-element study*. *Materials Science and Engineering: A*, 2009. **503**(1-2): p. 148-151.
114. Laboratories, L.A.N., *Preferred Orientation Package – Los Alamos: User's Manual*, 1995: Los Alamos.
115. Lapovok, R.Y.E., *The role of back-pressure in equal channel angular extrusion*. *Journal of Materials Science*, 2005. **40**(2): p. 341-346.

116. Horita, Z., et al., *Superplastic forming at high strain rates after severe plastic deformation*. Acta Materialia, 2000. **48**(14): p. 3633-3640.
117. Zisman, A.A., et al., *Equal channel angular drawing of aluminium sheet*. Materials Science and Engineering a-Structural Materials Properties Microstructure and Processing, 2006. **427**(1-2): p. 123-129.
118. Furukawa, M., et al., *The use of severe plastic deformation for microstructural control*. Materials Science and Engineering a-Structural Materials Properties Microstructure and Processing, 2002. **324**(1-2): p. 82-89.
119. Zhao, G., et al., *Grain refinement mechanism analysis and experimental investigation of equal channel angular pressing for producing pure aluminum ultra-fine grained materials*. Materials Science and Engineering a-Structural Materials Properties Microstructure and Processing, 2006. **437**: p. 281-292.
120. Biswas, S., S.S. Dhinwal, and S. Suwas, *Room-temperature equal channel angular extrusion of pure magnesium*. Acta Materialia, 2010. **58**(9): p. 3247-3261.
121. Figueiredo, R.B. and T.G. Langdon, *Grain refinement and mechanical behavior of a magnesium alloy processed by ECAP*. Journal of Materials Science, 2010. **45**(17): p. 4827-4836.
122. Figueiredo, R.B., P.R. Cetlin, and T.G. Langdon, *The processing of difficult-to-work alloys by ECAP with an emphasis on magnesium alloys*. Acta Materialia, 2007. **55**(14): p. 4769-4779.
123. Figueiredo, R.B. and T.G. Langdon, *Principles of grain refinement in magnesium alloys processed by equal-channel angular pressing*. Journal of Materials Science, 2009. **44**(17): p. 4758-4762.
124. Lapovok, R., et al., *Strain localisation patterns under equal-channel angular pressing*. Journal of the Mechanics and Physics of Solids, 2009. **57**(1): p. 122-136.

125. Sevillano, J.G., C. Garcia-Rosales, and J.F. Fuster, *Texture and Large-Strain Deformation Microstructure*. Philosophical Transactions of the Royal Society of London Series A, 1999. **357**.
126. Kuhlmann-Wilsdorf, D., et al., *Deformation bands, the LEDS theory, and their importance in texture development: Part I. Previous evidence and new observations*. Metallurgical and Materials Transactions A, 1999. **30**(9): p. 2491-2501.
127. D, K.-W., *Theory of plastic deformation: - properties of low energy dislocation structures*. Materials Science and Engineering: A, 1989. **113**(0): p. 1-41.
128. Doris, K.-W., *Fundamentals of cell and subgrain structures in historical perspective*. Scripta Metallurgica et Materialia, 1992. **27**(8): p. 951-956.
129. Kuhlmann-Wilsdorf, D., *Deformation bands, the LEDS theory, and their importance in texture development: Part 3. Theoretical conclusions*. Metallurgical and Materials Transactions A, 1999. **30**(9): p. 2391-2401.
130. Galiyev, A., R. Kaibyshev, and G. Gottstein, *Correlation of plastic deformation and dynamic recrystallization in magnesium alloy Zk60*. Acta Materialia, 2001. **49**(7): p. 1199-1207.
131. Galiyev, A.M., R.O. Kaibyshev, and G. Gottstein, *Mechanisms of dynamic recrystallization in a Mg-Zn-Zr alloy*. Recrystallization and Grain Growth, Vols 1 and 2, 2001: p. 893-898
132. Galiyev, A.M., R.O. Kaibyshev, and G. Gottstein, *Grain refinement of ZK60 magnesium alloy during low temperature deformation*. Magnesium Technology 2002, 2002: p. 181-185
133. Al-Samman, T. and G. Gottstein, *Dynamic recrystallization during high temperature deformation of magnesium*. Materials Science and Engineering a-Structural Materials Properties Microstructure and Processing, 2008. **490**(1-2): p. 411-420.

134. Modarres Razavi, S., *Effect of Texture on formability and mechanical anisotropy of a severe plastically deformed magnesium alloy*, in *Mechanical Engineering* 2011, Texas A&M University: College Station.
135. Barnett, M.R., *Twinning and ductile failure of Mg-3Al-1Zn*. *Magnesium Technology* 2007, 2007: p. 29-32
136. Kang, F., J.T. Wang, and Y. Peng, *Deformation and fracture during equal channel angular pressing of AZ31 magnesium alloy*. *Materials Science and Engineering: A*, 2008. **487**(1-2): p. 68-73.
137. He, Y., et al., *Microstructure and mechanical properties of ultrafine grain ZK60 alloy processed by equal channel angular pressing*. *Journal of Materials Science*, 2010. **45**: p. 1655-1662.
138. Barnett, M.R., et al., *Influence of grain size on the compressive deformation of wrought Mg-3Al-1Zn*. *Acta Materialia*, 2004. **52**(17): p. 5093-5103.
139. Agnew, S.R., et al., *Assessment of equal channel angular extrusion processing of magnesium alloys*. *Magnesium Technology* 2001, 2001: p. 243-247
140. Stoica, G.M., et al., *Microstructure, and ductility of Mg alloy, ZK60, after equal channel angular processing*. *Ultrafine Grained Materials* 3i, 2004: p. 427-432
141. Karaman, I., et al., *Deformation twinning in difficult-to-work alloys during severe plastic deformation*. *Materials Science and Engineering a-Structural Materials Properties Microstructure and Processing*, 2005. **410**: p. 243-247.
142. Proust, G., et al., *Modeling the effect of twinning and detwinning during strain-path changes of magnesium alloy AZ31*. *International Journal of Plasticity*, 2009. **25**(5): p. 861-880.

143. Capolungo, L., I.J. Beyerlein, and C.N. Tome, *Slip-assisted twin growth in hexagonal close-packed metals*. Scripta Materialia, 2009. **60**(1): p. 32-35.
144. Al-Samman, T. and G. Gottstein, *Dynamic recrystallization during high temperature deformation of magnesium*. Materials Science and Engineering A, 2008. **490**: p. 411-420.
145. Obara, T., H. Yoshinga, and S. Morozumi, $\{112\bar{2}\} \langle 1123 \rangle$ Slip system in magnesium. Acta Metallurgica, 1973. **21**(7): p. 845-853.
146. Sheerly, W.F. and R.R. Nash, Transactions of the Metallurgical Society of Aime, 1960. **218**: p. 416.
147. Gottstein, G. and T. Al Samman, *Texture Development in pure Mg and Mg alloy AZ31*. Materials Science Forum, 2005. **495-497**: p. 623-632.
148. Al-Samman, T. and G. Gottstein, *Room temperature formability of a magnesium AZ31 alloy: Examining the role of texture on the deformation mechanisms*. Materials Science and Engineering a-Structural Materials Properties Microstructure and Processing, 2008. **488**(1-2): p. 406-414.
149. Tan, J.C. and M.J. Tan, *Dynamic continuous recrystallization characteristics in two stage deformation of Mg-3Al-1Zn alloy sheet*. Materials Science and Engineering: A, 2003. **339**(1-2): p. 124-132.
150. Beausir, B., et al., *Analysis of texture evolution in magnesium during equal channel angular extrusion*. Acta Materialia, 2008. **56**(2): p. 200-214.
151. Al-Samman, T. and G. Gottstein, *Deformation conditions and stability of the basal texture in magnesium*. Thermec 2006, Pts 1-5, 2007. **539-543**: p. 3401-3406
152. Horita, Z., et al., *A two-step processing route for achieving a superplastic forming capability in dilute magnesium alloys*. Scripta Materialia, 2002. **47**(4): p. 255-260.

153. Jin, L., et al., *Mechanical properties and microstructure of AZ31 Mg alloy processed by two-step equal channel angular extrusion*. Materials Letters, 2005. **59**(18): p. 2267-2270.
154. Barnett, M.R., et al., *Role of grain boundary sliding in the anisotropy of magnesium alloys*. Scripta Materialia, 2009. **61**(3): p. 277-280.
155. Koike, J., et al., *Grain-boundary sliding in AZ31 magnesium alloys at room temperature to 523 K*. Materials Transactions, 2003. **44**(4): p. 445-451.
156. Semiatin, S.L. and D.P. DeLo, *Equal channel angular extrusion of difficult-to-work alloys*. Materials & Design, 2000. **21**(4): p. 311-322.
157. Semiatin, S.L., D.P. DeLo, and E.B. Shell, *The effect of material properties and tooling design on deformation and fracture during equal channel angular extrusion*. Acta Materialia, 2000. **48**: p. 1841-1851.
158. Semiatin, S.L. and D.P. DeLo, *Equal channel angular extrusion of difficult-to-work alloys*. Materials & Design, 2000. **21**(4): p. 311-322.
159. Capolungo, L., I.J. Beyerlein, and C.N. Tomé, *Slip-assisted twin growth in hexagonal close-packed metals*. Scripta Materialia, 2009. **60**: p. 32-35.
160. Sun, P., P. Kao, and C. Chang, *Effect of deformation route on microstructural development in aluminum processed by equal channel angular extrusion* Metallurgical and Materials Transactions A-Physical Metallurgy and Materials Science, 2004. **35A**: p. 1359-1368.
161. Al-Maharbi, M., *Mechanical flow response and anisotropy of ultra-fine grained magnesium and zinc alloys*", in *MEEN2009*, Texas A&M University: College Station.
162. Proust, G., et al., *Modeling the effect of twinning and detwinning during strain-path changes of magnesium alloy AZ31*. International Journal of Plasticity, 2008. **In press, corrected proof**.

163. Barnett, M.R., *Twinning and the ductility of magnesium alloys Part I: "Tension" twins*. *Materials Science and Engineering A*, 2007. **464**: p. 1-7.

VITA

Pinar Karpuz was born in Ankara, Turkey. After receiving a B.S. degree in Metallurgical and Materials Engineering from Middle East Technical University in 2002, she completed her M.S. studies and got her degree from the same department in 2005 and started the Ph.D. program. During her graduate studies, she continuously held a research/teaching assistantship position, while publishing three peer-reviewed journal articles. She also had the opportunity to present her research in three international conference symposia. Upon graduation, she will continue her post-doctorate studies in Texas A&M University in Texas, USA.

Her permanent address is:

Department of Mechanical Engineering

c/o Dr. Ibrahim Karaman

Texas A&M University

College Station, TX 77843-3123

Email: pinar.karpuz@gmail.com